

A Parametric Galactic Model toward the Galactic Bulge Based on Gaia and Microlensing Data

NAOKI KOSHIMOTO,^{1,2} JUNICHI BABA,³ AND DAVID P. BENNETT^{1,2}¹*Laboratory for Exoplanets and Stellar Astrophysics, NASA/Goddard Space Flight Center, Greenbelt, MD 20771, USA*²*Department of Astronomy, University of Maryland, College Park, MD 20742, USA*³*National Astronomical Observatory of Japan, Mitaka, Tokyo 181-8588, Japan*

ABSTRACT

We developed a parametric Galactic model toward the Galactic bulge by fitting to spatial distributions of the Gaia DR2 disk velocity, VVV proper motion, BRAVA radial velocity, OGLE-III red clump star count, and OGLE-IV star count and microlens rate, optimized for use in microlensing studies. We include the asymmetric drift of Galactic disk stars and the dependence of velocity dispersion on Galactic location in the kinematic model, which has been ignored in most previous models used for microlensing studies. We show that our model predicts a microlensing parameter distribution significantly different from those typically used in previous studies. We estimate various fundamental model parameters for our Galaxy through our modeling, including the initial mass function (IMF) in the inner Galaxy. Combined constraints from star counts and the microlensing event timescale distribution from the OGLE-IV survey, in addition to a prior on the bulge stellar mass, enable us to successfully measure IMF slopes using a broken power-law form over a broad mass range, $\alpha_{\text{bd}} = 0.22^{+0.20}_{-0.55}$ for $M < 0.08 M_{\odot}$, $\alpha_{\text{ms}} = 1.16^{+0.08}_{-0.15}$ for $0.08 M_{\odot} \leq M < M_{\text{br}}$, and $\alpha_{\text{hm}} = 2.32^{+0.14}_{-0.10}$ for $M \geq M_{\text{br}}$, as well as a break mass at $M_{\text{br}} = 0.90^{+0.05}_{-0.14} M_{\odot}$. This is significantly different from the Kroupa IMF for local stars, but similar to the Zoccali IMF measured from a bulge luminosity function. We also estimate the dark matter mass fraction in the bulge region of $28 \pm 7\%$ which could be larger than a previous estimate. Because our model is purely parametric, it can be universally applied using the parameters provided in this paper.^{a)}

Keywords: Milky Way Galaxy (1054), Galactic bulge (2041), Initial mass function (796), Gravitational microlensing (672)

1. INTRODUCTION

Gravitational microlensing is a unique tool that can study the population of planetary to black hole mass objects in our Galaxy (Gaudi et al. 2019). It has been applied to study the population of exoplanets since the proposal by Mao & Paczynski (1991), along with more than 100 exoplanets, has been discovered as of 2020¹. Suzuki et al. (2016) used a statistical sample of 30 microlensing planets to reveal a likely peak at $q \sim 10^{-4}$ in the mass-ratio function of planets beyond the H₂O snow line for the first time, challenging the core accretion theory (Suzuki et al. 2018). Microlensing also enables us

^{a)} A tool for microlensing simulation using our Galactic model has been published (Koshimoto & Ranc 2021), and can be downloaded at <https://github.com/nkoshimoto/genulens>.

¹ NASA Exoplanet Archive (Akeson et al. 2013)

to study the population of free-floating planets (Sumi et al. 2011; Mróz et al. 2017). Further, some candidates of isolated black holes have also been discovered (Bennett et al. 2002; Poindexter et al. 2005; Wyrzykowski et al. 2016; Wyrzykowski & Mandel 2020).

Difficulty in measuring the lens mass and distance makes microlensing studies complex. Although four physical quantities, namely the lens mass M_L , distance from lens D_L , distance from source D_S , and lens-source relative proper motion μ_{rel} , are involved in each microlensing event, the Einstein radius crossing time

$$t_E = \frac{\theta_E}{\mu_{\text{rel}}}, \quad (1)$$

is the only quantity that is measurable for all events, where θ_E is the angular Einstein radius given by

$$\theta_E = \sqrt{\kappa M_L \pi_{\text{rel}}} \quad (2)$$

with $\kappa = 8.144 \text{ mas } M_\odot^{-1}$ and $\pi_{\text{rel}} = 1 \text{ AU}(D_L^{-1} - D_S^{-1})$. For microlensing events toward the Galactic bulge, the source star is assumed to be a bulge star, i.e., $D_S \sim 8 \text{ kpc}$, but the three remaining quantities still degenerate in a t_E value.

There are three observable quantities each of which provides a mass-distance relation: the angular Einstein radius, θ_E , microlens parallax, π_E , and lens star flux. The degeneracy in t_E could be disentangled when any two of the three are observed. The angular Einstein radius is given by Eq. (2) while the microlens parallax is given by

$$\pi_E = \frac{\pi_{\text{rel}}}{\theta_E}, \quad (3)$$

and these two quantities can be measured through higher order effects in the light curve, finite source effect (Yoo et al. 2004) and annual parallax effect caused by the Earth's orbital motion (Alcock et al. 1995; An et al. 2002), respectively. However, these effects are rarely measured, particularly for single-lens events that account for $\sim 90\%$ of all microlensing events. We can measure the lens flux with high-angular resolution follow-up imaging using adaptive optics (AO) or the *Hubble Space Telescope* (*HST*) (Batista et al. 2015; Bennett et al. 2015; Bhattacharya et al. 2018). However, such measurements typically require us to wait for $\gtrsim 5$ years until the lens-source separation can be measured, depending on the relative proper motion and contrast between lens and source stars. These limitations associated with the lens mass and distance measurements have resulted in many microlensing studies suffering from a chronic lack of information.

From this perspective, a Galactic model, which refers to a combination of a stellar mass function and stellar density and velocity distributions in our Galaxy, has played a crucial role in providing prior probability distributions for microlensing events toward the Galactic bulge. For example, a large number of studies on individual event analysis use a Galactic model to calculate a posterior distribution of the lens mass and distance (e.g., Alcock et al. 1995; Beaulieu et al. 2006; Koshimoto et al. 2014; Bennett et al. 2014). Further, it has also been used for statistical studies to estimate fundamental parameters in our Galaxy, such as the slope of initial mass function (IMF) (Sumi et al. 2011; Mróz et al. 2017; Wegg et al. 2017) or dark matter fraction in the bulge region (Wegg et al. 2016). Galactic models are occasionally used to diagnose whether measurements of microlensing parameters are contaminated by systematic errors (Penny et al. 2016; Koshimoto & Bennett 2020).

However, there are concerns regarding the use of Galactic models because the results depend on the choice of models, with most Galactic models used in microlensing studies employing several simplified features (Yang et al. 2020). This is a concern specifically for statistical studies in which small effects for many individual events can be combined. For example, Koshimoto & Bennett (2020) compared three different Galactic models by Sumi et al. (2011), Bennett et al. (2014), and Zhu et al. (2017) with 50 microlens parallax measurements by the 2015 *Spitzer* microlensing campaign (Zhu et al. 2017) and concluded that the parallax measurements are significantly contaminated due to systematic errors based on diagnoses using the Anderson-Darling (AD) tests. Here, all of the three models use simplified models for disk kinematics with flat rotation curves, constant velocity dispersions, and no asymmetric drift, which contradict the observed velocity distributions (Gaia Collaboration et al. 2018). Although the conclusions seem robust because they are based on the discovered correlations between p -values from the AD tests and some characteristics of events, which are likely related to vulnerability to systematic errors (e.g., source brightness or peak coverage), the absolute p -values might be misestimated due to the simplified features in the Galactic models.²

Another case motivating this concern is the IMF in brown dwarf mass range of $M < 0.08 M_{\odot}$, parameterized by a slope, α_{bd} , with $dN/dM \propto M^{-\alpha_{\text{bd}}}$, and inferred by the t_{E} distribution from the OGLE-IV survey (Mróz et al. 2017). Although Mróz et al. (2017) shows the likelihood peak at $\alpha_{\text{bd}} \sim 0.8$ using the Galactic model based on Han & Gould (1995, 2003) with simplified disk kinematics, Specht et al. (2020) shows the likelihood peak at $\alpha_{\text{bd}} = -0.1$, and 0.8 (-0.8 in their definition) is significantly disfavored according to their Figure 4. Specht et al. (2020) used the Besançon model (Robin et al. 2003, 2012, 2017) for their analysis using a more realistic model for disk kinematics. However, the Besançon model also has some unrealistic features, as discussed by Penny et al. (2019), such as the small Galactic bar angle of 13° compared to 25° – 30° implied by other observations (see a review by Bland-Hawthorn & Gerhard 2016). Further, the IMF for bulge stars in the public version has a minimum mass at $0.15 M_{\odot}$, a too massive cut-off for applying microlensing analysis, which is sensitive down to planetary-mass objects.

Several non-parametric dynamical models of our Galaxy are developed with the aid of N -body simulations (Wegg & Gerhard 2013; Portail et al. 2015, 2017). These models are better than parametric models with respect to consistency with the dynamics, but they have limited resolution. Numerical models use particles of thousands of solar masses and it is not easy to employ these models for simulations of microlensing events along a specific line of sight. Also, they are not open to communities outside the group, and thus not useful in terms of accessibility or difficulty of reproduction. A recent version of the Besançon model uses results from an N -body simulation (Gardner et al. 2014) for the kinematics of bulge stars, and it is difficult for other people to reproduce the model for their own use.

In this study, we develop a parametric Galactic model by fitting to spatial distributions of the median velocity and velocity dispersion from Gaia DR2 (Gaia Collaboration et al. 2018), OGLE-III red clump (RC) star count (Nataf et al. 2013), VIRAC proper motion data (Smith et al. 2018; Clarke et al. 2019), BRAVA radial velocity data (Rich et al. 2007; Kunder et al. 2012), and the OGLE-IV star count and microlensing event data (Mróz et al. 2017, 2019). We parameterize the model with 40–48 parameters depending on the selected options for the bulge density profile, and we present

² In Section 6.1, we show that our improved Galactic model does not have a significant effect on the results of Koshimoto & Bennett (2020) that were calculated with simplified Galactic models.

the best-fit values for all the parameters to enable ease of reproduction or make further updates. Our model aims to fulfill the gap in the market between the simplified parametric models used for microlensing studies and dynamical models based on N -body simulations that are difficult to use for microlensing work.

This model enables, for the first time, simultaneous measurements of the three slopes over entire mass range in a broken power law IMF of $dN/dM \propto M^{-\alpha}$, $\alpha_{\text{bd}} = 0.22_{-0.55}^{+0.20}$ in $M < 0.08 M_{\odot}$, $\alpha_{\text{ms}} = 1.16_{-0.15}^{+0.08}$ in $0.08 M_{\odot} \leq M < M_{\text{br}}$, and $\alpha_{\text{hm}} = 2.32_{-0.10}^{+0.14}$ in $M \geq M_{\text{br}}$, as well as a break mass at $M_{\text{br}} = 0.90_{-0.14}^{+0.05} M_{\odot}$. The IMF corresponds to the stellar mass-to-light ratio in K -band of $\Upsilon_K = 0.72_{-0.02}^{+0.05} M_{\odot}/L_{K_{\odot}}$, which is significantly different from $\Upsilon_K = 1.04 M_{\odot}/L_{K_{\odot}}$ with the [Kroupa \(2001\)](#) IMF for local stars but consistent with $\Upsilon_K = 0.75 M_{\odot}/L_{K_{\odot}}$ with the [Zoccali et al. \(2000\)](#) IMF for bulge stars. We estimated the dark matter mass inside the VVV bulge box ($\pm 2.2 \times \pm 1.4 \times \pm 1.2$ kpc, [Wegg & Gerhard 2013](#)) of $M_{\mathcal{DM}} = 0.45_{-0.06}^{+0.02} \times 10^{10} M_{\odot}$ by comparing our Υ_K value with those of the five versions of dynamical Galactic models in [Portail et al. \(2015\)](#). This is consistent with another independent estimate of $M_{\mathcal{DM}} = 0.51_{-0.11}^{+0.12} \times 10^{10} M_{\odot}$ derived by combining our estimate on the stellar mass inside the VVV bulge box of $1.34_{-0.11}^{+0.10} \times 10^{10} M_{\odot}$ and the dynamical mass in the same region of $(1.85 \pm 0.05) \times 10^{10} M_{\odot}$ constrained by [Portail et al. \(2017\)](#).

Using the developed models, we repeated a part of the analysis by [Koshimoto & Bennett \(2020\)](#) and confirmed their finding of a significant discrepancy between the predicted and observed π_{E} distributions with the new model, although the predicted π_{E} distribution significantly differed from the previous one. Further, we applied the model to calculate the lens-source proper motion μ_{rel} prior for OGLE-2011-BLG-0950, the only ambiguous event suffering from degeneracy between the planetary and binary solutions out of the 29 events in the [Suzuki et al. \(2016\)](#) combined sample. Our prior probability distribution for μ_{rel} indicates that the binary solution is more probable than the planetary solution.

This paper is organized as follows. In Section 2, we describe our parametric Galactic model and introduce all of the 40–48 fit parameters. Fitting to the Gaia DR2 data is conducted to determine the 10 parameters for the disk velocity model in Section 3. Fitting to the other data, which is toward the bulge sky, is separately conducted in Section 4 to determine the 26–34 parameters for the bulge density and velocity models, as well as the 4 parameters for the IMF model, where the determined disk velocity model is used in the fit. In Section 5, we discuss the determined parameters by comparing them with previous studies. We apply the developed Galactic models to microlensing analysis in Section 6. Section 7 presents the summary and conclusion.

2. MODEL PARAMETERIZATION

In this section, we describe our parametric Galactic model with a barred bulge and a multi-component of the stellar thin and thick disks. We disregard a stellar halo in this study because it rarely contributes to the considered data, which are mostly toward the Galactic bulge. We refer to a bar with a rigid-body rotation as the ‘bulge’ while an inner part of our Galaxy as the ‘bulge region,’ which means stars in the bulge region refer to both the bulge and disk stars present there. These Galactic structures consist of stars with mass functions (Section 2.1) and have the density and velocity distributions as functions of the Galactocentric coordinate (x, y, z) or Galactocentric cylindrical coordinate (R, ϕ, z) . We use different density and velocity distributions for each component, where we use ρ_{d} and v_{d} to refer to the disk density and velocity, respectively (Section 2.2), and ρ_{B} and v_{B} to refer to the bulge density and velocity, respectively (Section 2.3).

Here we introduce 4 fit parameters to model the stellar mass function, 10 fit parameters to model the v_d distribution, 7–15 fit parameters to model the ρ_B distribution, and 19 fit parameters to model the v_B distribution, respectively. Whereas the ρ_d model does not contain any fit parameters, two options of flat-scale and linear-scale height models are introduced for the thin disk. The 10 parameters for the v_d distribution are determined by fitting to the Gaia DR2 data (Gaia Collaboration et al. 2018) in Section 3, while the other 30–38 parameters are determined in Section 4 by fitting to the other data toward the bulge sky, namely the OGLE-III red clump star count (Nataf et al. 2013), VIRAC proper motion data (Smith et al. 2018; Clarke et al. 2019), BRAVA radial velocity data (Rich et al. 2007; Kunder et al. 2012), and OGLE-IV star count and microlensing event data (Mróz et al. 2017, 2019).

The OGLE-III red clump star count data from Nataf et al. (2013) is sensitive to the Sun’s Galactic position and the bar angle. In fact, Cao et al. (2013) used the same dataset to measure the distance to the Galactic center of 8.1–8.2 kpc and the bar angle of 27–32 deg. However, because the number of fit parameters is already large, 40 to 48, we fix these two parameters to mitigate degeneracies among fit parameters. For the solar position in our Galaxy, we use $R_\odot = 8160$ pc, which is consistent with a recent precise measurement of $8178 \pm 13_{\text{stat.}} \pm 22_{\text{sys.}}$ pc on the distance to Sgr A* (Gravity Collaboration et al. 2019), and $z_\odot = 25$ pc (Bland-Hawthorn & Gerhard 2016). We use $\alpha_{\text{bar}} = 27^\circ$ for the bar angle (Wegg & Gerhard 2013; Bland-Hawthorn & Gerhard 2016). The R_\odot and α_{bar} values are consistent with the OGLE-III red clump star count data because these two values are both within the above respective ranges derived by Cao et al. (2013). Thus, this choice generates no tension.

We also fix the solar velocity to be $(v_{\odot,x}, v_{\odot,y}, v_{\odot,z}) = (-10, 243, 7)$ km/s (Bland-Hawthorn & Gerhard 2016). The tangential velocity $v_{\odot,y} = 243$ km/s is marginally lower than 248 ± 3 km/s suggested by Bland-Hawthorn & Gerhard (2016) (a recent thorough review paper on our Galaxy) because we found a better agreement to the VIRAC proper motion data with 243 km/s. This is consistent with Clarke et al. (2019), who found that the dynamical model of Portail et al. (2017), with a slower tangential velocity of $v_{\odot,y} = 245$ km/s, gave an improved match to the VIRAC proper motion data, compared to the original value of $v_{\odot,y} = 250.24$ km/s used by Portail et al. (2017).

2.1. Stellar Mass Function

The stellar mass function refers to a present-day mass function, which can be calculated by a combination of IMF, star formation rate, and initial–final mass relationships for remnants, i.e., for white dwarfs, neutron stars, and black holes. Here, we introduce the IMF, star formation rate, and initial–final mass relationships used in this paper.

We use a broken-power law form IMF given by

$$\frac{dN}{dM} \propto \begin{cases} M^{-\alpha_{\text{hm}}} & \text{when } M_{\text{br}} < M < 120 M_\odot \\ M^{-\alpha_{\text{ms}}} & \text{when } 0.08 M_\odot \leq M < M_{\text{br}} \\ M^{-\alpha_{\text{bd}}} & \text{when } 10^{-3} M_\odot \leq M < 0.08 M_\odot . \end{cases} \quad (4)$$

We use four parameters, the three slopes ($\alpha_{\text{hm}}, \alpha_{\text{ms}}, \alpha_{\text{bd}}$) and a break mass M_{br} , as fit parameters in Section 4, and fit them to the data including the OGLE-IV microlensing t_E distribution, which has a sensitivity to objects with brown dwarf mass to black hole mass. By contrast, we use the local IMF by Kroupa (2001), $(\alpha_{\text{hm}}, \alpha_{\text{ms}}, \alpha_{\text{bd}}) = (2.30, 1.30, 0.30)$ with $M_{\text{br}} = 0.50 M_\odot$, in the fit to the

Gaia DR2 data, in Section 3, to derive the values of the local density for red giants, which are listed in Table 1. We selected different IMF values because the Gaia data are dominated by local stars, whereas the data used in Section 4 are dominated by bulge stars.

Further, a star formation rate $\propto \exp[-\frac{T}{7\text{Gyr}}]$ (Bovy 2017) is applied to the thin disk star, where T is stellar age, while we assume a mono-age thick disk at $T = 12$ Gyr (Robin et al. 2014) and the Gaussian distribution of 9 ± 1 Gyr (Koshimoto et al. 2020) for the bulge stars. The PARSEC isochrone models (Bressan et al. 2012; Chen et al. 2014; Tang et al. 2014) are used for the stellar lifetime of a given initial mass.

For initial–final mass relationships of remnants, we apply the model used by Lam et al. (2020), where a linear relation of Kalirai et al. (2008), $M_{\text{WD}} = 0.109M_{\text{ini}} + 0.394M_{\odot}$, is used for white dwarfs and a modified probabilistic relation based on Raithel et al. (2018) is used for neutron stars and black holes. See Appendix C of Lam et al. (2020) and references therein for more details. Further, we add a birth kick velocity in a random direction of 350 km/s or 100 km/s to the velocity of the progenitor star for a neutron star or a black hole, respectively (Lam et al. 2020).

2.2. Galactic Disk Model

In this subsection, we describe the density and velocity models of a thin and a thick disk, where the thin disk is further divided into seven components depending on ages following the classification by Robin et al. (2003). These seven plus one components have different scale height values and velocity dispersions. The velocity dispersions differ from each other depending on the 10 fit parameters introduced in the v_d model and determined later in Section 3. The disk model contributes to both fits in Sections 3 and 4.

2.2.1. Disk density (ρ_d model)

A thin and a thick disk are considered with density profiles of

$$\rho_d^{\text{thin}}(R, z) = \begin{cases} \rho_{d,\odot}^{\text{thin}} \frac{z_{d,\odot}^{\text{thin}}}{z_d^{\text{thin}}(R)} \exp\left(-\frac{R-R_{\odot}}{R_d^{\text{thin}}}\right) \text{sech}^2\left(-\frac{|z|}{z_d^{\text{thin}}(R)}\right) & \text{if } R > R_{d,\text{break}} \\ \rho_{d,\odot}^{\text{thin}} \frac{z_{d,\odot}^{\text{thin}}}{z_d^{\text{thin}}(R)} \exp\left(-\frac{R_{d,\text{break}}-R_{\odot}}{R_d^{\text{thin}}}\right) \text{sech}^2\left(-\frac{|z|}{z_d^{\text{thin}}(R)}\right) & \text{if } R \leq R_{d,\text{break}} \end{cases} \quad (5)$$

$$\rho_d^{\text{thick}}(R, z) = \begin{cases} \rho_{d,\odot}^{\text{thick}} \exp\left(-\frac{R-R_{\odot}}{R_d^{\text{thick}}}\right) \exp\left(-\frac{|z|}{z_{d,\odot}^{\text{thick}}}\right) & \text{if } R > R_{d,\text{break}} \\ \rho_{d,\odot}^{\text{thick}} \exp\left(-\frac{R_{d,\text{break}}-R_{\odot}}{R_d^{\text{thick}}}\right) \exp\left(-\frac{|z|}{z_{d,\odot}^{\text{thick}}}\right) & \text{if } R \leq R_{d,\text{break}}, \end{cases} \quad (6)$$

where $\rho_{d,\odot}$ is the stellar density in the solar neighborhood, hereafter referred to as the local (stellar) density, R_d is the disk scale length, and z_d is the disk scale height.

The disk profile in the inner Galaxy region is still uncertain. A constant surface density model is adopted within $R < R_{d,\text{break}}$ following the findings of Portail et al. (2017) who developed an N -body dynamical model reproducing extensive photometric and kinematic data across our Galaxy. In their model, the disk has an exponential feature in the outer part of our Galaxy ($\gtrsim 5$ kpc) while it has a flat surface density feature in the inner part ($\lesssim 5$ kpc). We use $R_{d,\text{break}} = 5.3$ kpc for our model.

For the thin disk scale height z_d^{thin} , two options are considered: a flat- and a linear-scale height model. We adopt

$$z_d^{\text{thin}}(R) = \begin{cases} z_{d,\odot}^{\text{thin}} - (z_{d,\odot}^{\text{thin}} - z_{d,4.5}^{\text{thin}}) \frac{R_{\odot}-R}{R_{\odot}-4.5\text{kpc}} & \text{if } R > 4.5 \text{ kpc} \\ z_{d,4.5}^{\text{thin}} & \text{if } R \leq 4.5 \text{ kpc} \end{cases} \quad (7)$$

Table 1. Scale lengths, scale heights and local densities for thin and thick disks.

	Age T	R_d	$z_{d,\odot}$	$z_{d,4.5}$ ^a	$\rho_{d,\odot}^{\text{MS}}$ ^b	$\rho_{d,\odot}^{\text{WD}}$ ^b	$n_{d,\odot}^{\text{RG}}$ ^b
	[Gyr]	[pc]	[pc]	[pc]	$[M_\odot \text{ pc}^{-3}]$	$[M_\odot \text{ pc}^{-3}]$	$[\text{pc}^{-3}]$
Thin disk	0 - 0.15	5000	61	36	5.1×10^{-3}	5.5×10^{-5}	6.9×10^{-6}
	0.15 - 1	2600	141	85	5.0×10^{-3}	2.2×10^{-4}	3.3×10^{-5}
	1 - 2	2600	224	134	3.8×10^{-3}	2.9×10^{-4}	4.2×10^{-5}
	2 - 3	2600	292	175	3.2×10^{-3}	3.3×10^{-4}	2.1×10^{-5}
	3 - 5	2600	372	223	5.9×10^{-3}	7.8×10^{-4}	6.5×10^{-5}
	5 - 7	2600	440	264	6.3×10^{-3}	1.0×10^{-3}	6.1×10^{-5}
	7 - 10	2600	445	267	1.3×10^{-2}	2.4×10^{-3}	1.3×10^{-4}
Sum/Mean			329	197	4.2×10^{-2}	5.1×10^{-3}	3.6×10^{-4}
Thick disk	12	2200	903		1.7×10^{-3}	4.4×10^{-4}	9.1×10^{-6}

^aFor the linear scale height model.

^bLocal densities are given for main sequence stars (MS, including brown dwarfs), white dwarfs (WD), and red giants (RG). In the fit in Section 4, the values are updated with a given IMF.

NOTE— R_d refers to R_d^{thin} in the lines for thin disk, and R_d^{thick} in the line for thick disk. The same is true for $z_{d,\odot}$, $z_{d,4.5}$, $\rho_{d,\odot}$, and $n_{d,\odot}$.

for the linear-scale height model with $z_{d,4.5}^{\text{thin}} = 0.6 z_{d,\odot}^{\text{thin}}$ (Wegg et al. 2016) while for the flat-scale height model $z_d^{\text{thin}}(R) = z_{d,\odot}^{\text{thin}}$ is used. Two options have been considered as we were motivated by a similar attempt of Wegg et al. (2016) who considered the linear-scale height model to smoothly connect the disk to the inner thin long bar with a scale height of ~ 200 pc suggested by Wegg et al. (2015). As described in Section 2.3.1, adding the long bar component to our bulge model did not result in a significant improvement. However, whether we used the flat- or linear-scale height model in the disk model did affect χ^2 or $\tilde{\chi}^2$ values in the fit.

The thin disk is divided into 7 components depending on the age (T) following the Besançon model (Robin et al. 2003, 2012, 2017). Table 1 lists the scale length and height values for each component of the thin and thick disks. The scale height for each component is calculated using the age-scale height relation for the axis ratio ϵ , that is $\epsilon = \text{Min}[0.0791, 0.104\sqrt{(T/\text{Gyr} + 0.1)/10.1}]$ (Sharma et al. 2014). Because ϵ is designed as the ratio of the scale height to the scale length in a disk with Einasto laws (Einasto 1979), we used the surface-to-volume density ratio in the Einasto disk calculated with ϵ to derive the $z_{d,\odot}$ value for each component.

Table 1 also lists the local stellar density values for main sequence stars, white dwarfs, and red giants for each disk component. The total thin disk local mass density is normalized by $4.2 \times 10^{-2} M_\odot \text{ pc}^{-3}$ for main sequence stars (Bovy 2017), while the thick disk local mass density is normalized so that its local contribution to the thin disk becomes 4% (Bland-Hawthorn & Gerhard 2016).

The local density value for stars at each evolutionary stage in each disk component is calculated using the local IMF by Kroupa (2001) combined with the star formation rate and the initial–final mass relationship described in Section 2.1. The red giants are selected based on their absolute magnitude

$M_G < 3.9$ mag and intrinsic color $(G_{BP} - G_{RP})_0 > 0.95$ in the Gaia bands using the PARSEC isochrones (Bressan et al. 2012; Chen et al. 2014; Tang et al. 2014). This criteria for red giants is same as that used for the selection of the giant sample by Gaia Collaboration et al. (2018), and the $n_{d,\odot}^{RG}$ values listed in the table are used in the fit to the Gaia DR2 data in Section 3.

An important note here is that the local density values are updated with a given IMF and are different in the fit in Section 4. This apparent inconsistent treatment can be partially justified by considering that our IMF presented in Section 4 is for the disk stars located in the inner Galaxy region ($R \lesssim 4$ kpc) contributing to the data used in Section 4, and the Kroupa (2001) IMF is appropriate for the nearby stars ($R \gtrsim 4$ kpc) contributing to the Gaia data used in Section 3.

The local surface density with the Kroupa (2001) IMF is $30.01 M_\odot \text{ pc}^{-2}$ for main sequence stars, which is compared with the measurements of $23.0 \pm 1.5 M_\odot \text{ pc}^{-2}$ (Bovy 2017) and $28.2 \pm 2.7 M_\odot \text{ pc}^{-2}$ (McKee et al. 2015). The local surface density of white dwarfs is $4.87 M_\odot \text{ pc}^{-2}$, and this is consistent with measurements of $5 \pm 1 M_\odot \text{ pc}^{-2}$ (Bovy 2017) and $4.9 \pm 0.6 M_\odot \text{ pc}^{-2}$ (McKee et al. 2015). The local number density of red giants is $3.6 \times 10^{-4} \text{ pc}^{-3}$, and this fairly well agrees with the measurement by Bovy (2017) of $(3.9 \pm 0.1) \times 10^{-4} \text{ pc}^{-3}$.

2.2.2. Disk kinematics (v_d model)

Our work is highly motivated by Gaia DR2 (Gaia Collaboration et al. 2018) in which skewed distributions for the azimuthal velocity v_ϕ and clear dependencies of the velocity dispersion and mean azimuthal velocity of disk stars on their location are shown. Such disk kinematic structures have not been included in most of the models used for microlensing analysis like the three models (Sumi et al. 2011; Bennett et al. 2014; Zhu et al. 2017) used in Koshimoto & Bennett (2020). To include those dependencies as a function of the Galactocentric cylindrical coordinate (R, ϕ, z) in addition to a skewed v_ϕ distribution, we follow the parameterization of a disk velocity model by Sharma et al. (2014).

We assume that the Galaxy is in a dynamical equilibrium, and use a modified Shu distribution function (DF) model developed by Schönrich & Binney (2012) and Sharma & Bland-Hawthorn (2013) to represent the distribution of disk azimuthal velocity $v_{d,\phi}$. Gaussian velocity models are used for $v_{d,\phi}$ distributions in other Galactic models for microlens analysis (Sumi et al. 2011; Bennett et al. 2014; Zhu et al. 2017; Jung et al. 2018) and in the Besançon model (Robin et al. 2003, 2012, 2017). However, a real v_ϕ distribution is highly skewed to low v_ϕ (e.g., Nordström et al. 2004; Gaia Collaboration et al. 2018), and the Shu DF (Shu 1969) provides a much better approximation for it (Binney & Tremaine 2008; Sharma et al. 2014; Bland-Hawthorn & Gerhard 2016).

We introduce the guiding-center radius R_g as the radius of a circular orbit with specific angular momentum L_z , i.e., $R_g = L_z/v_c$, where v_c is the circular velocity (Binney & Tremaine 2008). The modified Shu DF model provides a joint distribution of the Galactocentric radius R and R_g ,

$$P(R, R_g) = \frac{(2\pi)^2 \Sigma(R_g)}{g\left(\frac{1}{2a^2}\right)} \exp\left[\frac{2 \ln(R_g/R) + 1 - R_g^2/R^2}{2a^2}\right], \quad (8)$$

where $a = \sigma_{v_{d,R}}(R_g)/v_c$, $g(c) = \frac{e^c \Gamma(c-1/2)}{2c^{c-1/2}}$ with the velocity dispersion along radial direction $\sigma_{v_{d,R}}(R) = \sigma_{R,\odot} \exp\left[-\frac{R-R_\odot}{R\sigma_R}\right]$ and the Gamma function $\Gamma(x)$. R_{σ_R} is the scale length for the $\sigma_{v_{d,R}}(R)$ distribution given by Eqs. (11)-(12) below. $\Sigma(R_g)$ is a function that controls disk surface density, and we use an

empirical formula proposed by [Sharma & Bland-Hawthorn \(2013\)](#),

$$\Sigma(R_g) = \frac{e^{-R_g/R_d}}{2\pi R_d^2} - \frac{c_3 a_0^{c_4}}{R_d^2} \times s \left(\frac{R_g}{c_1 R_d (1 + q/c_2)} \right), \quad (9)$$

where $s(x) = 31.53e^{-x/0.2743}((x/0.6719)^2 - 1)$ and $q = R_d/R_{\sigma_R}$. We select $(c_1, c_2, c_3, c_4) = (3.822, 0.524, 0.00567, 2.13)$ from Table 1 of [Sharma & Bland-Hawthorn \(2013\)](#) that is for the rising rotation curve of $v_c \propto (R/R_d)^{0.2}$. This is because we use a similar rising rotation curve of $v_c(R)$ from [Bland-Hawthorn & Gerhard \(2016\)](#), which comes from the N -body dynamical model of [Portail et al. \(2015\)](#) for $R_d = 2.6$ kpc.

A conditional probability for R_g given R , $P(R_g|R)$, which is calculated using Eq. (8), is used to model the disk azimuthal velocity $v_{d,\phi}$ distribution through the relation between $v_{d,\phi}$ and R_g ,

$$\begin{aligned} v_{d,\phi}(R, z) &= v_c(R_g, z)R_g/R \\ &= \frac{v_c(R_g)R_g/R}{1 + 0.0374|z/\text{kpc}|^{1.34}}, \end{aligned} \quad (10)$$

where we apply $v_c(R, z) = v_c(R)(1 + 0.0374|z/\text{kpc}|^{1.34})^{-1}$ ([Sharma et al. 2014](#)) for the vertical dependency of v_c . Again, the rotation curve from [Bland-Hawthorn & Gerhard \(2016\)](#) is used for $v_c(R)$.

For the disk velocity along radial ($v_{d,R}$) and vertical ($v_{d,z}$) directions, we use the Gaussian distribution with mean velocity of 0 (i.e. dynamical equilibrium) with the velocity dispersion given by

$$\sigma_{v_{d,i}}^{\text{thin}}(R) = \sigma_{i,\odot}^{\text{thin}} \left(\frac{T + T_{\min}}{T_{\max} + T_{\min}} \right)^{\beta_i} \exp \left[-\frac{R - R_\odot}{R_{\sigma_i}^{\text{thin}}} \right] \quad (11)$$

for the thin disk and

$$\sigma_{v_{d,i}}^{\text{thick}}(R) = \sigma_{i,\odot}^{\text{thick}} \exp \left[-\frac{R - R_\odot}{R_{\sigma_i}^{\text{thick}}} \right] \quad (12)$$

for the thick disk, where i takes R or z , and we use $T_{\min} = 0.01$ Gyr and $T_{\max} = 10$ Gyr in this study. Further, we introduce the dependence on stellar age T for the thin disk to include the age-velocity dispersion relation owing to secular heating in the disk. With this formula, the local velocity dispersion value calculated for thin disk, $\sigma_{i,\odot}^{\text{thin}}$, is for stars with $T = 10$ Gyr.

In Section 3.3, we investigate acceptable combinations of the following 10 fit parameters by comparing with the data from the giant sample by [Gaia Collaboration et al. \(2018\)](#); the local velocity dispersion values, $\sigma_{i,\odot}^{\text{thin}}$ and $\sigma_{i,\odot}^{\text{thick}}$, slope of age-velocity dispersion relation, β_i , and scale lengths of the velocity dispersion distribution, $R_{\sigma_i}^{\text{thin}}$ and $R_{\sigma_i}^{\text{thick}}$, where i takes R or z . Note that additional parameters are not needed to represent the distribution of velocity dispersion along the azimuthal direction, such as the above parameters with $i = \phi$, because Eq. (8) naturally relates the $v_{d,\phi}$ distribution to the $v_{d,R}$ distribution.

2.3. Barred Bulge Model

Compared to the disk model, an analytical approximated expression for the bulge dynamical model is less developed because of its difficulty in the treatment of a non-axisymmetric property of the

bar. An N -body model is dynamically correct; however, fitting the model to the observational data is difficult. A probable optimal technique is a made-to-measure method (Syer & Tremaine 1996), where weights of particles are updated such that observables of the model match a given dataset during the simulation. Portail et al. (2017) developed an N -body dynamical model matching extensive photometric and kinematic data across our Galaxy using the made-to-measure method. However, such a dynamical simulation is beyond the scope of this study because we aim to develop a parametric Galactic model, which can be easily implemented, reproduced, and updated by anybody. Although some studies developed parametric models for the bar (Dwek et al. 1995; Rattenbury et al. 2007b; Robin et al. 2012; Cao et al. 2013), they lack constraints from some recent data such as the one by Mróz et al. (2019), who performed the largest statistical study for single-lens microlensing events through the OGLE-IV Galactic bulge survey, which is especially important for microlensing studies.

In this subsection, we describe our parameterization for the bulge density (ρ_B) and velocity (v_B) models. We consider a total of four different shapes for the ρ_B model: two ‘one-component’ models and two ‘two-components’ models, in which 7 and 15 fit parameters are introduced, respectively. The one-component model is designed following the parameterization used in the previous studies (Dwek et al. 1995; Rattenbury et al. 2007b; Robin et al. 2012; Cao et al. 2013), while the two-components model is designed to express the X-shape structure (Nataf et al. 2010), which is not considered in the previous parametric models. We consider a bar’s rigid-body rotation and a streaming motion in the v_B model and introduce 19 fit parameters to model it. Note that the bulge model contributes to the fits in Section 4 rather than those in Section 3.

2.3.1. Bulge density (ρ_B model)

Our one-component bulge model follows the parameterization by Robin et al. (2012), in which we consider each of E (exponential) and G (Gaussian) models given by

$$\rho_B^{(i)} = \rho_{0,B} f_i(x', y', z'; \mathbf{p}_{r_s}) \text{Cut} \left[\frac{R - R_c}{0.5 \text{ kpc}} \right] \quad (i = \text{E, G}), \quad (13)$$

where $\text{Cut}(x)$ is a cut-off function given by

$$\text{Cut}(x) = \begin{cases} \exp(-x^2) & \text{if } x > 0 \\ 1 & \text{if } x \leq 0 \end{cases} \quad (14)$$

and R_c is the cut-off radius. The two functions, $f_E(x', y', z'; \mathbf{p}_{r_s})$ and $f_G(x', y', z'; \mathbf{p}_{r_s})$, are defined as

$$\begin{aligned} f_E(x', y', z'; \mathbf{p}_{r_s}) &= \exp[-r_s(x', y', z'; \mathbf{p}_{r_s})], \\ f_G(x', y', z'; \mathbf{p}_{r_s}) &= \exp[-0.5r_s^2(x', y', z'; \mathbf{p}_{r_s})] \end{aligned} \quad (15)$$

with

$$r_s(x', y', z'; \mathbf{p}_{r_s}) = \left\{ \left[\left(\frac{x'}{x_0} \right)^{C_\perp} + \left(\frac{y'}{y_0} \right)^{C_\perp} \right]^{C_\parallel/C_\perp} + \left(\frac{z'}{z_0} \right)^{C_\parallel} \right\}^{1/C_\parallel} \quad (16)$$

and $\mathbf{p}_{r_s} = (x_0, y_0, z_0, C_\perp, C_\parallel)$. We use (x', y', z') to refer to a Galactocentric coordinate system rotated around the z -axis by an angle α_{bar} such that the x' axis is aligned with the major axis of the Galactic bar, where $\alpha_{\text{bar}} = 27^\circ$ is applied as the bar angle. The parameters (x_0, y_0, z_0) are the scale lengths along (x', y', z') axes, and C_\perp and C_\parallel allow the bar to take various shapes (Robin et al. 2012).

Motivated by the X-shape structure confirmed both observationally and dynamically (McWilliam & Zoccali 2010; Nataf et al. 2010; Wegg & Gerhard 2013), we consider a two-components model, $\rho_B = \rho_B^{(i)} + \rho_X^{(j)}$, where $\rho_B^{(i)}$ is given by Eq. (13) and

$$\rho_X^{(j)} = \rho_{0,X} [f_j(x' - b_X z', y', z'; \mathbf{p}_{r_s,X}) + f_j(x' + b_X z', y', z'; \mathbf{p}_{r_s,X})] \text{Cut} \left[\frac{R - R_{c,X}}{0.5 \text{ kpc}} \right] \quad (j = E, G). \quad (17)$$

The parameter b_X controls the slope of an X-shape, and we use another parameter set, $\mathbf{p}_{r_s,X} = (x_{0,X}, y_{0,X}, z_{0,X}, C_{\perp,X}, C_{\parallel,X})$, which is different from the \mathbf{p}_{r_s} for the first component given by Eq. (13). Note that the X-shape structure with this expression is centered on the Galactic center, although Portail et al. (2015) found a slightly off-centered X-shape structure in their N -body dynamical model. We considered all four combinations of $i = E, G$ and $j = E, G$, and found no significant difference among those combinations with respect to agreement with the fitted data. Hence, herein, we present results of two combinations of $(i, j) = (E, E)$ and (G, G) among the four. Hereafter, we refer to these models as the E+E_X and G+G_X models, respectively.

Furthermore, other structures known in the bulge region are locally significant but not captured by either of the four ρ_B models. For example, a nuclear stellar disk exists in a central sub-kpc region (Launhardt et al. 2002; Nishiyama et al. 2013; Portail et al. 2017). The scale height and the outer edge of the nuclear stellar disk are ~ 45 pc (Nishiyama et al. 2013) and ~ 230 pc (Bland-Hawthorn & Gerhard 2016), respectively, which indicates no influence on the used data in this study ranged in $|b| \gtrsim 2^\circ$. A long bar component was found to be distributed in the outer bulge region along the major axis by Wegg et al. (2015); hence, it was added in our model to observe its effect, but no significant improvement was observed regarding the $\tilde{\chi}_{\text{sum}}^2$ value defined in Section 4.3. This is probably because the used data lacks the sky region in $|l| > 10^\circ$, where the long bar component becomes prominent. Therefore, we consider each of the E, G, E+E_X and G+G_X models with no additional components.

The 7 fit parameters for the E and G models are: $x_0, y_0, z_0, C_\perp, C_\parallel, R_c$, and $\rho_{0,B}$. In the E+E_X and G+G_X models, the additional 8 fit parameters are: $x_{0,X}, y_{0,X}, z_{0,X}, C_{\perp,X}, C_{\parallel,X}, R_{c,X}, b_X$, and $f_{0,X}$, where $f_{0,X} \equiv \rho_{0,X}/\rho_{0,B}$.

2.3.2. Bulge kinematics (v_B model)

For the velocity distribution of the bulge star, we use the Gaussian distribution with a mean velocity and velocity dispersion, both varying as a function of (x', y', z') . The mean velocity is calculated by combining the rigid-body rotation of the bar and streaming motion along the bar. We denote the angular velocity of the rigid-body rotation or the bar pattern speed by Ω_p and consider the streaming motion along the major axis as

$$v_{x'}^{\text{str}}(y') = v_0^{\text{str}} (1 - \exp[-(y'/y_0^{\text{str}})^2]), \quad (18)$$

where v_0^{str} is the streaming velocity at $y' \gg y_0^{\text{str}}$, and y_0^{str} is the scale length along y' axis. This form of distribution for the streaming motion is motivated by the bottom panels in Figure 14 of Sanders

et al. (2019a) that show the $v_{x'}^{\text{str}}$ of their dynamical model, which represents our Galaxy, increasing from $y' = 0$ to $|y'| > 0$ along y' axis.

For the velocity dispersion, we use

$$\sigma_{v_{\text{B}},i}(x', y', z') = \sigma_{v_{\text{B}},i,0} + \sigma_{v_{\text{B}},i,1} f_{\text{E}}(x', y', z'; \mathbf{p}_{r_s, \sigma_i}) \quad (i = x', y', z'), \quad (19)$$

where we apply $\mathbf{p}_{r_s, \sigma_{x'}} = \mathbf{p}_{r_s, \sigma_{y'}} \neq \mathbf{p}_{r_s, \sigma_{z'}}$ and denote the parameter set for $\sigma_{x'}$ and $\sigma_{y'}$ by $\mathbf{p}_{r_s, \sigma_R}$, i.e., $\mathbf{p}_{r_s, \sigma_R} = \mathbf{p}_{r_s, \sigma_{x'}} = \mathbf{p}_{r_s, \sigma_{y'}} = (x_{0, \sigma_R}, y_{0, \sigma_R}, z_{0, \sigma_R}, C_{\perp, \sigma_R}, C_{\parallel, \sigma_R})$. The constant $\sigma_{v_{\text{B}},i,0}$ provides a minimum value of $\sigma_{v_{\text{B}},i}$ while $\sigma_{v_{\text{B}},i,0} + \sigma_{v_{\text{B}},i,1}$ provides the maximum $\sigma_{v_{\text{B}},i}$ value at the Galactic center.

This model is not dynamically consistent with the density model described in Section 2.3.1; however, the profile of Eq. (19) peaking at the Galactic center and gradually decreasing as it goes around is motivated by the velocity dispersion field of the dynamical model of our Galaxy by Sanders et al. (2019a) illustrated in their Figure 15.

There are a total of 19 fit parameters for the velocity model; $\Omega_{\text{D}}, v_0^{\text{str}}, y_0^{\text{str}}, \sigma_{v_{\text{B}},i,0}, \sigma_{v_{\text{B}},i,1} (i = x', y', z'), x_{0, \sigma_R}, y_{0, \sigma_R}, z_{0, \sigma_R}, C_{\perp, \sigma_R}, C_{\parallel, \sigma_R}, x_{0, \sigma_{z'}}, y_{0, \sigma_{z'}}, z_{0, \sigma_{z'}}, C_{\perp, \sigma_{z'}},$ and $C_{\parallel, \sigma_{z'}}$.

3. FITTING FOR THE DISK VELOCITY PARAMETERS

In this section, we determine the 10 fit parameters for the v_{d} model by fitting our disk model to the spatial distribution of the median velocity and the velocity dispersion for giant stars in the Gaia DR2 (Gaia Collaboration et al. 2018), where the data are given in grids of 200 pc by 200 pc in (R, z) . Bulge stars rarely contribute to the Gaia data and the barred bulge model is not used in the fit in this section. The fit is conducted through a grid search. The disk model with the determined parameters in this section is used for the other fits in Section 4.

3.1. Gaia DR2 Velocity Data

We use the median velocity and velocity dispersion distributions of the red giant sample consisting of 3,153,160 sources by Gaia Collaboration et al. (2018) as a function of the Galactocentric radius R and the height from the Galactic plane z . The stars in this sample are selected based on their absolute magnitude $\mathcal{M}_G < 3.9$ mag and intrinsic color $(G_{\text{BP}} - G_{\text{RP}})_0 > 0.95$ in the Gaia bands. This is the same data plotted in Figure 11 of Gaia Collaboration et al. (2018), and we obtained the data through private communication with the lead author, D. Katz. The medians and dispersions are given in grids of 200 pc by 200 pc in (R, z) over $3340 \text{ pc} < R < 13340 \text{ pc}$, $-3400 \text{ pc} < z < 3400 \text{ pc}$. The center of (i_R, i_z) th grid is $(R, z) = (200 i_R + 3440, 200 i_z - 3300)$ pc. The total grids in the range of R and z are $50 \times 34 = 1700$; however, we do not use the grids with < 30 stars contributing to the statistics, which results in 1207 grids being available.

The medians of the v_R and v_z distribution are assumed as 0; hence, only the data of the median of the azimuthal velocity $\overline{v_{\phi}}$ and velocity dispersions along the three axes, σ_R, σ_{ϕ} , and σ_z , are used. The data distribution for these four parameters is plotted in the far-left panels in Fig. 1.

3.2. Definition of Goodness of Fit

The far-right column of Table 1 lists the local number density of red giants in our model, which is calculated using the same criteria as for the Gaia DR2 giant sample. We use these $n_{\text{d}, \odot}^{\text{RG}}$ values instead of $\rho_{\text{d}, \odot}$ in Eqs. (5)-(6) to calculate model values for the median $\overline{v_{\phi}}$ and the velocity dispersions σ_R, σ_{ϕ} , and σ_z . Thereafter, Monte Carlo random sampling is used to calculate the model values for each

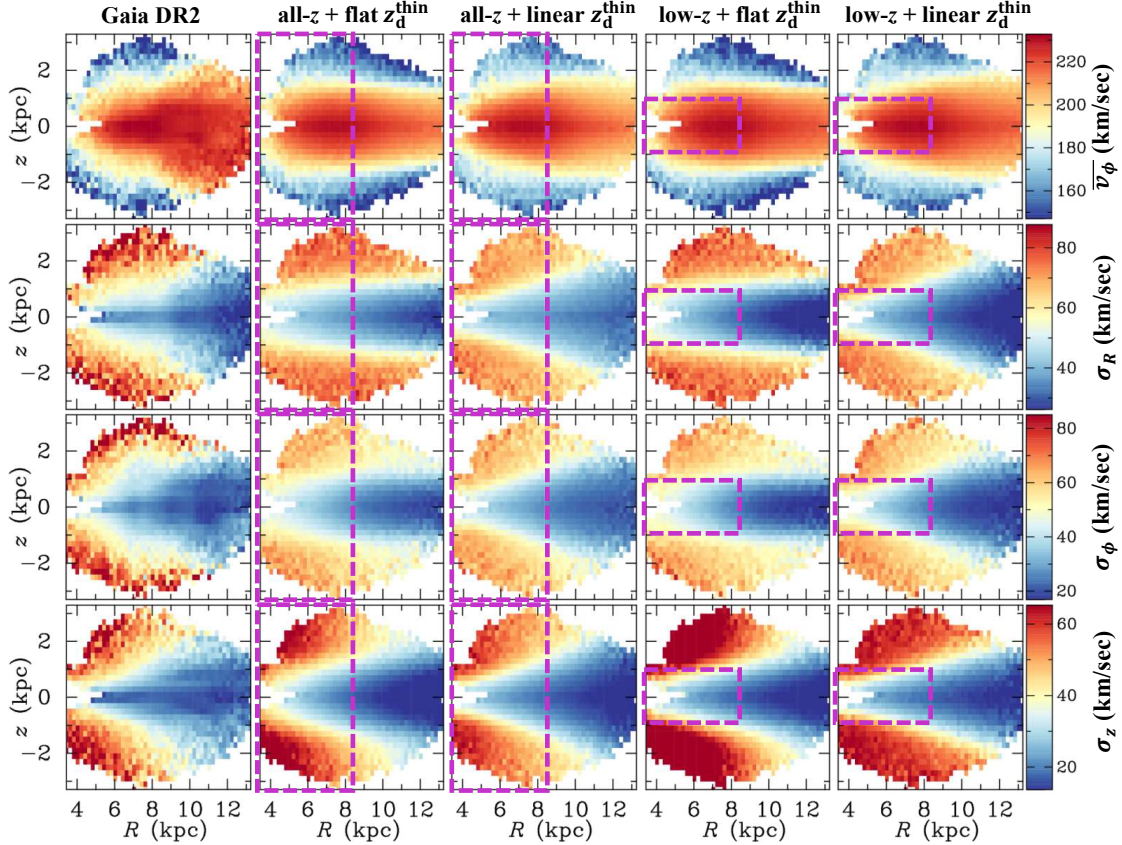


Figure 1. Far left: The Gaia DR2 giant sample’s R - z distributions for median azimuthal velocity ($\overline{v_\phi}$) and velocity dispersions along the radial (σ_R), azimuthal (σ_ϕ), and vertical (σ_z) directions from top to bottom (reproduction of Figure 11 of Gaia Collaboration et al. 2018). The right four columns: The same distributions from each indicated model. Only the grids inside the purple boxes are used in the calculation of $\tilde{\chi}^2$ for each model.

grid of the data with a particular combination of the 10 fit parameters, i.e., $\sigma_{i,\odot}^{\text{thin}}$, $\sigma_{i,\odot}^{\text{thick}}$, β_i , $R_{\sigma_i}^{\text{thin}}$, and $R_{\sigma_i}^{\text{thick}}$ ($i = R, z$). We assume that data incompleteness does not affect the kinematic statistics in each grid and do not consider the completeness correction for the comparison between the data and model values.

To evaluate an agreement with the data at (i_R, i_z) th grid, we use

$$\tilde{\chi}_{i_R, i_z}^2 = \sum_{p=\overline{v_\phi}, \sigma_R, \sigma_\phi, \sigma_z} w_{i_R, i_z} (p_{i_R, i_z}^{\text{simu}} - p_{i_R, i_z}^{\text{obs}})^2, \quad (20)$$

where

$$w_{i_R, i_z} = \frac{(1/N_{i_R, i_z}^{\text{obs}} + 1/N_{i_R, i_z}^{\text{simu}})^{-1}}{\sum_{j_R, j_z} (1/N_{j_R, j_z}^{\text{obs}} + 1/N_{j_R, j_z}^{\text{simu}})^{-1}}, \quad (21)$$

and $N_{i_R, i_z}^{\text{obs}}$ is the number of observed stars in a grid, while $N_{i_R, i_z}^{\text{simu}}$ is the number of simulated stars in the same grid. $N_{i_R, i_z}^{\text{obs}}$ takes 30–34243 depending on grid position, where the median is ~ 250 and 67 out of 1207 grids have $N_{i_R, i_z}^{\text{obs}} > 10^4$. The weight for each grid, w_{i_R, i_z} , disregards each measurement

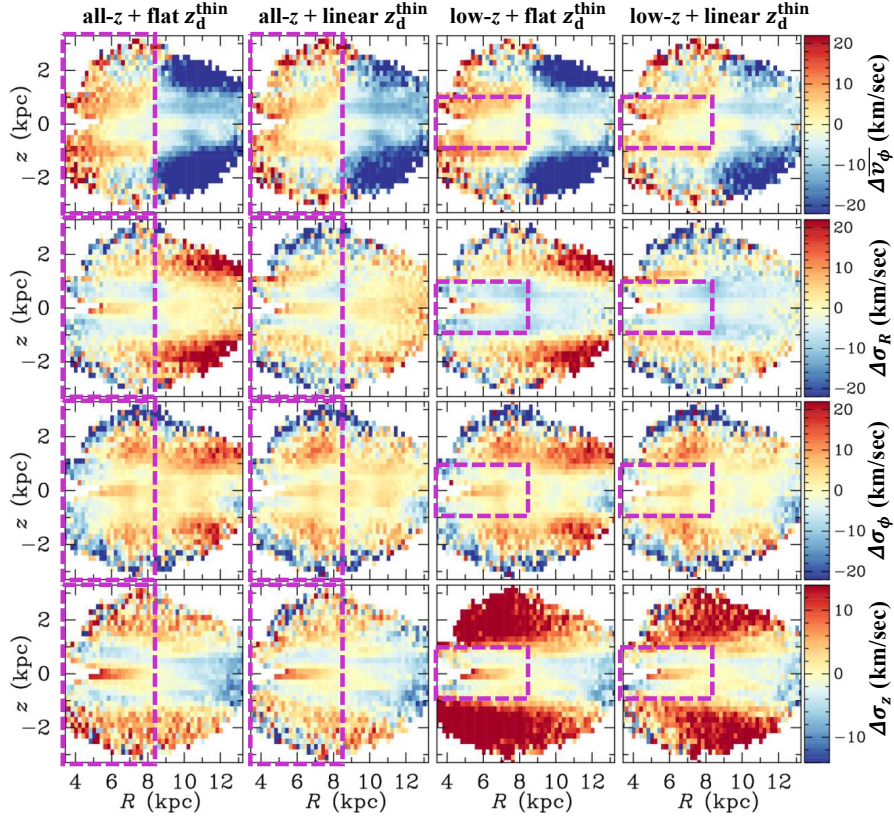


Figure 2. Residuals (model – data) corresponding to the four models plotted in Fig. 1.

uncertainty because we were not provided the uncertainties of measurements of the median velocity and velocity dispersion through the private communication. This corresponds to an assumption that the average measurement uncertainty in each grid is the same regardless of the grid; however, this is not true because velocity measurements in a grid further from the Sun tend to have larger uncertainties than those in a closer grid due to its relative faintness, and hence a closer grid should have a larger weight considering this effect. Nevertheless, the relative weights among different grids are, qualitatively, correctly set by the current form of w_{i_R, i_z} because a closer grid tends to have a larger $N_{i_R, i_z}^{\text{obs}}$ value, which makes its relative weight larger. Therefore, although there should be an underestimation of relative weight for a grid closer to the Sun, our result is not expected to change significantly with the missed effect.

Another concern with the w_{i_R, i_z} expression by Eq. (21) is its dependency on $N_{i_R, i_z}^{\text{simu}}$. To reduce the dependency on the simulated number of stars but not increase the computation time significantly, we adopt $N_{i_R, i_z}^{\text{simu}} = \min(10^4, 4 N_{i_R, i_z}^{\text{obs}})$ for each grid. The maximum simulation number of 10^4 indicates that the $N_{i_R, i_z}^{\text{simu}}$ term becomes dominant in w_{i_R, i_z} when $N_{i_R, i_z}^{\text{obs}} > 10^4$. We set this maximum primarily to reduce the computation time, but also to avoid placing too much weight for grids with large $N_{i_R, i_z}^{\text{obs}}$ values, because we want to have a model that matches a wide range of grid points instead of being optimized to a small fraction of the grid points that is highly weighted.

A particular set of the 10 fit parameters is evaluated by $\tilde{\chi}^2 = \sum_{i_R, i_z} \tilde{\chi}_{i_R, i_z}^2$. The summation for $\tilde{\chi}^2$ only run over 651 grids with $R \leq 8440$ pc out of a total of 1207 grids because our primary science interest is in microlensing events toward the Galactic bulge and because the outer disk has a warp

and/or a flare feature, which is not considered in our model. The cut at 8440 pc is motivated by the starting Galactocentric radius of the warp used in the Besançon model (Robin et al. 2003) of $R = 8400$ pc. We refer to a model fitted with this data selection as an all- z model. Additionally, we consider another option, which is highly optimized for microlensing studies toward the Galactic bulge, where the summation for $\tilde{\chi}^2$ run over 234 grids with $R \leq 8440$ pc and $|z| \leq 900$ pc. With this option, we also ignore the agreement in σ_R , i.e., the $\tilde{\chi}_{iR,iz}^2$ in Eq. (20) just run over $p = \overline{v}_\phi, \sigma_\phi, \sigma_z$ and not over $p = \sigma_R$. This is because σ_R is irrelevant to observables of microlensing events in fields near the Galactic center. We refer to a model from this data selection as a low- z model.

3.3. Grid Search

Because the Monte Carlo simulation to calculate $\tilde{\chi}^2$ is computationally expensive, we conduct a grid search to find a combination of parameters with a better agreement to the data. We conduct a sparse initial grid search of the 10 fit parameters with a large interval between adjacent grids at first, and then repeat it in narrower parameter space with a smaller interval. The initial grid search run over the following ranges; $\sigma_{R,\odot}^{\text{thin}} = 30\text{--}50$ km/s, $\sigma_{z,\odot}^{\text{thin}} = 15\text{--}30$ km/s, $\sigma_{R,\odot}^{\text{thick}} = 40\text{--}70$ km/s, $\sigma_{z,\odot}^{\text{thick}} = 35\text{--}65$ km/s, $\beta_R = 0.1\text{--}0.4$, $\beta_z = 0.2\text{--}0.8$, $R_{\sigma_R}^{\text{thin}} = 8\text{--}30$ kpc, $R_{\sigma_z}^{\text{thin}} = 8\text{--}30$ kpc, $R_{\sigma_R}^{\text{thick}} = 8\text{--}30$ kpc, and $R_{\sigma_z}^{\text{thick}} = 8\text{--}30$ kpc. Once a best-fit combination was found at an edge of the parameter space searched, we expanded the parameter space in the next iteration. This procedure was repeated until no significant $\tilde{\chi}^2$ improvement was found with a smaller interval or an expansion of the parameter space.

We conduct the above search for each of the four options, i.e., all combinations of the two options for the data selection (all- z or low- z) and thin disk scale height (flat or linear), respectively. Table 2 shows the best-fit parameters given by the calculations. Figs. 1 and 2 show color maps of each model values and residuals (model value – data value), respectively. In each panel of these figures, we indicate the selected grid region with magenta dashed boxes. Fig. 2 shows that our models fail to reproduce the outer disk distributions, in particular, the \overline{v}_ϕ , but this is expected because our density model is designed for the inner disk and does not consider the warp or flare structure seen in the outer disk. Similarly, the σ_z distribution of the low- z model significantly overestimates the values in $z > 900$ pc which is outside the magenta box. This is because the best-fit $\sigma_{z,\odot}^{\text{thick}}$ value for a low- z model (61.4 or 59.0 km/s) is much higher than that for an all- z model (49.2 or 47.8 km/s), as shown in Table 2. However, this difference has little effect in the microlensing region toward the Galactic bulge because the thick disk stars are relatively rare in this region. Focusing on the region related to the microlensing study (i.e., inside the magenta box of a low- z model), all the four models show moderate agreements with the Gaia data.

The $\tilde{\chi}^2$ value is smallest for the low- z + linear z_d^{thin} model; however, comparison of the $\tilde{\chi}^2$ values between low- z and all- z models is unreasonable because the grids contributing to the $\tilde{\chi}^2$ are different. The $\tilde{\chi}^2$ values, defined by Eq (20), is the weighted root mean square of deviation of the model from the data, that is, $\sqrt{\tilde{\chi}^2}$ provides a weighted average of the deviations in km/s. Notably, the linear scale height models are preferred for both the all- z and low- z models. Although this might indicate that the scale height is not constant inside the solar radius, the flat scale height models are favored in the fits to the data toward bulge regions as described in Section 4.3.2.

We keep all the four models as options for the disk model, and use each of them combined with a bulge model in the fits conducted in Section 4, and the four models are compared in Section 4.3.2

Table 2. Best-fit parameters for the disk kinematic model.

Model	N_{grid}	$\sigma_{R,\odot}^{\text{thin}}$	$\sigma_{z,\odot}^{\text{thin}}$	$\sigma_{R,\odot}^{\text{thick}}$	$\sigma_{z,\odot}^{\text{thick}}$	β_R	β_z	$R_{\sigma_R}^{\text{thin}}$	$R_{\sigma_z}^{\text{thin}}$	$R_{\sigma_R}^{\text{thick}}$	$R_{\sigma_z}^{\text{thick}}$	$\bar{\chi}_{v_\phi}^2$	$\bar{\chi}_{\sigma_R}^2$	$\bar{\chi}_{\sigma_\phi}^2$	$\bar{\chi}_{\sigma_z}^2$
		[km/s]	[km/s]	[km/s]	[km/s]			[kpc]	[kpc]	[kpc]	[kpc]				
all- z + flat z_d^{thin}	651	42.0	24.4	75	49.2	0.32	0.77	14.3	5.9	180	9.4	19.5	16.3	15.9	9.6
all- z + linear z_d^{thin}	651	44.0	25.4	68	47.8	0.34	0.81	21.4	8.1	57.6	15.6	14.9	13.7	14.1	6.7
low- z + flat z_d^{thin}	234	35.2	22.2	75	61.4	0.22	0.77	9.5	10.4	90.0	6.9	12.6	7.2	–	4.2
low- z + linear z_d^{thin}	234	37.6	23.4	68	59.0	0.30	0.82	11.1	7.8	47.0	52.0	8.7	5.8	–	3.5

with respect to the best-fit χ^2 values to the bulge data. We discuss the determined values in Table 2 by comparing with the previous studies in Section 5.1.

4. FITTING FOR THE BULGE AND IMF PARAMETERS

In this section, we determine the 4 fit parameters for the IMF model, 7–15 fit parameters for the ρ_B model, and 19 fit parameters for the v_B model, through the Markov Chain Monte Carlo (MCMC) fitting to the observed distributions toward the bulge sky of the OGLE-III RC star count (Nataf et al. 2013), VIRAC proper motion (Smith et al. 2018; Clarke et al. 2019), BRAVA radial velocity (Rich et al. 2007; Kunder et al. 2012), and star and microlensing event count by OGLE-IV (Mróz et al. 2017, 2019).

We use the bulge model combined with the disk model in the fit, where we fix and use the 10 fit parameters for the v_d model determined in Section 3. However, the local density values are recalculated in the fit for every given set of the 4 fit parameters in the IMF.

4.1. Data and Corresponding χ^2 Values

This section describes details of each dataset used to constrain the 30–38 fit parameters. For each dataset, we also describe model values compared with the observed values and introduce the corresponding χ^2 values. All the used data are plotted in Figs. 4, 6, and 8.

4.1.1. OGLE-III red clump star count

Nataf et al. (2013) divided the OGLE-III Galactic bulge fields over 90.25 deg^2 in $-10^\circ < l < 10^\circ$ and $2^\circ < |b| < 7^\circ$ into 9019 areas and measured the red clump (RC) star count in each area. They used a luminosity function model that primarily consists of a Gaussian RC component on an exponential red giant branch continuum for fit to the observed I -mag distribution in each area. As a result of the fits, they provided a catalog of 9019 sets of the number count N_{RC} , mean distance modulus DM_{RC} , variance of distance modulus σ_{DM}^2 , and error matrix for them, as well as the extinctions A_I and A_V , where N_{RC} and DM_{RC} are equivalent to the area and the peak of the Gaussian, respectively. The variance of distance modulus, σ_{DM}^2 , was determined by subtracting the sum of variances of the extinction in the area ($= \sigma_{A_I}^2$) and of the intrinsic brightness of RC ($= \sigma_{I,\text{RC},0}^2$) from the variance of the Gaussian ($= \sigma_{I,\text{RC}}^2$).

Nataf et al. (2013) used $\sigma_{I,\text{RC},0} = 0.09$ with no uncertainty to derive the σ_{DM}^2 values. To be conservative, we apply $\sigma_{I,\text{RC},0} = 0.15 \pm 0.06$, i.e., we modify the data by $\sigma_{\text{DM}}^2 = \sigma_{\text{DM,org}}^2 + 0.09^2 - 0.15^2$ and increase the uncertainty accordingly. This choice for $\sigma_{I,\text{RC},0}$ is motivated by Hawkins et al. (2017) who measured the RC mag dispersions of 0.20 ± 0.02 in both G - and J -bands. Because the

wavelength of I -band is between these bands, we conservatively take 0.15 ± 0.06 so that its $1\text{-}\sigma$ range includes both 0.09 used by [Nataf et al. \(2013\)](#) and 0.20 measured for G - and J -bands.

Moreover, because the measurements of N_{RC} , DM_{RC} , and σ_{DM}^2 are all from the Gaussian fit, it could overestimate/underestimate the RC population when it is not distributed following a Gaussian shape. In particular, because our disk model has a constant surface density at $R < 5.3$ kpc (see Eqs. 5–6), which is continuously distributed in the bulge region mildly, most or part of the disk RC population is expected to be absorbed into the exponential red giant branch continuum component in the fit by [Nataf et al. \(2013\)](#), although the fraction of absorption probably depends on the line of sight. To account for this uncertainty, we considered only the bulge population in the model observables given below in Eqs. (22)–(24), in addition to increasing the uncertainties of N_{RC} by 10% and adding 0.04 mag error to the uncertainties of DM_{RC} in quadrature.

[Cao et al. \(2013\)](#) modeled a bulge density distribution by fitting to the [Nataf et al. \(2013\)](#) data, and we similarly follow their parameterization but with a modification on the integration range. For a particular i th line of sight toward (l_i, b_i) , the model RC number count is expressed as

$$N_{\text{RC},i}^{\text{mod}} = \Omega_i N_{\text{B},i} \times \frac{\sum_j N_{\text{RC},j}^{\text{obs}}}{\sum_j \Omega_j N_{\text{B},j}}, \quad (22)$$

where Ω_i is the sky area of the i th field, and $N_{\text{B},i}$ is the model number of bulge stars integrated along i th line of sight, which is defined as

$$N_{\text{B},i} \equiv \int_{s_{\text{min},i}}^{s_{\text{max},i}} n_{\text{B}}(l_i, b_i, s) s^2 ds,$$

and $n_{\text{B}}(l_i, b_i, s)$ is the number density of bulge stars at the distance s from the Sun toward (l_i, b_i) . The summation for j in the second factor in Eq. (22) runs over all the 9019 lines of sight, and the factor is for a normalization to let the total $N_{\text{RC},i}^{\text{mod}}$ be same as the observed one, i.e., to make $\sum_i N_{\text{RC},i}^{\text{mod}} = \sum_i N_{\text{RC},i}^{\text{obs}}$.

The mean and variance of distance modulus are expressed as

$$\text{DM}_{\text{RC},i}^{\text{mod}} = \frac{1}{N_{\text{B},i}} \int_{s_{\text{min},i}}^{s_{\text{max},i}} n_{\text{B}}(l_i, b_i, s) s^2 \text{DM}(s) ds \quad (23)$$

and

$$(\sigma_{\text{DM},i}^2)^{\text{mod}} = \frac{1}{N_{\text{B},i}} \int_{s_{\text{min},i}}^{s_{\text{max},i}} n_{\text{B}}(l_i, b_i, s) s^2 [\text{DM}(s)]^2 ds - (\text{DM}_{\text{RC},i}^{\text{mod}})^2, \quad (24)$$

respectively, where $\text{DM}(s)$ denotes the distance modulus at distance s , which is given by $\text{DM}(s) = 5 \log_{10}[s/(10\text{pc})]$.

For the integration range, we use a pair of $s_{\text{min},i}$ and $s_{\text{max},i}$ that satisfies

$$\text{DM}(s_{\text{min},i}) = \text{DM}_{\text{RC},i}^{\text{obs}} - \min(3\sigma_{I,\text{RC},i}^{\text{obs}}, 1.5) \quad (25)$$

$$\text{DM}(s_{\text{max},i}) = \text{DM}_{\text{RC},i}^{\text{obs}} + \min(3\sigma_{I,\text{RC},i}^{\text{obs}}, 1.5), \quad (26)$$

where $\sigma_{I,\text{RC},i}^{\text{obs}}$ is the standard deviation of the Gaussian fit for the RC component in the I -band luminosity function of i th field. We chose these values rather than $s_{\text{min},i} = 3$ kpc and $s_{\text{max},i} = 13$ kpc

used by Cao et al. (2013) because the RC stars outside of $\pm 3\sigma$ from the mean have a negligible contribution to the measurements of the three observables, which are equivalent to the area, peak position, and variance of the Gaussian distribution. The value of 1.5 for the maximum range of integration originates from the limit on the fitting range of magnitude, $-1.5 < I - I_{\text{RC}} < 1.5$, set by Nataf et al. (2013).

Following Cao et al. (2013), we calculate the χ^2 for this dataset by

$$\chi_{\text{RC}}^2 = \sum_i (\mathbf{X}_i^{\text{mod}} - \mathbf{X}_i^{\text{obs}})^T \mathbf{S}_i^{-1} (\mathbf{X}_i^{\text{mod}} - \mathbf{X}_i^{\text{obs}}), \quad (27)$$

where $\mathbf{X}_i = (N_{\text{RC},i}, \text{DM}_{\text{RC},i}, \sigma_{\text{DM},i}^2)$ and \mathbf{S}_i^{-1} is the covariance matrix of the uncertainties. We further define the following four χ^2 values to quantify a contribution to χ_{RC}^2 from each observable;

$$\chi_p^2 = \sum_i \left(\frac{p_i^{\text{mod}} - p_i^{\text{obs}}}{p_i^{\text{err}}} \right)^2 \quad (p = N_{\text{RC}}, \text{DM}_{\text{RC}}, \sigma_{\text{DM}}^2),$$

and $\chi_{\text{cov}}^2 = \chi_{\text{RC}}^2 - \chi_{N_{\text{RC}}}^2 - \chi_{\text{DM}_{\text{RC}}}^2 - \chi_{\sigma_{\text{DM}}^2}^2$, where p_i^{err} denotes the error-bar of the i th data of parameter p .

4.1.2. VIRAC red giants' proper motions

Smith et al. (2018) provided the VVV infrared astrometric catalogue (VIRAC), which is a near-infrared proper motion catalog of the five years VISTA Variables in the Via Lactea (VVV) survey (Minniti et al. 2010), which includes 312,587,642 sources over 560 deg^2 of the bulge and southern disk. Clarke et al. (2019) calibrated the VIRAC proper motions by comparing the VIRAC values to the corresponding Gaia values. They carefully selected red giants with $11.8 < K_{s,0} < 13.6$ from the calibrated catalog, where $K_{s,0}$ indicates the extinction-corrected K_s magnitude. Then they split each of the VVV tiles located in the bulge region into 4 sub-tiles and presented means $\langle \mu_l \rangle$ and dispersions σ_{μ_i} ($i = l, b$) of proper motions of the selected giant stars in each sub-tile. We use the data for $\langle \mu_l \rangle$, σ_{μ_l} , and σ_{μ_b} in 676 sub-tiles distributed roughly over $-9^\circ < l < 9.4^\circ$ and $-9.4^\circ < b < 4.2^\circ$. Out of the 676 sub-tiles, we do not use 90 sub-tiles with $|b| \lesssim 1^\circ$ because of high extinction values. Thus, we use the data in 586 sub-tiles for the fit. We do not use the $\langle \mu_b \rangle$ data because they are little sensitive to the fit parameters and not very useful to constrain them.

Seeing-limited observations toward the Galactic bulge often suffer from systematic errors due to blended stars. Because the data are derived from bright stars with $11.8 < K_{s,0} < 13.6$, they are not expected to be affected by such systematics compared to fainter stars. To verify this, we compared the proper motion dispersion measurements from VIRAC with those from the *Hubble Space Telescope* (*HST*) observations. Fig. 3 shows the comparison as a function of extinction A_I . We used 35 fields observed by Kozłowski et al. (2006) and 4 fields summarized in Table 2 of Terry et al. (2020) for the comparison, and the *HST* values are taken from the two papers. The 4 *HST* values from Terry et al. (2020) were originally measured by Calamida et al. (2014), Kuijken & Rich (2002), and Terry et al. (2020). If there are no systematic errors, the mean value of $\sigma_{\mu_i, \text{VVV}} - \sigma_{\mu_i, \text{HST}}$ should be consistent with 0. However, we found the mean and standard deviation values of $\langle \sigma_{\mu_l, \text{VVV}} - \sigma_{\mu_l, \text{HST}} \rangle = 0.124 \pm 0.135 \text{ mas/yr}$ and $\langle \sigma_{\mu_b, \text{VVV}} - \sigma_{\mu_b, \text{HST}} \rangle = 0.153 \pm 0.144 \text{ mas/yr}$ when we used the 39 fields without the outlier indicated in the figure that is specified by Terry et al. (2020). This implies the existence of systematic offset between the VVV and *HST* measurements. We, at first, checked

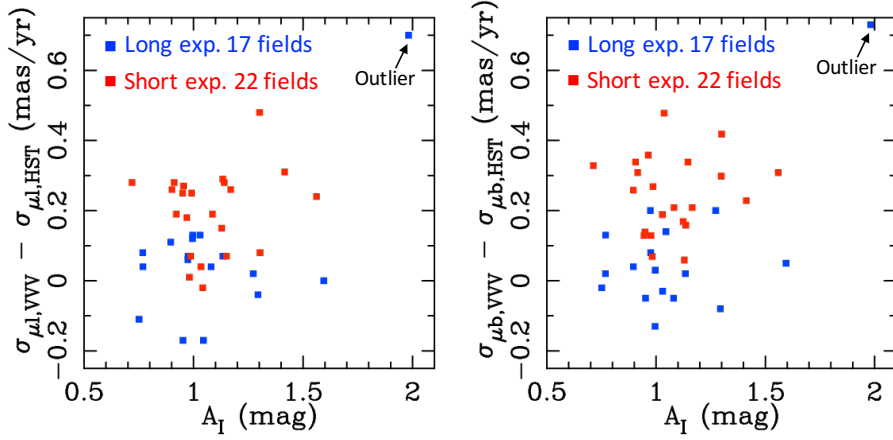


Figure 3. Comparison of proper motion dispersions (left σ_{μ_l} , right σ_{μ_b}) between VVV and *HST*. Differences of measured values are plotted as a function of extinction for 35 fields from Kozłowski et al. (2006) and 4 fields from Table 2 of Terry et al. (2020). 22 fields with ≤ 40 secs exposures from Kozłowski et al. (2006) are classified as the short exp. fields while the other 17 fields are classified as the long exp. fields. An outlier pointed by Terry et al. (2020) is indicated.

whether there was any correlation between the offset and the extinction, but Fig. 3 shows no such a correlation except for the outlier.

Thereafter, we divide the sample of 39 fields into two subsamples depending on the exposure time of the *HST* observations because certain fields have significantly shorter exposure times than others. One of the two subsamples consists of 22 short exposure fields from Kozłowski et al. (2006) with each exposure less than 40 s, and the other consists of 17 long exposure fields with each exposure longer than 100 s. Note that Kozłowski et al. (2006) used 1st epoch data taken by the WFPC2/PC camera, which is much less sensitive than the ACS camera used to take their 2nd epoch data. The mean and standard deviation values are $\langle \sigma_{\mu_l, \text{VVV}} - \sigma_{\mu_l, \text{HST}} \rangle = 0.205 \pm 0.116$ mas/yr and $\langle \sigma_{\mu_b, \text{VVV}} - \sigma_{\mu_b, \text{HST}} \rangle = 0.246 \pm 0.108$ mas/yr for the 22 short exposure fields and $\langle \sigma_{\mu_l, \text{VVV}} - \sigma_{\mu_l, \text{HST}} \rangle = 0.023 \pm 0.096$ mas/yr and $\langle \sigma_{\mu_b, \text{VVV}} - \sigma_{\mu_b, \text{HST}} \rangle = 0.034 \pm 0.093$ mas/yr for the 17 long exposure fields without the outlier. The long exposure subsample shows no clear difference between VVV and *HST* measurements while the short exposure subsample does.

Thus, we conclude that the implied offset is due to the systematic error in the *HST* measurements for the 22 short exposure fields. Given the standard deviation of ~ 0.1 mas/yr for the long exposure subsample, we use 0.1 mas/yr for the uncertainty of σ_{μ_l} and σ_{μ_b} of each sub-tile because formal statistic errors are comparatively small. For the uncertainty of $\langle \mu_l \rangle$, we use 0.14 mas/yr by additionally considering the error of calibration to the Gaia scale of ~ 0.1 mas/yr (Clarke et al. 2019).

For a particular i th subtile's coordinate of (l_i, b_i) , the model $\langle \mu_l \rangle$ value is calculated by

$$\langle \mu_l \rangle_i^{\text{mod}} = \frac{\int_{3\text{kpc}}^{16\text{kpc}} [n_{\text{d}}^{\text{RG}}(l_i, b_i, s) \langle \mu_{l, \text{d}}(l_i, b_i, s) \rangle + n_{\text{B}}^{\text{RG}}(l_i, b_i, s) \langle \mu_{l, \text{B}}(l_i, b_i, s) \rangle] w(s) ds}{\int_{3\text{kpc}}^{16\text{kpc}} [n_{\text{d}}^{\text{RG}}(l_i, b_i, s) + n_{\text{B}}^{\text{RG}}(l_i, b_i, s)] w(s) ds}, \quad (28)$$

where $n_{\text{d}}^{\text{RG}}(l_i, b_i, s)$ and $n_{\text{B}}^{\text{RG}}(l_i, b_i, s)$ are the number densities of red giants of the disk and bulge components at (l_i, b_i, s) , respectively. We used the same definition for red giants in Section 2.2.1, i.e., stars with $\mathcal{M}_G < 3.9$ mag and $(G_{\text{BP}} - G_{\text{RP}})_0 > 0.95$. $\langle \mu_{l, \text{d}}(l_i, b_i, s) \rangle$ and $\langle \mu_{l, \text{B}}(l_i, b_i, s) \rangle$ are mean proper

motions calculated using our disk and bulge velocity model at (l_i, b_i, s) , respectively. Calculations of proper motion require the solar velocity, and again we use $(v_{\odot,x}, v_{\odot,y}, v_{\odot,z}) = (-10, 243, 7)$ km/s in this study. The weight $w(s)$ is given by

$$w(s) = s^2 \int_{11.8}^{13.6} L_{\mathcal{M}_{K_s}} (K_{s,0} - \text{DM}(s)) dK_{s,0}, \quad (29)$$

where $L_{\mathcal{M}_{K_s}}(\mathcal{M}_{K_s})$ is luminosity function for the red giant's absolute magnitude \mathcal{M}_{K_s} , given by Eqs. (2)–(5) of [Clarke et al. \(2019\)](#). Further, the model σ_{μ_j} ($j = l, b$) values are expressed as

$$\sigma_{\mu_j,i}^{\text{mod}} = \sqrt{\langle \mu_j^2 \rangle_i^{\text{mod}} - \left(\langle \mu_j \rangle_i^{\text{mod}} \right)^2}, \quad (30)$$

where

$$\langle \mu_j^2 \rangle_i^{\text{mod}} = \frac{\int_{3\text{kpc}}^{16\text{kpc}} [n_{\text{d}}^{\text{RG}}(l_i, b_i, s) \langle \mu_{j,\text{d}}^2(l_i, b_i, s) \rangle + n_{\text{B}}^{\text{RG}}(l_i, b_i, s) \langle \mu_{j,\text{B}}^2(l_i, b_i, s) \rangle] w(s) ds}{\int_{3\text{kpc}}^{16\text{kpc}} [n_{\text{d}}^{\text{RG}}(l_i, b_i, s) + n_{\text{B}}^{\text{RG}}(l_i, b_i, s)] w(s) ds}.$$

χ^2 for this dataset is denoted by

$$\chi_{\mu}^2 = \chi_{\mu_l}^2 + \chi_{\sigma_{\mu_l}}^2 + \chi_{\sigma_{\mu_b}}^2,$$

where

$$\chi_p^2 = \sum_i \left(\frac{p_i^{\text{mod}} - p_i^{\text{obs}}}{p_i^{\text{err}}} \right)^2 \quad (p = \mu_l, \sigma_{\mu_l}, \sigma_{\mu_b}).$$

4.1.3. BRAVA radial velocity data

The Bulge Radial Velocity Assay (BRAVA, [Rich et al. 2007](#); [Kunder et al. 2012](#)) is a large spectroscopic survey of M giant stars in the Galactic bulge to constrain the bulge dynamics by measuring their radial velocities (RVs). We use the mean and dispersion values of the RV measurements in 82 fields where 80 fields are located at $-10^\circ \leq l \leq 10^\circ$ and $3^\circ \leq |b| \leq 8^\circ$, while the other 2 are located at $(l, b) = (0^\circ, -1^\circ)$ and $(l, b) = (0^\circ, -2^\circ)$. Although RV is not very relevant to our interest in microlensing observables, we use these data as a constraint because RV provides direct information of velocity compared to proper motion, which is a combination of distance and velocity.

The BRAVA mean RV values are given in the Galactocentric frame by a conversion from the originally observed values in the heliocentric frame. The conversion was done using the Sun velocity of $(-9.0, 231.9, 7.0)$ km/s along (x, y, z) axes ([Howard et al. 2008](#)), which is slightly different from our values of $(-10, 243, 7)$ km/s. Thus, we reconverted the mean RV values using our values and then use them as data for our fits.

Similar to $\langle \mu_l \rangle_i^{\text{mod}}$, the model value for mean RV is given by

$$\langle \text{RV} \rangle_i^{\text{mod}} = \frac{\int_{3\text{kpc}}^{16\text{kpc}} [n_{\text{d}}^{\text{RG}}(l_i, b_i, s) \langle \text{RV}_{\text{d}}(l_i, b_i, s) \rangle + n_{\text{B}}^{\text{RG}}(l_i, b_i, s) \langle \text{RV}_{\text{B}}(l_i, b_i, s) \rangle] s^{0.6} ds}{\int_{3\text{kpc}}^{16\text{kpc}} [n_{\text{d}}^{\text{RG}}(l_i, b_i, s) + n_{\text{B}}^{\text{RG}}(l_i, b_i, s)] s^{0.6} ds}, \quad (31)$$

where the weight $s^{0.6}$ follows [Portail et al. \(2015\)](#) who combined the volume effect ($\propto s^2$) with an approximate luminosity function of giant stars of $\propto 10^{0.28\mathcal{M}_K}$ ([Wegg & Gerhard 2013](#)), which resulted

in a dependency on the distance of $\propto s^{-1.4}$. Further, the model RV dispersion value is calculated using the following

$$\sigma_{\text{RV},i}^{\text{mod}} = \sqrt{\langle \text{RV}^2 \rangle_i^{\text{mod}} - \left(\langle \text{RV} \rangle_i^{\text{mod}} \right)^2}. \quad (32)$$

χ^2 for this dataset is denoted by

$$\chi_{\text{BRA}}^2 = \chi_{\text{RV}}^2 + \chi_{\sigma_{\text{RV}}}^2,$$

where

$$\chi_p^2 = \sum_i \left(\frac{p_i^{\text{mod}} - p_i^{\text{obs}}}{p_i^{\text{err}}} \right)^2 \quad (p = \langle \text{RV} \rangle, \sigma_{\text{RV}}).$$

4.1.4. OGLE-IV star count data

Mróz et al. (2019) analyzed long-term photometric observations of the Galactic bulge by the OGLE group using their fourth-generation wide-field camera OGLE-IV. The analyzed fields consist of 9 high-cadence fields and 112 low-cadence fields, with each field further divided into 32 subfields having an individual area of $\sim 0.044 \text{ deg}^2$. They measured the number of stars with $I < 21$ mag and $I < 18$ mag, denoted by $N_{I < 21}$ and $N_{I < 18}$ respectively, for each subfield in addition to the microlens-related observables described in Section 4.1.5. Note that $N_{I < 21}$ is used as the number of candidate source stars in the microlensing events. Although an extinction value A_I is needed for each line of sight to model $N_{I < I_c}$ ($I_c = 18, 21$), there is no extinction catalog in I -band covering all the OGLE-IV fields. Thus, we only use 1456 subfields covered by the A_I map of Nataf et al. (2013) for our analysis.

The model $N_{I < I_c}$ for a particular i th subfield is calculated from

$$N_{I < I_c, i}^{\text{mod}} = \Omega_i \int_{3\text{kpc}}^{16\text{kpc}} n_{I < I_c}(l_i, b_i, s) s^2 ds \quad (I_c = 18, 21), \quad (33)$$

where Ω_i is the sky area, and $n_{I < I_c}(l_i, b_i, s)$ is the number density of stars with $I < I_c$ at a distance s from the Sun toward (l_i, b_i) , which is expressed as

$$n_{I < I_c}(l_i, b_i, s) = [n_{\text{d}}(l_i, b_i, s) + n_{\text{B}}(l_i, b_i, s)] \int_{I < I_c} L_{\mathcal{M}_I}(I - \text{DM}(s) - A_I(l_i, b_i, s)) dI \quad (34)$$

with the stellar number density for disk and bulge stars, $n_{\text{d}}(l_i, b_i, s)$ and $n_{\text{B}}(l_i, b_i, s)$, respectively, and the luminosity function for I -band absolute magnitude $L_{\mathcal{M}_I}(\mathcal{M}_I)$ calculated using the PARSEC isochrone models (Bressan et al. 2012; Chen et al. 2014; Tang et al. 2014) for a given IMF. We use a 3D extinction distribution of

$$A_I(l_i, b_i, s) = A_{I, \text{RC}}(l_i, b_i) \frac{1 - \exp[-s/(h_{\text{dust}}/\sin |b_i|)]}{1 - \exp[-s_{\text{RC}}(l_i, b_i)/(h_{\text{dust}}/\sin |b_i|)]}, \quad (35)$$

where $A_{I, \text{RC}}(l_i, b_i)$ and $s_{\text{RC}}(l_i, b_i)$ are the mean extinction for the RC and mean distance to RC, respectively, both taken from the Nataf et al. (2013) extinction catalog, and we use $h_{\text{dust}} = 164 \text{ pc}$ based on the measurement by Nataf et al. (2013). Because the extinction distribution is not uniform even inside a subfield of $\sim 0.044 \text{ deg}^2$, we further divide each subfield into 8 sub-subfields and then

calculate the $N_{I < I_c, i}^{\text{mod}}$ value for each subfield by summing the values over the 8 sub-subfields with different $A_{I, \text{RC}}$ values.

χ^2 for the star count data is given by

$$\chi_{N_{I < I_c}}^2 = \sum_i \left(\frac{N_{I < I_c, i}^{\text{mod}} - N_{I < I_c, i}^{\text{obs}}}{N_{I < I_c, i}^{\text{err}}} \right)^2 \quad (I_c = 18, 21),$$

where we apply $N_{I < 21, i}^{\text{err}} = 0.12 N_{I < 21, i}^{\text{obs}}$ because Mróz et al. (2019) estimated the errors as 10 to 15 % by comparing to star count in *HST* images. We use a larger uncertainty of $N_{I < 18, i}^{\text{err}} = 0.14 N_{I < 18, i}^{\text{obs}}$ because evolved stars like red giants mainly contribute to $N_{I < 18}$ and the isochrone model uncertainty for such evolved stars is likely larger than that for main-sequence stars contributing to $N_{I < 21}$.

The model value $N_{I < I_c}^{\text{mod}}$ depends on the density model, as well as the IMF, because the luminosity function $L_{\mathcal{M}_I}(\mathcal{M}_I)$ depends on the IMF. As a quantity that is less dependent on the density model but more on the IMF, we defined $f_{18/21} \equiv N_{I < 18} / N_{I < 21}$. χ^2 for this quantity is calculated by

$$\chi_{f_{18/21}}^2 = \sum_i \left(\frac{f_{18/21, i}^{\text{mod}} - f_{18/21, i}^{\text{obs}}}{f_{18/21, i}^{\text{err}}} \right)^2,$$

where we used $f_{18/21, i}^{\text{err}} = 0.16 f_{18/21, i}^{\text{obs}}$. This uncertainty is taken slightly smaller than just a square root of the sum of the $N_{I < 21, i}^{\text{err}}$ and $N_{I < 18, i}^{\text{err}}$ considering a positive correlation between $N_{I < 21, i}^{\text{obs}}$ and $N_{I < 18, i}^{\text{obs}}$.

4.1.5. Number of microlensing events and t_E distribution by OGLE-IV

Mróz et al. (2019) also provided the microlensing optical depth and the event rate for each OGLE-IV field. However, it is statistically easier to deal with another equivalent quantity, $N_{\text{eve}, i}(t_E)$, which is the number of detected events as a function of t_E for each i th subfield, because $N_{\text{eve}, i}(t_E)$ simply follows a Poisson distribution. For a particular i th subfield and a j th t_E bin, the expected number of event detections is given by

$$N_{\text{eve}, i}^{\text{mod}}(t_{E, j}) = \frac{2N_{I < 21, i}^{\text{mod}} T_0}{\pi \langle t_E \rangle_i} \tau_{I < 21, i} f_i(t_{E, j}) \epsilon_i(t_{E, j}) \Delta t_E, \quad (36)$$

where T_0 is the survey duration that takes 2741 or 2011 days depending on the field, $\tau_{I < 21, i}$ is the average optical depth over the monitored $N_{I < 21, i}^{\text{mod}}$ stars, which is given by

$$\tau_{I < 21, i} = \frac{1}{N_{I < 21, i}^{\text{mod}}} \int_{3\text{kpc}}^{16\text{kpc}} \tau(l_i, b_i, s) n_{I < 21}(l_i, b_i, s) s^2 ds \quad (37)$$

with

$$\tau(l_i, b_i, s) = \frac{4\pi G}{c^2} \int_0^s \rho(l_i, b_i, s_L) \frac{s_L(s - s_L)}{s} ds_L, \quad (38)$$

$f_i(t_E)$ is the probability density function of t_E , $\langle t_E \rangle_i$ is the mean t_E value given by $\langle t_E \rangle_i = \int f_i(t_E) t_E dt_E$, $\epsilon_i(t_E)$ is the detection efficiency for an event with t_E in the subfield, and Δt_E is the t_E bin size. We have been provided with the detection efficiency values in addition to the number

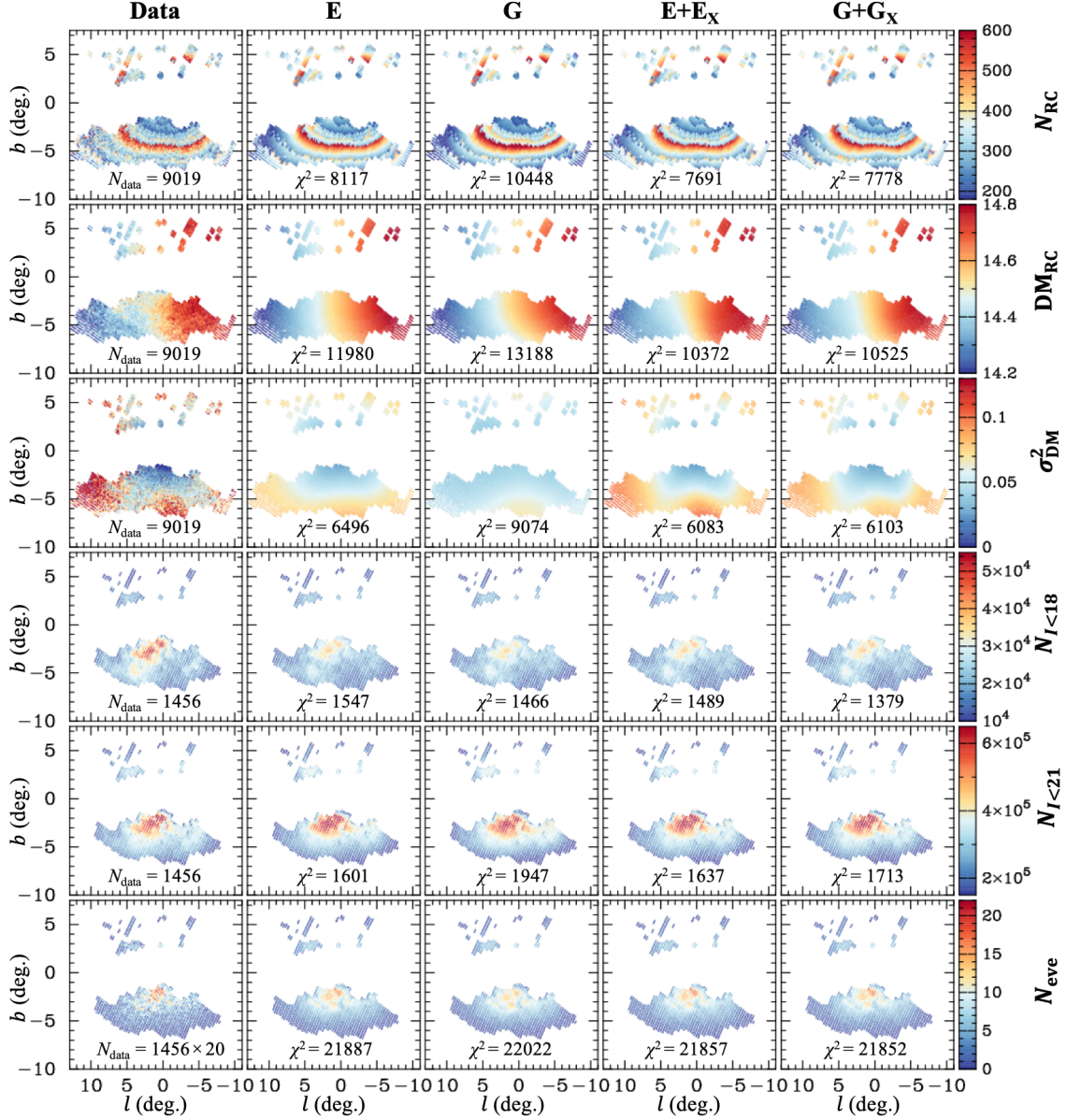


Figure 4. Far left: Data distribution of six quantities used to constrain the bulge density (ρ_B) model (Nataf et al. 2013; Mróz et al. 2019). The right six rows: The same distributions from each indicated model. χ^2 values defined for each quantity are shown. In the bottom panels indicated by N_{eve} , total number of (expected) event detections in i th subfield, $\sum_{j=1}^{20} N_{eve,i}(t_{E,j})$, are plotted.

of detected events as a function of t_E for each subfield through a private communication with P. Mróz.

We determine χ^2 for the number of microlensing event detections with

$$\chi_{N_{eve}}^2 = \sum_{i,j} -2 \ln P[N_{eve,i}^{obs}(t_{E,j}); N_{eve,i}^{mod}(t_{E,j})], \quad (39)$$

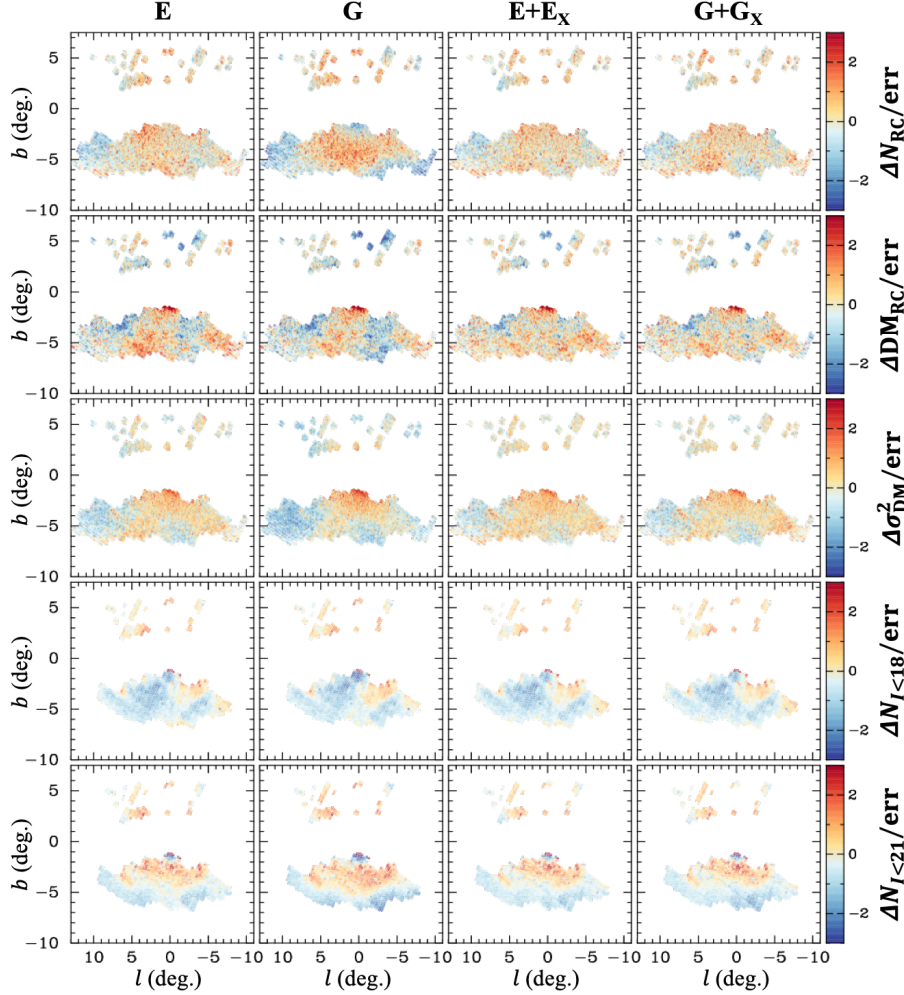


Figure 5. Residuals corresponding to Fig. 4. In i th subfield, $(p_i^{\text{mod}} - p_i^{\text{obs}})/p_i^{\text{err}}$, is plotted where p is each indicated parameter on the far right.

where $P(x; \lambda) = \lambda^x e^{-\lambda}/x!$ is the Poisson probability of x with the mean value λ . A j th t_E bin includes events with $0.125(j-1) \leq \log[t_E/\text{days}] < 0.125j$ ($j = 1, \dots, 20$) for $i \in O_{\text{low}}$, while it includes events with $-0.30 + 0.14(j-1) \leq \log[t_E/\text{days}] < -0.30 + 0.14j$ ($j = 1, \dots, 20$) for $i \in O_{\text{hi}}$, where $i \in O_{\text{low}}$ and $i \in O_{\text{hi}}$ indicate when i th subfield is located in the low- and high-cadence fields, respectively. Note that 4,057 bins have $N_{\text{eve},i}^{\text{obs}}(t_{E,j}) > 0$ out of the total 29,120 bins ($1456 \text{ subfields} \times 20 \text{ bins}$) while the remaining have $N_{\text{eve},i}^{\text{obs}}(t_{E,j}) = 0$.

The probability density function of t_E , $f_i(t_E)$, is calculated through a Monte Carlo simulation of $\sim 10^8$ microlensing events for each i th subfield with a given model. This is computationally expensive and time-consuming when $f_i(t_E)$ is updated for every proposed model in the MCMC fitting procedure described in Section 4.3. Thus, in a fitting run, we instead use a representative $f_i(t_E)$ calculated with a tentative best-fit model because we found that the $\chi_{N_{\text{eve}}}^2$ value had negligible variance when the $f_i(t_E)$ used was calculated with a model showing similar $\chi_{t_E}^2$ introduced below.

Mróz et al. (2017) and Mróz et al. (2019) separately provided t_E distributions consisting of 2212 events in the high-cadence fields and 5788 events in the low-cadence fields, respectively, which are

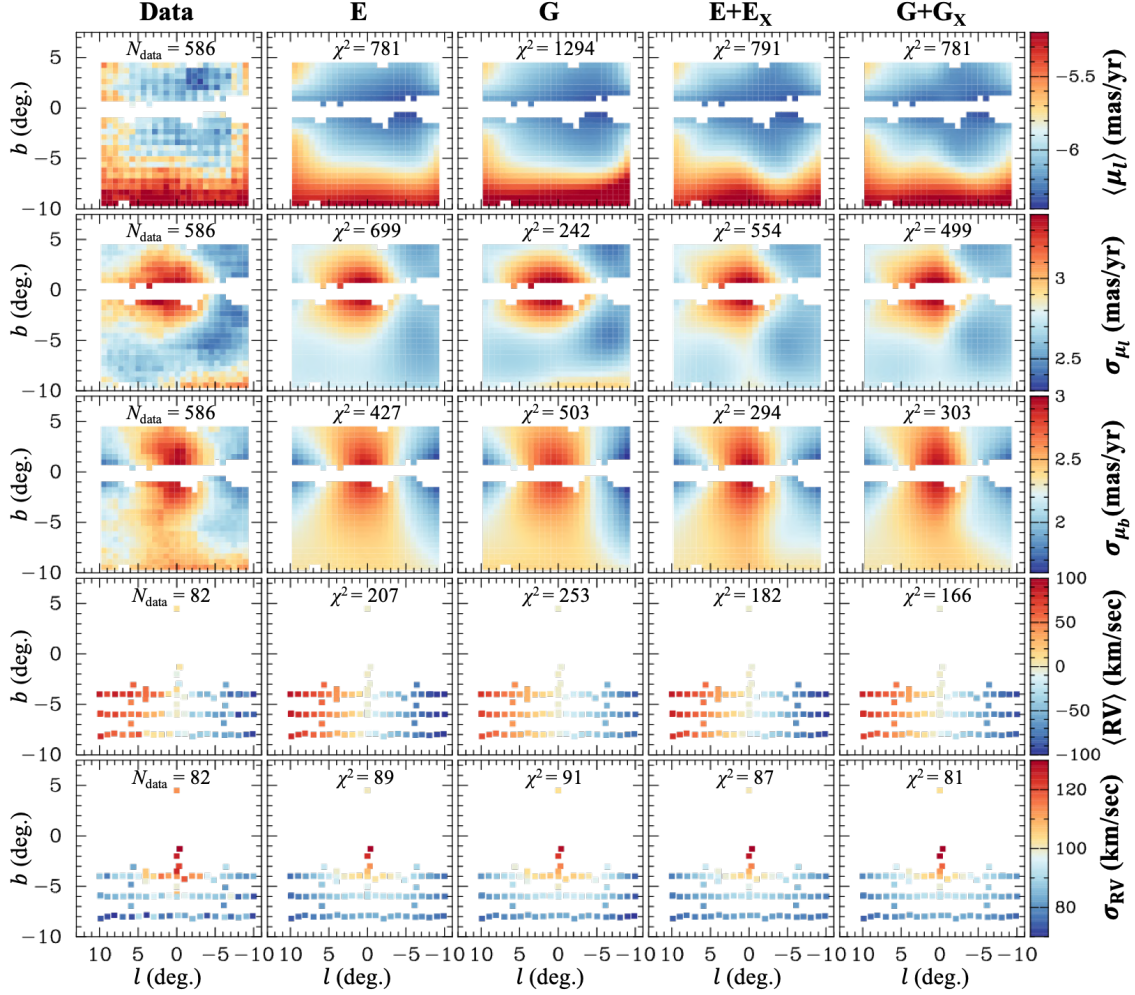


Figure 6. Far left: Data distribution of five quantities used to constrain the bulge velocity (v_B) model (Clarke et al. 2019; Rich et al. 2007; Kunder et al. 2012). The right six rows: The same distributions from each indicated model. χ^2 values defined for each quantity are shown.

denoted by $N_{\text{O}_{\text{hi}}}^{\text{obs}}(t_{E,j})$ and $N_{\text{O}_{\text{low}}}^{\text{obs}}(t_{E,j})$, respectively. These are given by

$$N_o^{\text{obs}}(t_{E,j}) = \sum_{i \in o} N_{\text{eve},i}^{\text{obs}}(t_{E,j}) \quad (o = \text{O}_{\text{hi}}, \text{O}_{\text{low}}),$$

where the summation is taken over all subfields located in $i \in o$ ($o = \text{O}_{\text{hi}}$ or O_{low}). The range of summation is different from the case for $\chi_{N_{\text{eve}}}^2$ where only the subfields covered by Nataf et al. (2013) are considered because a shape of t_E distribution is not sensitive to variation in extinction values. A compared model value for a particular j th t_E bin is

$$N_o^{\text{mod}}(t_{E,j}) = \eta_o \langle \epsilon_o \rangle_j \sum_{i \in o} \omega_i f_i(t_{E,j}) \Delta t_E \quad (o = \text{O}_{\text{hi}}, \text{O}_{\text{low}}), \quad (40)$$

where the mean detection efficiency $\langle \epsilon_o \rangle_j$ and weight for each subfield ω_i are

$$\langle \epsilon_o \rangle_j \equiv \frac{\sum_{i \in o} N_{\text{eve},i}^{\text{obs}}(t_{E,j})}{\sum_{i \in o} N_{\text{eve},i}^{\text{obs}}(t_{E,j}) / \epsilon_i(t_{E,j})},$$

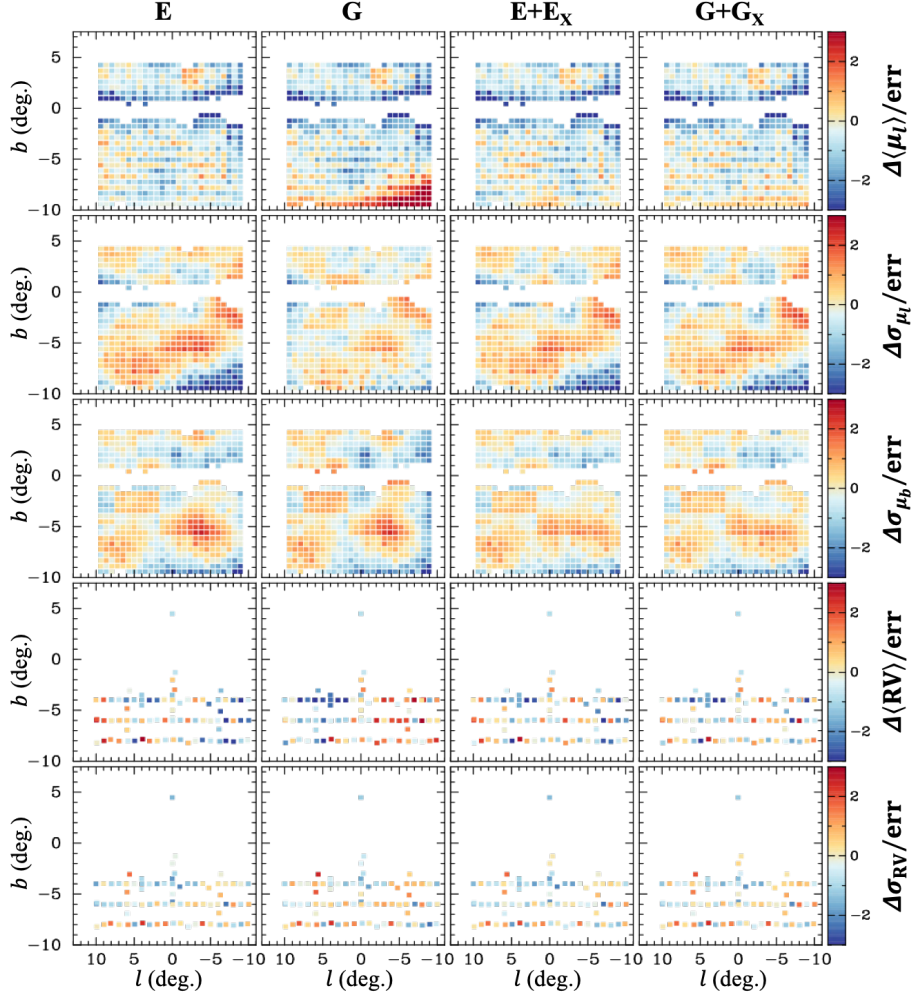


Figure 7. Residuals corresponding to Fig. 6. In i th subfield, $(p_i^{\text{mod}} - p_i^{\text{obs}})/p_i^{\text{err}}$, is plotted where p is each indicated parameter.

and

$$\omega_i = \sum_j \frac{N_{\text{eve},i}^{\text{obs}}(t_{\text{E},j})}{\epsilon_i(t_{\text{E},j})},$$

respectively, with η_o being an arbitrary constant expected to be approximately 1. Although $\eta_o = 1$ provides $\sum_j N_o^{\text{mod}}(t_{\text{E},j}) = \sum_j N_o^{\text{obs}}(t_{\text{E},j})$, η_o can take a random value because $\sum_j N_o^{\text{mod}}(t_{\text{E},j})$ is simply an expected number of the total event detections, and $\sum_j N_o^{\text{obs}}(t_{\text{E},j})$ can differ from it. Thus, η_o is chosen such that it minimizes $\chi_{t_{\text{E},o}}^2$ introduced below in every step of the MCMC fitting.

We consider χ^2 for the two t_{E} distributions by

$$\begin{aligned} \chi_{t_{\text{E}}}^2 &= \chi_{t_{\text{E}},\text{O}_{\text{hi}}}^2 + \chi_{t_{\text{E}},\text{O}_{\text{low}}}^2 \\ &= \sum_j \left(\chi_{t_{\text{E},j},\text{O}_{\text{hi}}}^2 + \chi_{t_{\text{E},j},\text{O}_{\text{low}}}^2 \right), \end{aligned} \quad (41)$$

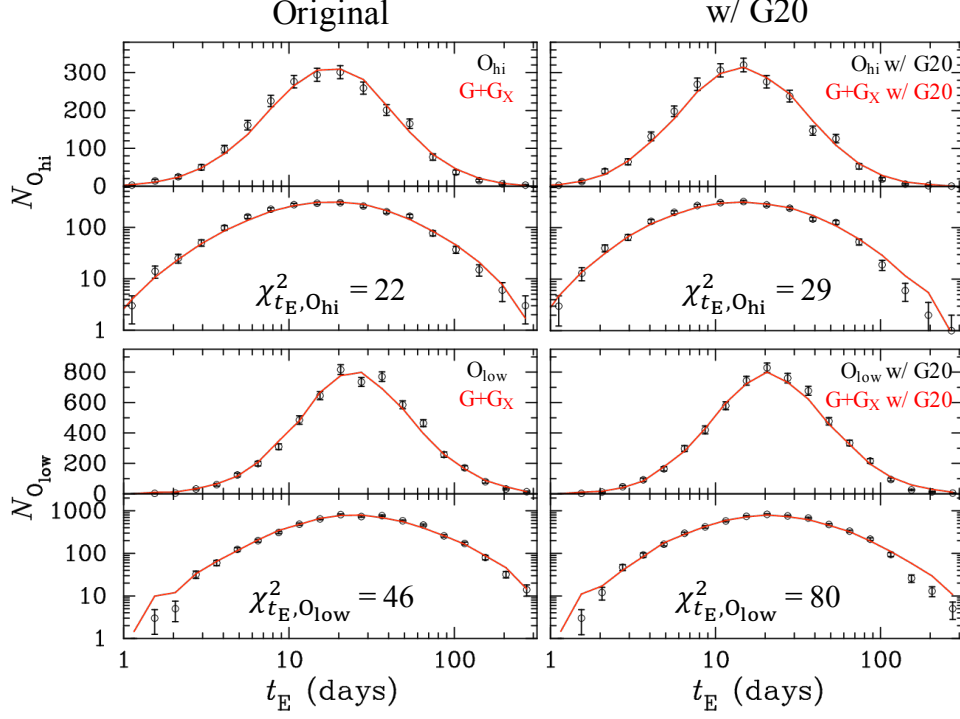


Figure 8. Left: The original OGLE-IV t_E distributions of 2212 events in the high-cadence fields by Mróz et al. (2017) (top) and 5788 events in the low-cadence fields by Mróz et al. (2019) (bottom). Right: Modified t_E distributions by applying the Golovich et al. (2020) correction with the Gaussian Process model (G20 option, considered in Appendix A). The black open circles and the red curves are indicated data and models, respectively.

where

$$\chi_{t_{E,j},o}^2 = \begin{cases} -2 \ln P[N_o^{\text{obs}}(t_{E,j}); N_o^{\text{mod}}(t_{E,j})] & \text{when } N_o^{\text{obs}}(t_{E,j}) \leq 15 \\ \left[\frac{N_o^{\text{mod}}(t_{E,j}) - N_o^{\text{obs}}(t_{E,j})}{N_o^{\text{err}}(t_{E,j})} \right]^2 & \text{when } N_o^{\text{obs}}(t_{E,j}) > 15 \end{cases} \quad (42)$$

with

$$N_o^{\text{err}}(t_{E,j}) = \langle \epsilon_o \rangle_j \sqrt{\sum_{i \in o} \frac{N_{\text{eve},i}^{\text{obs}}(t_{E,j})}{\epsilon_i^2(t_{E,j})}}.$$

Recall that $P(x; \lambda) = \lambda^x e^{-\lambda} / x!$ is the Poisson probability of x with the mean value λ . The uncertainty $N_o^{\text{err}}(t_{E,j})$ is not simply a square root of the sum of the Poisson errors of each $N_{\text{eve},i}^{\text{obs}}(t_{E,j})$, but instead, it is weighted by $1/\epsilon_i^2(t_{E,j})$. Therefore, this makes the $N_o(t_{E,j})$ distribution different from a simple Poisson probability distribution; however, we consider $\chi_{t_{E,j},o}^2$ with the Poisson distribution when $N_o^{\text{obs}}(t_{E,j})$ is small (≤ 15) because the dependency of $\epsilon_i(t_{E,j})$ on i (i.e., subfield) is much smaller than that on j (i.e., t_E), and the distribution is expected to remain similar to the Poisson distribution, especially when number of subfields contributing to $N_o^{\text{obs}}(t_{E,j})$ is small. Because the Poisson distribution can be approximated to the Gaussian distribution when $N_o^{\text{obs}}(t_{E,j})$ becomes larger, we consider $\chi_{t_{E,j},o}^2$ with the Gaussian distribution with $N_o^{\text{err}}(t_{E,j})$ to consider the weight of $1/\epsilon_i^2(t_{E,j})$.

4.2. Prior Constraints and χ^2 Penalty

Table 3. Priors used in fits for the bulge model and posterior values.

	Parameter	Reference	Value/Prior ^a	Posterior ^b
Sun	(R_{\odot}, z_{\odot}) [pc]	(1), (2)	(8160, 25)	(8160, 25)
	$(v_{\odot,x}, v_{\odot,y}, v_{\odot,z})$ [km/s]	(1)	(-10, 243, 7)	(-10, 243, 7)
Bulge	α_{bar} [deg.]	(1)	27	27
	M_{VVV} [$10^{10} M_{\odot}$]	(3)	1.32 ± 0.08	$1.14^{+0.10}_{-0.11}$
	$\langle \sigma_{v_{\text{B},x'}} \rangle$ [km/s]	(1), (4)	135 ± 5	$141.0^{+1.7}_{-4.4}$
	$\langle \sigma_{v_{\text{B},y'}} \rangle$ [km/s]	(1), (4)	105 ± 5	$113.6^{+3.4}_{-0.9}$
	$\langle \sigma_{v_{\text{B},z'}} \rangle$ [km/s]	(1), (4)	96 ± 5	$108.3^{+0.2}_{-1.7}$
	Ω_{p} [km/s/kpc]	(3)	39.0 ± 3.5	$45.9^{+4.0}_{-5.4}$
	IMF	M_{br} [M_{\odot}]	(5), (6)	0.60 ± 0.10
α_{hm}		(5), (6)	2.30 ± 0.10	$2.32^{+0.14}_{-0.10}$
α_{ms}		(5), (6)	1.30 ± 0.15	$1.16^{+0.08}_{-0.15}$
α_{bd}		(5)	0.30 ± 0.70	$0.22^{+0.20}_{-0.55}$

References—(1) Bland-Hawthorn & Gerhard (2016); (2) Gravity Collaboration et al. (2019); (3) Portail et al. (2017); (4) Portail et al. (2015); (5) Kroupa (2001); (6) Calamida et al. (2015).

^a $x \pm x_e$ indicates Gaussian prior and $\chi_{\text{pena}}^2 = \sum_x a_x \times (\frac{p_x - x}{x_e})^2$ is applied in the fit, where $a_x = 5$ for M_{VVV} and $a_x = 1$ for the others, and p_x is the value of parameter x in a given model.

^b Posterior values are from the best-fit G+G_X model in Table 5, and the uncertainties are combinations of statistic errors and systematic errors due to model choice.

We have prior information about certain fundamental parameters in our Galaxy from several previous studies, and reasonable prior constraints on such parameters help us efficiently examine the huge parameter space or disentangle degeneracies among fit parameters. Particularly, in this case where our parametric model lacks a dynamical consistency, prior constraints on the bulge mass or kinematic parameters help us avoid converging into a completely unphysical model.

Table 3 lists the fundamental parameters on which we apply prior constraints during the fit. Other than the solar position, velocity and bar angle that are fixed, there are 9 parameters: the model integrated mass within the VVV bulge box, M_{VVV} , mass-weighted velocity dispersions inside the bulge half mass radius, $\langle \sigma_{v_{\text{B},i}} \rangle$ ($i = x', y', z'$), bar pattern speed, Ω_{p} , three IMF slopes, (α_{hm} , α_{ms} , α_{bd}), and break mass, M_{br} , where the VVV bulge box is defined the central region inside $(x', y', z') = (\pm 2.2, \pm 1.4, \pm 1.2)$ kpc (Wegg & Gerhard 2013). Practically, we add a χ^2 penalty depending on a deviation from the applied prior value for each parameter, as described below.

Portail et al. (2017) found a total dynamical mass inside the VVV bulge box of $(1.85 \pm 0.05) \times 10^{10} M_{\odot}$, where the mass budget was $(0.32 \pm 0.05) \times 10^{10} M_{\odot}$ for dark matter, $0.2 \times 10^{10} M_{\odot}$ for a nuclear stellar disk in the very center, and the remaining $(1.32 \pm 0.08) \times 10^{10} M_{\odot}$ was for stellar

objects traceable by the RC stars. Because the data introduced in Section 4.1 is not sensitive to the central nuclear stellar disk with a ~ 50 pc scale height, we use $(1.32 \pm 0.08) \times 10^{10} M_{\odot}$ as a prior for M_{VVV} and apply a χ^2 penalty of $5 \times \left(\frac{M_{\text{VVV}} [10^{10} M_{\odot}] - 1.32}{0.08}\right)^2$ in the fit. Our best-fit models presented in Section 4.3 all have $M_{\text{VVV}} < 1.32 \times 10^{10} M_{\odot}$, and the large factor of 5 was multiplied by the χ^2 penalty to avoid needlessly reducing the bulge stellar mass, because our parametric Galactic model does not ensure dynamical consistency by itself. Note that the light stellar mass in the bulge region does not violate dynamics in itself; rather it indicates an additional stellar mass in a non-sensitive region and/or a larger dark matter mass fraction compared to the Portail et al. (2017) model. We discuss the implied dark matter mass in our model later, in Section 5.3.

For the mass-weighted velocity dispersions inside the bulge half mass radius, $\langle \sigma_{v_{\text{B}},i} \rangle$ ($i = x', y', z'$), we apply a χ^2 penalty of $\sum_{i=x',y',z'} \left(\frac{\langle \sigma_{v_{\text{B}},i} \rangle - \langle \sigma_{v_{\text{B}},i} \rangle_{\text{P15}}}{5 \text{ km/s}} \right)^2$, where $(\langle \sigma_{v_{\text{B}},x'} \rangle, \langle \sigma_{v_{\text{B}},y'} \rangle, \langle \sigma_{v_{\text{B}},z'} \rangle)_{\text{P15}} = (135, 105, 96)$ km/s that were derived by Bland-Hawthorn & Gerhard (2016) using the Portail et al. (2015) dynamical bulge model. Further, a χ^2 penalty of $\left(\frac{\Omega_{\text{p}} - 39.0}{3.5}\right)^2$ is applied for the pattern speed of Ω_{p} in unit of km/s/kpc based on the value derived by Portail et al. (2017).

For the IMF parameters, the following χ^2 penalties were applied for each slope and break mass; $\left(\frac{M_{\text{br}}/M_{\odot} - 0.60}{0.10}\right)^2$, $\left(\frac{\alpha_{\text{hm}} - 2.30}{0.10}\right)^2$, $\left(\frac{\alpha_{\text{ms}} - 1.30}{0.15}\right)^2$, and $\left(\frac{\alpha_{\text{bd}} - 0.30}{0.70}\right)^2$, where the prior values were determined based on the local IMF by Kroupa (2001) combined with the break mass at $\sim 0.56 M_{\odot}$ found by Calamida et al. (2015).

Hereafter, we denote the sum of the χ^2 penalty values for the above nine parameters by χ_{pena}^2 .

4.3. Fitting

4.3.1. Fitting procedure

We use the Markov Chain Monte Carlo (MCMC) methods (Metropolis et al. 1953) for our fitting. The bulge model consists of 39 fit parameters, i.e., 7–16, 19, and 4 parameters for the density (ρ_{B}), velocity (v_{B}), and IMF models, respectively. In the previous sections, we defined the following eight χ^2 values, χ_{RC}^2 for the OGLE-III RC star count data in 9019 lines of sight (Section 4.1.1), χ_{μ}^2 for the VIRAC proper motion measurements in 586 VVV sub-tiles (Section 4.1.2), χ_{BRA}^2 for the BRAVA radial velocity data in 82 fields (Section 4.1.3), $\chi_{N_{I < I_c}}^2$ ($I_c = 18, 21$) and $\chi_{f_{18/21}}^2$ for the OGLE-IV star count data in 1456 subfields (Section 4.1.4), $\chi_{N_{\text{eve}}}^2$ for the number of microlensing event detections as a function of t_{E} by the OGLE-IV survey in the 1456 subfields (Section 4.1.5), and $\chi_{t_{\text{E}}}^2$ for the two t_{E} distributions in the OGLE-IV high- and low-cadence fields divided into 20 $\log[t_{\text{E}}/\text{days}]$ bins (Section 4.1.5), in addition to the χ^2 penalty from priors on the nine parameters summarized in Table 3 (Section 4.2). Of the eight χ^2 values, χ_{μ}^2 and χ_{BRA}^2 depend on the ρ_{B} and v_{B} models, $\chi_{N_{I < I_c}}^2$ ($I_c = 18, 21$) depends on the ρ_{B} and IMF models, and $\chi_{N_{\text{eve}}}^2$ and $\chi_{t_{\text{E}}}^2$ depend on the ρ_{B} , v_{B} , and IMF models. Thus, ideally, all the 39 fit parameters are simultaneously fitted because of the correlations among the ρ_{B} , v_{B} , and IMF models in the parameter space.

However, such a simultaneous fit is difficult for the following reasons: First, the volume of the parameter space is very large and difficult to examine in a reasonable amount of time. Second, the probability density function of t_{E} , $f_i(t_{\text{E}})$, is needed to calculate $\chi_{N_{\text{eve}}}^2$, which involves time-consuming calculations, for a given combination of ρ_{B} , v_{B} , and IMF models. As described in Section 4.1.5, a representative $f_i(t_{\text{E}})$ can be used for models showing similar $\chi_{t_{\text{E}}}^2$, but it is difficult to ensure the similarity in such a simultaneous fit. Third, even if time permitted, the “best-fit” model depends

Table 4. Each step in the iterative process to find best-fit models.

Step	Fit parameters	Minimized χ^2	Input ^a	Output
1	$M_{\text{br}}, \alpha_{\text{hm}}, \alpha_{\text{ms}}, \alpha_{\text{bd}}, \rho_{0,\text{B}}$	$\tilde{\chi}_{\text{IMF}}^2 + \chi_{\text{pena}}^2$	Tentative best ρ_{B} and v_{B} models	$L_{\mathcal{M}_I}(\mathcal{M}_I), f_i(t_{\text{E},j})$
2	$\rho_{0,\text{B}}, \mathbf{p}_{r_s}, R_c$ + $x_{\text{KM,th}}$ for KM option + $f_{0,\text{X}}, \mathbf{p}_{r_s,\text{X}}, R_{c,\text{X}}, b_{\text{X}}$ for 2-comp. model	$\tilde{\chi}_{\rho_{\text{B}}}^2 + 5\chi_{\text{pena}}^2$	$L_{\mathcal{M}_I}(\mathcal{M}_I)$ & $f_i(t_{\text{E},j})$ from 1	ρ_{B} model
3	$\Omega_{\text{p}}, v_0^{\text{str}}, y_0^{\text{str}}, \sigma_{v_{\text{B}},i,0}, \sigma_{v_{\text{B}},i,1}, \mathbf{p}_{r_s,\sigma_R}, \mathbf{p}_{r_s,\sigma_z}$	$2\chi_{v_{\text{B}}}^2 + 5\chi_{\text{pena}}^2$	ρ_{B} model from 2	v_{B} model
4	Same as step 2	$\tilde{\chi}_{\rho_{\text{B}}}^2 + 2\chi_{v_{\text{B}}}^2 + 5\chi_{\text{pena}}^2$	v_{B} model from 3, $L_{\mathcal{M}_I}(\mathcal{M}_I)$ & $f_i(t_{\text{E},j})$ from 1	ρ_{B} model
5	Same as step 3	$2\chi_{v_{\text{B}}}^2 + 5\chi_{\text{pena}}^2$	ρ_{B} model from 4	v_{B} model

^aInput models or functions are fixed during each step other than $\rho_{0,\text{B}}$ in step 1.

^b $\tilde{\chi}_{\text{IMF}}^2 \equiv \chi_{t_{\text{E}}}^2 + 0.2(\chi_{N_{I<21}}^2 + \chi_{N_{I<18}}^2 + \chi_{f_{18/21}}^2)/3$, $\tilde{\chi}_{\rho_{\text{B}}}^2 \equiv \chi_{\text{RC}}^2 + \chi_{N_{I<21}}^2 + \chi_{N_{I<18}}^2 + 2\chi_{N_{\text{eve}}}^2$, and $\chi_{v_{\text{B}}}^2 \equiv \chi_{\mu}^2 + \chi_{\text{BRA}}^2$.

on what χ^2 value was minimized in the fit. Because the number of data points in the used datasets ranges from 40 bins for $\chi_{t_{\text{E}}}^2$ to 9019×3 for χ_{RC}^2 , agreement to a small dataset could be neglected depending on arbitrarily selected weights among the eight χ^2 values. The weights are ideally 1 if every data does not contain any systematic error, and the model selection is perfect; however, since neither of these statements is true, the “best-fit” model would be dominated by an arbitrary choice of weights.

Because of these difficulties associated with the simultaneous fit, we perform modeling by iterating the following step-by-step procedure, where steps 1–5 are also summarized in Table 4:

0. At the beginning, tentative best-fit ρ_{B} and v_{B} models are determined to use in step 1 by performing steps 2–5 without using $\chi_{t_{\text{E}}}^2$, $\chi_{N_{I<21}}^2$, $\chi_{N_{I<18}}^2$, $\chi_{f_{18/21}}^2$, or $\chi_{N_{\text{eve}}}^2$. The Kroupa (2001) IMF is used when an IMF is needed.
1. An IMF model is determined by minimizing $\tilde{\chi}_{\text{IMF}}^2 + \chi_{\text{pena}}^2$, where χ^2 to evaluate an IMF model is defined as $\tilde{\chi}_{\text{IMF}}^2 \equiv \chi_{t_{\text{E}}}^2 + 0.2(\chi_{N_{I<21}}^2 + \chi_{N_{I<18}}^2 + \chi_{f_{18/21}}^2)/3$, and the best-fit ρ_{B} and v_{B} models from the previous run or from step 0 are fixed and used. Subsequently, the probability density function of t_{E} in i th subfield, $f_i(t_{\text{E}})$, is calculated using the ρ_{B} , v_{B} , and IMF models. The luminosity function $L_{\mathcal{M}_I}(\mathcal{M}_I)$ is calculated using the IMF model. A $\chi_{t_{\text{E}}}^2$ value, $\chi_{t_{\text{E},\text{ini}}}^2$, is calculated using the ρ_{B} , v_{B} , and IMF models.
2. A ρ_{B} model is determined by minimizing $\tilde{\chi}_{\rho_{\text{B}}}^2 + 5\chi_{\text{pena}}^2$, where χ^2 to evaluate a ρ_{B} model is defined as $\tilde{\chi}_{\rho_{\text{B}}}^2 \equiv \chi_{\text{RC}}^2 + \chi_{N_{I<21}}^2 + \chi_{N_{I<18}}^2 + 2\chi_{N_{\text{eve}}}^2$, and the $f_i(t_{\text{E}})$ and $L_{\mathcal{M}_I}(\mathcal{M}_I)$ from step 1 are fixed and used.
3. A v_{B} model is determined by minimizing $2\chi_{v_{\text{B}}}^2 + 5\chi_{\text{pena}}^2$, where χ^2 to evaluate a v_{B} model is defined as $\chi_{v_{\text{B}}}^2 \equiv \chi_{\mu}^2 + \chi_{\text{BRA}}^2$, and the best-fit ρ_{B} model from step 2 is fixed and used.
4. The ρ_{B} model from step 2 is updated by minimizing $\tilde{\chi}_{\rho_{\text{B}}}^2 + 2\chi_{v_{\text{B}}}^2 + 5\chi_{\text{pena}}^2$, where the best-fit v_{B} model from step 3 is fixed and used.
5. The v_{B} model from step 3 is updated by minimizing $2\chi_{v_{\text{B}}}^2 + 5\chi_{\text{pena}}^2$, where the best-fit ρ_{B} model from step 4 is fixed and used.

6. A $\chi_{t_E}^2$ value, $\chi_{t_E,\text{fin}}^2$, is calculated using the ρ_B , v_B , and IMF models from steps 4, 5, and 1, respectively. If $|\chi_{t_E,\text{ini}}^2 - \chi_{t_E,\text{fin}}^2| < 4$, the iteration is stopped; otherwise, steps 1–6 are repeated.

It is difficult to systematically determine weights among various datasets suffering from different systematic errors; therefore, a factor multiplied by each χ^2 value is subjectively selected in our attempt to find a proper balance between large and small datasets. We multiply 2 by $\chi_{N_{\text{eve}}}^2$ in $\tilde{\chi}_{\rho_B}^2$ because our interest is in microlensing study, and we want to have a better agreement on it. Further, we multiply 2 by $\chi_{v_B}^2$ because the number of data points contributed is ~ 30 times fewer than $\tilde{\chi}_{\rho_B}^2$. χ_{pena}^2 is multiplied by 5 in steps 2–5 because the χ_{pena}^2 is the sum of the χ^2 penalty set on the nine quantities, as the effect is otherwise easily diminished by a small improvement of $\chi_{v_B}^2$ or $\tilde{\chi}_{\rho_B}^2$, which could be falsely caused due to systematic errors in data.

In step 1, we fit the four parameters for the IMF and the mass normalization factor, $\rho_{0,B}$, by minimizing $\tilde{\chi}_{\text{IMF}}^2$, which concerns not only agreement with the t_E distribution by $\chi_{t_E}^2$, but also agreement with star count data via the $\chi_{N_{I<21}}^2$, $\chi_{N_{I<18}}^2$, and $\chi_{f_{18/21}}^2$ values. This is because the model values for the star count data given by Eq. (33) are calculated using the luminosity function $L_{\mathcal{M}_I}(\mathcal{M}_I)$, and $L_{\mathcal{M}_I}(\mathcal{M}_I)$ is calculated using a given IMF. The sum of the three χ^2 values for the OGLE-IV star count data, $\chi_{N_{I<21}}^2 + \chi_{N_{I<18}}^2 + \chi_{f_{18/21}}^2$, are multiplied by $0.1 \times 2/3$ in $\tilde{\chi}_{\text{IMF}}^2$ because the number of data values are 1456 for each of the three datasets compared with 40 for the t_E distribution, and we desire to place a larger weight on t_E because $\chi_{N_{I<21}}^2 + \chi_{N_{I<18}}^2$ is also included in $\tilde{\chi}_{\rho_B}^2$. The factor $2/3$ is multiplied because only two of the three datasets, $N_{I<21}$, $N_{I<18}$, and $f_{18/21}$ ($= N_{I<18}/N_{I<21}$), are independent data.

As mentioned in Section 4.1.5, the χ^2 for the number of microlensing event detections, $\chi_{N_{\text{eve}}}^2$, is insensitive to a variation of the probability density function for t_E in i th subfield, $f_i(t_E)$, till the models used to calculate $f_i(t_E)$ show similar values of $\chi_{t_E}^2$, the χ^2 for the shape of the t_E distribution. In the fitting procedure, we use the same $f_i(t_E)$ from step 1 throughout steps 2–6, where $\chi_{N_{\text{eve}}}^2$ contributes to $\chi_{\rho_B}^2$ in steps 2 and 4. Using the same $f_i(t_E)$ can be justified only when $\chi_{t_E,\text{ini}}^2$ is similar to $\chi_{t_E,\text{fin}}^2$, and thus a similarity between the two values is used as the condition to end the iteration. The differences among different iteration runs are $f_i(t_E)$ and the IMF model, and the condition ensures convergences of not only $f_i(t_E)$, but also the IMF, because the IMF parameters are primarily determined by shape of t_E distribution when the ρ_B and v_B models are sufficiently constrained by other datasets. Note that $\chi_{N_{\text{eve}}}^2$ is only used to find the best-fit ρ_B models because a model value for the number of microlensing events with $t_{E,j}$ in i th subfield, $N_{\text{eve},i}^{\text{mod}}(t_{E,j})$, given by Eq. (36) is independent of the v_B and IMF models once $f_i(t_E)$ is fixed.

We use a Monte Carlo simulation of 3×10^6 microlensing events to calculate the model values for the t_E distribution, $N_o^{\text{mod}}(t_{E,j})$ ($o = \text{O}_{\text{hi}}, \text{O}_{\text{low}}$), which takes ~ 20 s to calculate a $\chi_{t_E}^2$ value under our computational environment. This causes a dispersion of $\chi_{t_E}^2$ values ~ 1.3 depending on the random seed value. Thus, we conduct MCMC fits in step 1 with a temperature of $T_{\text{MCMC}} \geq 4$ to avoid being stuck at a local minimum created due to the random noise, where a proposed parameter set with $\Delta\chi^2 > 0$ is accepted with a probability $\exp[-0.5 \Delta\chi^2/T_{\text{MCMC}}]$ in an MCMC run. As a result of this, we use $|\chi_{t_E,\text{ini}}^2 - \chi_{t_E,\text{fin}}^2| < 4$ as the condition in step 6. Note that the $\chi_{t_E,\text{ini}}^2$ and $\chi_{t_E,\text{fin}}^2$ values are calculated with a Monte Carlo simulation of 3×10^7 events, which is 10 times the one during the MCMC calculations.

It is important to ensure that a solution from the MCMC fit with the $\chi_{t_E}^2$ dispersion of ~ 1.3 is not plagued by the random noise. In Section 4.4, we compare the best-fit model from our fitting

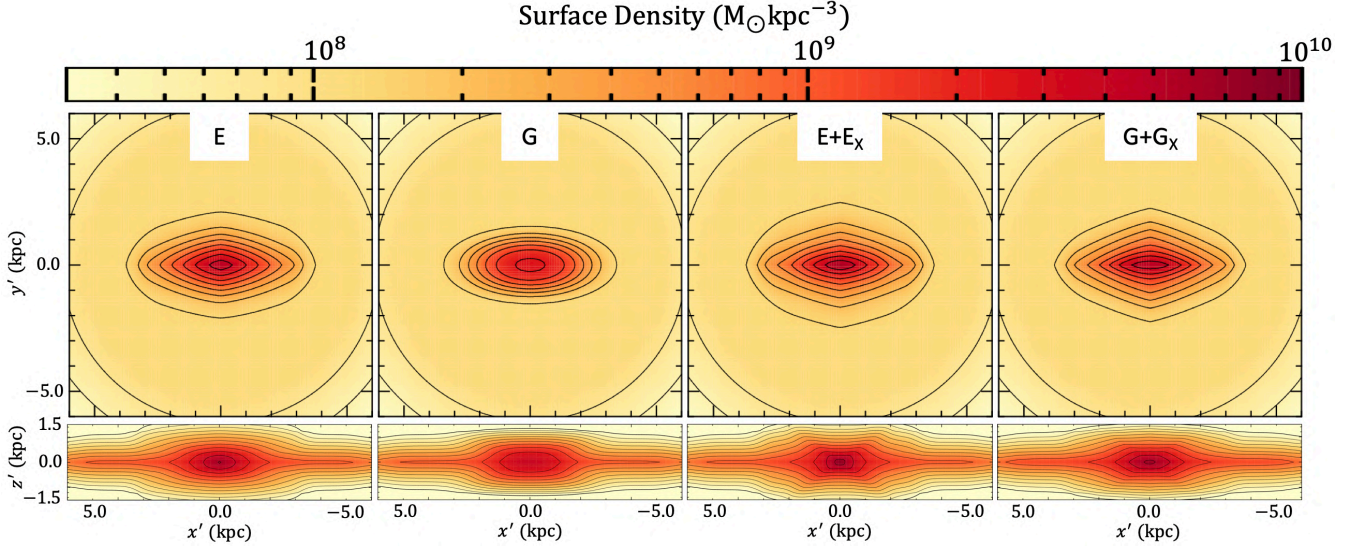


Figure 9. Surface density distributions along the bar-axes of the two one-component models (E and G) and two two-components models (E+E_X and G+G_X). Parameters of each model are listed in Table 5. Note that the plotted surface density does not include the contribution from very centered or very thin components such as a nuclear stellar disk (Launhardt et al. 2002; Nishiyama et al. 2013; Portail et al. 2017) or thin bar components (Wegg et al. 2015). We neither confirm nor confute existence of such components in this paper because we lack data in $|b| \lesssim 2^\circ$ or in $|l| > 10^\circ$.

procedure with the best-fit model from a grid search where $\chi^2_{t_E}$ at each grid is calculated with 3×10^7 events. We find a consistency between them, and confirm that the settings for the fitting procedure have successfully determined a converged solution.

In the Monte Carlo simulation of microlensing events, we also consider binary systems for lens objects, which are generated by following the binary distribution developed by Koshimoto et al. (2020) based on Duchêne & Kraus (2013). Because Mróz et al. (2017) and Mróz et al. (2019) did not include binary lens events in the OGLE-IV t_E distributions, we reject a detectable binary system whose central caustic size w_{LC} is larger than the impact parameter u_0 , where u_0 is randomly generated uniformly from 0 to 1 in each trial of the Monte Carlo simulation. We use $w_{LC} = 4q_{LC}/(s_{LC} - s_{LC}^{-1})^2$ (Chung et al. 2005) with the mass ratio, q_{LC} , and the separation in unit of the angular Einstein radius θ_E , s_{LC} . Although the formula for w_{LC} is an approximation for the planetary mass-ratio of $q_{LC} \ll 1$, Koshimoto et al. (2020) found that the criterion $w_{LC} < u_0$ itself works reasonably well even for a stellar mass-ratio because of the extension of θ_E by a factor $\sqrt{1 + q_{LC}}$. Section 10.3.1 of Koshimoto et al. (2020) presents a more detailed discussion. Because a tight close binary system with $s_{LC} \ll 1$ can be undetectable under this criterion, the resulting t_E distribution includes their contribution, as well as single star lens systems. Such a binary system has a lens mass equal to the total system mass, and their fraction for each t_E bin ranges from $\lesssim 3\%$ for $t_E < 10$ days to 10–14% for $t_E > 50$ days.

4.3.2. Best-Fit Models

As described in Section 2.3.1, we consider four different shapes for the ρ_B model: two one-component models (E and G models) and two two-components models (E+E_X and G+G_X models). For each of the E, G, E+E_X, and G+G_X models, we consider four options, corresponding to the four disk

Table 5. Best-fit parameters for each model.

Model	IMF model						ρ_B model							
	$\tilde{\chi}_{\text{sum}}^2$ ^a	$\tilde{\chi}_{\text{IMF}}^2$ ^a	M_{br} [M_{\odot}]	α_{hm}	α_{ms}	α_{bd}	$\tilde{\chi}_{\rho_B}^2$ ^a	$\rho_{0,B}$ [M_{\odot}/pc^3]	x_0 [kpc]	y_0 [kpc]	z_0 [kpc]	C_{\perp}	C_{\parallel}	R_c [kpc]
E	80173	355	0.84	2.31	1.10	0.18	75481	9.72	0.67	0.28	0.24	1.4	3.3	2.8
G	91319	391	0.90	2.40	1.18	0.17	86105	2.43	1.03	0.46	0.40	2.0	4.0	4.8
E+E _X	76261	342	0.86	2.32	1.13	0.18	72147	4.12	0.93	0.37	0.24	1.2	4.1	2.6
G+G _X	76500	337	0.90	2.32	1.16	0.22	72585	0.88	1.56	0.72	0.49	1.2	3.1	2.8

Model	ρ_B model								v_B model					
	$f_{0,X}$	b_X	$x_{0,X}$ [kpc]	$y_{0,X}$ [kpc]	$z_{0,X}$ [kpc]	$C_{\perp,X}$	$C_{\parallel,X}$	$R_{c,X}$ [kpc]	$\chi_{v_B}^2$ ^a	Ω_P [km/s/kpc]	v_0^{str} [km/s]	y_0^{str} [pc]	$\sigma_{v_B,x',0}$ [km/s]	$\sigma_{v_B,y',0}$ [km/s]
E	–	–	–	–	–	–	–	–	2203	49.5	49	393	64	75
G	–	–	–	–	–	–	–	–	2382	40.5	12	20	76	68
E+E _X	1.44	1.38	0.28	0.18	0.29	1.3	2.2	1.3	1908	47.4	43	407	64	76
G+G _X	3.00	1.38	0.76	0.31	0.40	1.2	1.3	5.2	1831	45.9	28	11	64	75

Model	v_B model													
	$\sigma_{v_B,z',0}$ [km/s]	$\sigma_{v_B,x',1}$ [km/s]	$\sigma_{v_B,y',1}$ [km/s]	$\sigma_{v_B,z',1}$ [km/s]	x_{0,σ_R} [kpc]	y_{0,σ_R} [kpc]	z_{0,σ_R} [kpc]	C_{\perp,σ_R}	C_{\parallel,σ_R}	$x_{0,\sigma_{z'}}$ [kpc]	$y_{0,\sigma_{z'}}$ [kpc]	$z_{0,\sigma_{z'}}$ [kpc]	$C_{\perp,\sigma_{z'}}$	$C_{\parallel,\sigma_{z'}}$
E	72	156	84	86	0.82	9.29	0.86	3.8	1.0	0.51	2.90	2.19	3.0	1.0
G	75	136	109	101	1.03	2.15	0.73	4.9	1.0	0.52	1.44	1.10	2.3	1.0
E+E _X	71	152	78	82	0.86	3.22	0.95	4.3	1.0	0.56	2.00	3.82	3.7	1.1
G+G _X	70	155	78	83	0.94	4.23	0.88	4.6	1.0	0.70	1.73	2.03	4.8	1.0

^a $\tilde{\chi}_{\text{sum}}^2 \equiv \tilde{\chi}_{\rho_B}^2 + 2\chi_{v_B}^2 + 5\chi_{\text{pena}}^2$, $\tilde{\chi}_{\text{IMF}}^2 \equiv \chi_{t_E}^2 + 0.2(\chi_{N_{I<21}}^2 + \chi_{N_{I<18}}^2 + \chi_{f_{18/21}}^2)/3$, $\tilde{\chi}_{\rho_B}^2 \equiv \chi_{\text{RC}}^2 + \chi_{N_{I<21}}^2 + \chi_{N_{I<18}}^2 + 2\chi_{N_{\text{eve}}}^2$, and $\chi_{v_B}^2 \equiv \chi_{\mu}^2 + \chi_{\text{BRA}}^2$.

models in Table 2. We derived the best-fit parameters for each option with each model by the fitting procedure described in Section 4.3.1. We define another χ^2 value, $\tilde{\chi}_{\text{sum}}^2 = \tilde{\chi}_{\rho_B}^2 + 2\chi_{v_B}^2 + 5\chi_{\text{pena}}^2$, and use its difference, $\Delta\tilde{\chi}_{\text{sum}}^2$, to indicate the better model among them. The χ^2 for the t_E distributions, $\chi_{t_E}^2$, is not considered in $\tilde{\chi}_{\text{sum}}^2$ because the information contained in $\chi_{t_E}^2$ is included in the χ^2 for the number of microlensing event detections as a function of t_E , $\chi_{N_{\text{eve}}}^2$, in a more statistically proper style. Although this inclusion is only for the fields covered by Nataf et al. (2013), we conservatively avoid the partial overlap. In this subsection, we determine the best-fit model for each of the E, G, E+E_X, and G+G_X models by selecting the best option from the four based on comparisons using $\Delta\tilde{\chi}_{\text{sum}}^2$.

Among the four disk models in Table 2, we decide to use the all- z + flat $z_{\text{d}}^{\text{thin}}$ model based on the following two comparisons. The first comparison is between the all- z and low- z models, where we find $\Delta\tilde{\chi}_{\text{sum}}^2 < 100$ between the two, which is not considered significant. Thus, we select the all- z models because it is more broadly applicable compared to the low- z models optimized for bulge sky. The second comparison is between the flat- and linear-scale height models, where we find that the best-fit model with the flat-scale height model is preferable to the linear-scale height model by $\Delta\tilde{\chi}_{\text{sum}}^2 > 1000$. Half of this preference comes from $\chi_{N_{I<21}}^2 + \chi_{N_{I<18}}^2$ while the other half comes from $2\chi_{v_B}^2$. These results barely depend on the choice of E, G, E+E_X, and G+G_X models, and we select the all- z + flat $z_{\text{d}}^{\text{thin}}$ model as the fiducial disk model for all of them.

In Appendix A, we consider another option of using a different dataset of the OGLE-IV t_E measurements. In this dataset, the original light curve data are the same as those by Mróz et al. (2017, 2019), but the Gaussian Process model developed by Golovich et al. (2020) is applied for the t_E

measurements. Appendix A presents a comparison of χ^2 values between the best-fit models with the original t_E distributions by Mróz et al. (2017, 2019) and the best-fit models with the t_E distributions with the Golovich et al. (2020) model, where we find that the original Mróz et al.’s t_E distributions are favored with respect to the $\tilde{\chi}_{\text{sum}}^2$, $\chi_{N_{\text{eve}}}^2$, and $\chi_{t_E}^2$ values.

Table 5 lists all the best-fit parameters for the fiducial four models. Figs. 4–8 present comparisons between the data and model values using the four models from Table 5, where we show χ_p^2 values for each parameter p in each panel of Figs. 4, 6, and 8, while Figs. 5 and 7 show the residuals corresponding to Figs. 4 and 6, respectively. Fig. 9 shows the surface density distributions of each best-fit model.

Among the four models, we find that the two-components models are more favorable than the one-component models by $\Delta\tilde{\chi}_{\text{sum}}^2 > 3600$. The E model is preferred over the G model by $\Delta\tilde{\chi}_{\text{sum}}^2 \sim 11000$ in the one-component models. By contrast, the two two-component models (E+E_X vs. G+G_X) show very similar $\tilde{\chi}_{\text{sum}}^2$ values, as described in Section 2.3.1.

4.4. Uncertainty Assessments for Fundamental Parameters

The far-right column in Table 3 presents the posterior values for the fundamental parameters on which we applied the prior in the fits. The fiducial values are from the best-fit G+G_X model, while the uncertainties are combinations of statistical and systematic errors for each parameter.

The systematic errors are taken from the variation of each value depending on the model choice listed in Table 5. These are the stellar mass within the VVV bulge box ($\pm 2.2 \times \pm 1.4 \times \pm 1.2$ kpc), $M_{\text{VVV}} = 1.14_{-0.11}^{+0.00}|_{\text{sys.}} \times 10^{10} M_{\odot}$, mass-weighted velocity dispersions inside the bulge half mass radius along the bar axes, $(\langle\sigma_{v_B, x'}\rangle, \langle\sigma_{v_B, y'}\rangle, \langle\sigma_{v_B, z'}\rangle) = (141.0_{-3.8}^{+0.0}|_{\text{sys.}}, 113.6_{-0.0}^{+3.2}|_{\text{sys.}}, 108.3_{-1.5}^{+0.0}|_{\text{sys.}})$ km/s, bar pattern speed, $\Omega_p = 45.9_{-5.4}^{+3.6}|_{\text{sys.}}$ km/s/kpc, break mass in the IMF, $M_{\text{br}} = 0.90_{-0.06}^{+0.00}|_{\text{sys.}} M_{\odot}$, and IMF slopes for three different mass regions, $(\alpha_{\text{hm}}, \alpha_{\text{ms}}, \alpha_{\text{bd}}) = (2.32_{-0.01}^{+0.08}|_{\text{sys.}}, 1.16_{-0.06}^{+0.02}|_{\text{sys.}}, 0.22_{-0.05}^{+0.00}|_{\text{sys.}})$. The representative values are for the best-fit G+G_X model, and the 0 error values indicate that the G+G_X model has the largest or lowest values among the four models in Table 5.

Statistical errors for the four velocity parameters are determined using the posterior distribution for the G+G_X model taken from the MCMC calculation in step 5 in our fitting procedure that is described in Section 4.3.1. These are $(\langle\sigma_{v_B, x'}\rangle, \langle\sigma_{v_B, y'}\rangle, \langle\sigma_{v_B, z'}\rangle) = (141.0_{-2.2}^{+1.7}|_{\text{stat.}}, 113.6_{-0.9}^{+1.0}|_{\text{stat.}}, 108.3_{-0.9}^{+0.2}|_{\text{stat.}})$ km/s and $\Omega_p = 45.9_{-0.2}^{+0.6}|_{\text{stat.}}$ km/s/kpc.

Although we have a posterior distribution from the MCMC calculation in step 1 for the other five parameters, M_{VVV} , M_{br} , α_{hm} , α_{ms} , and α_{bd} , the distribution is contaminated by the dispersion of $\chi_{t_E}^2$ values of ~ 1.3 due to the limited sample size of simulated events (3×10^6 events) in each step of the MCMC calculation. Thus, we use the $\Delta\chi^2$ distributions from a grid search with a ten times larger sample size of 3×10^7 events to determine statistical errors for the five parameters. Fig. 10 shows the resultant $\Delta(\tilde{\chi}_{\text{IMF}}^2 + \chi_{\text{pena}}^2)$ maps calculated with the best-fit G+G_X ρ_B and v_B models. In the grid search, a grid is specified by a combination of $(M_{\text{br}}, \alpha_{\text{hm}}, \alpha_{\text{ms}}, \alpha_{\text{bd}})$ distributed uniformly, and the mass normalization factor $\rho_{0,B}$, which is represented by M_{VVV} here, is adjusted such that the $\tilde{\chi}_{\text{IMF}}^2 + \chi_{\text{pena}}^2$ for each grid is minimized.

The best-fit parameters from the grid search are $(M_{\text{VVV}}, M_{\text{br}}, \alpha_{\text{hm}}, \alpha_{\text{ms}}, \alpha_{\text{bd}}) = (1.16 \times 10^{10} M_{\odot}, 0.90 M_{\odot}, 2.30, 1.15, 0.20)$, which are almost identical to the best-fit G+G_X model parameters of $(1.14 \times 10^{10} M_{\odot}, 0.90 M_{\odot}, 2.32, 1.16, 0.22)$ considering the limited resolution of the grid search. These two sets of parameters can be, in principle, different because the grid search uses the ρ_B and v_B models obtained from the last iteration of our fitting procedure, whereas the IMF parameters of

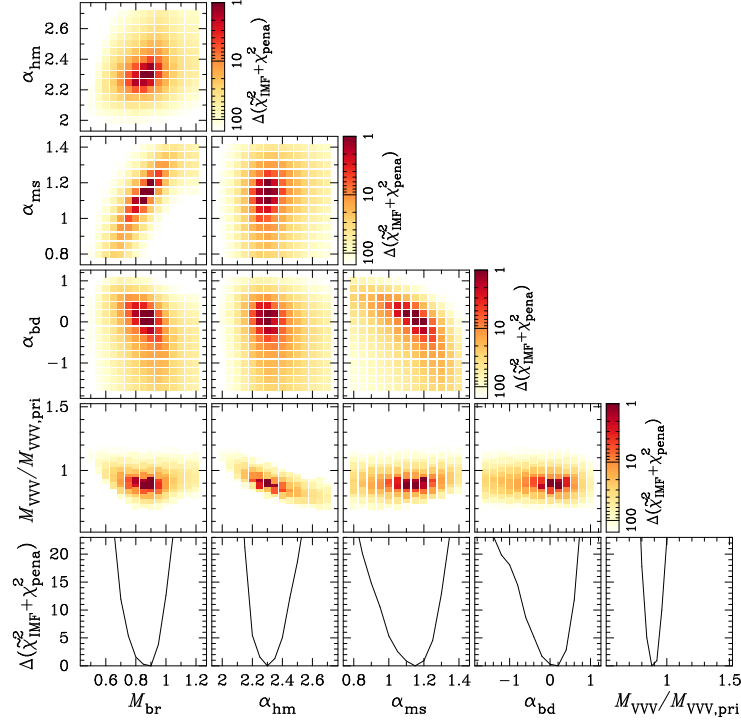


Figure 10. $\Delta(\tilde{\chi}_{\text{IMF}}^2 + \chi_{\text{pena}}^2)$ map calculated through a grid-search with the best-fit G+G_X ρ_B and v_B models. $M_{\text{VVV,pri}}$ indicates prior value for M_{VVV} of $1.32 \times 10^{10} M_{\odot}$.

the best-fit G+G_X model are determined using the tentative best-fit ρ_B and v_B models from the last but one iteration. Therefore, the identity of these two sets of parameters confirms a convergence of our iterative fitting procedure. This also ensures that the number of simulated events used in the MCMC fit, 3×10^6 , was sufficient to find the best-fit parameters.

We use $\Delta(\tilde{\chi}_{\text{IMF}}^2 + \chi_{\text{pena}}^2) = 4$ as the threshold value to determine the statistical errors for the five parameters because the grid search is based on the best-fit ρ_B and v_B models determined using the IMF parameters from step 1 in which the MCMC temperature of $T_{\text{MCMC}} = 4$ is used. This yields $(M_{\text{VVV}}, M_{\text{br}}, \alpha_{\text{hm}}, \alpha_{\text{ms}}, \alpha_{\text{bd}}) = (1.14_{-0.02}^{+0.10}|_{\text{stat.}} \times 10^{10} M_{\odot}, 0.90_{-0.13}^{+0.05}|_{\text{stat.}} M_{\odot}, 2.32_{-0.10}^{+0.07}|_{\text{stat.}}, 1.16_{-0.14}^{+0.08}|_{\text{stat.}}, 0.22_{-0.55}^{+0.20}|_{\text{stat.}})$. By combining the statistical and systematic errors above, we derive the posterior values listed in Table 3. Note that these error estimates could be influenced by our non-standard fitting method, an iterative step-by-step procedure, described in Section 4.3.1.

5. DISCUSSION

In this section, we discuss several fundamental parameters in our Galaxy measured through our modeling process throughout Sections 3 and 4 by comparison to previous studies. In Section 5.1, we discuss the 10 best-fit parameters for the v_d models in Table 2. Section 5.2 examines how the IMF parameters are constrained in our model framework, and compares these IMF parameters with a local IMF by Kroupa (2001) and a bulge IMF by Zoccali et al. (2000). In Section 5.3, we derive the stellar mass-to-light ratio corresponding to our IMF and estimate the dark matter fraction inferred from our results.

5.1. Disk Velocity Parameters

A review paper by Bland-Hawthorn & Gerhard (2016) summarizes estimates on the local velocity dispersion values and the scale lengths of the distributions from several previous studies (see their Table 5). The local velocity dispersion values for the thin disk range from 34 (Piffl et al. 2014) to 48 km/s (Sanders & Binney 2015) for $\sigma_{R,\odot}^{\text{thin}}$ and from 20 (Binney 2012) to 31 km/s (Sanders & Binney 2015) for $\sigma_{z,\odot}^{\text{thin}}$, and our best-fit values in Table 2 are consistent with the estimates for these two parameters in any of the four models considered.

Binney (2012) is the only one who did a fit to the scale length of the velocity dispersion along R for the thin disk, $R_{\sigma_R}^{\text{thin}}$, in the summary by Bland-Hawthorn & Gerhard (2016). Their estimate is $R_{\sigma_R}^{\text{thin}} = 3.3\text{--}20$ kpc, which includes our estimated values for all models other than the all- z + linear $z_{\text{d}}^{\text{thin}}$ model. The value for the all- z + linear $z_{\text{d}}^{\text{thin}}$ model is $R_{\sigma_R}^{\text{thin}} = 21.4$ kpc, and it is only slightly outside the range presented by Binney (2012).

No study has presented a fit to the scale length of the velocity dispersion along z for the thin disk, $R_{\sigma_z}^{\text{thin}}$, in the summary by Bland-Hawthorn & Gerhard (2016), but some studies fixed the value at 9.0 (Piffl et al. 2014), 7.8 (Sanders & Binney 2015), and 7.4 kpc (Binney & Piffl 2015) in their analysis. Our estimates on $R_{\sigma_z}^{\text{thin}}$ ranging from 5.9–10.4 kpc are consistent with these values. The all- z + flat $z_{\text{d}}^{\text{thin}}$ model, which is our fiducial disk model selected in Section 4.3.2, has $R_{\sigma_z}^{\text{thin}} = 5.9$ kpc which is shorter than the fixed values in the previous papers, though.

Further, our estimates on the slope of age-velocity dispersion relation are $\beta_R = 0.22\text{--}0.34$ and $\beta_z = 0.77\text{--}0.82$, which are fully and fairly consistent with the estimates by Yu & Liu (2018) of $\beta_R = 0.28 \pm 0.08$ and $\beta_z = 0.54 \pm 0.13$, respectively.

By contrast, our estimates for some parameters for the thick disk show inconsistency with previous studies. In Table 5 of Bland-Hawthorn & Gerhard (2016), the local velocity dispersion values for the thick disk range from 25 (Binney 2012) to 53 km/s (Binney & Piffl 2015) for $\sigma_{R,\odot}^{\text{thick}}$ and from 33 to 65 km/s (Binney 2012) for $\sigma_{z,\odot}^{\text{thick}}$, while our estimate for these parameters are $\sigma_{R,\odot}^{\text{thick}} = 68\text{--}75$ km/s and $\sigma_{z,\odot}^{\text{thick}} = 47.8\text{--}61.4$ km/s. Therefore, our estimate on $\sigma_{R,\odot}^{\text{thick}}$ is significantly higher than the values in previous studies.

Similarly, our estimates on the scale lengths of the velocity dispersion are $R_{\sigma_R}^{\text{thick}} = 47.0\text{--}180$ kpc and $R_{\sigma_z}^{\text{thick}} = 6.9\text{--}52.0$ kpc, which are both longer than $R_{\sigma_R}^{\text{thick}} = 13$ kpc (Piffl et al. 2014) or 11.6 kpc (Binney & Piffl 2015) and $R_{\sigma_z}^{\text{thick}} = 4.2$ kpc (Piffl et al. 2014) or 5.0 kpc (Binney & Piffl 2015), respectively. These differences probably arise from our rejection of the outer disk ($R > 8440$ pc) region. In contrast to our preference for the inner disk, most of the previous studies used data primarily from the outer disk rather than the inner disk.

5.2. IMF Parameters

Several studies measured the IMF parameters in the bulge field, and two approaches have been attempted so far. One approach is measuring a very deep luminosity function and deriving the IMF slopes by fitting to it using a mass–luminosity relation. With this approach, Zoccali et al. (2000) found that a single power–law model of $M^{-1.33}$ had a good agreement in $0.15 M_{\odot} < M < 1.00 M_{\odot}$ for the luminosity function measured toward $(l, b) = (0.277, -6.167)$ using the *HST*. Calamida et al. (2015) also used the *HST* to observe a luminosity function at $(l, b) = (1.25, -2.65)$ and derived $M_{\text{br}} \sim 0.56 M_{\odot}$ and $(\alpha_{\text{hm}}, \alpha_{\text{ms}}) = (2.41 \pm 0.50, 1.25 \pm 0.20)$ in $0.15 M_{\odot} < M < 1.00 M_{\odot}$. This approach lacks sensitivity to α_{bd} because brown dwarfs are too faint to be observed in a bulge field.

The other approach, in which the t_{E} distributions from microlensing surveys are used, has an advantage with regard to sensitivity to the brown dwarf population, although the IMF measured

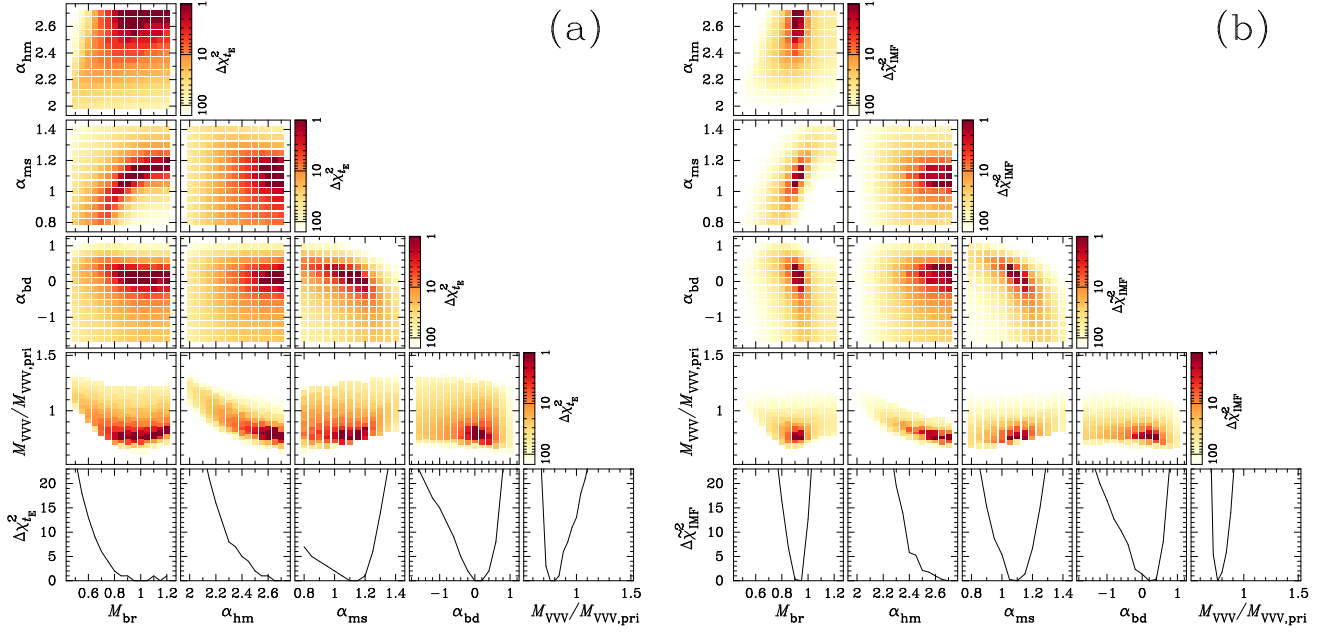


Figure 11. Same as Fig. 10, but for (a) $\Delta\chi_{t_E}^2$ and (b) $\Delta\tilde{\chi}_{\text{IMF}}^2$, where $\chi_{t_E}^2$ is for the OGLE-IV t_E distributions and $\tilde{\chi}_{\text{IMF}}^2 = \chi_{t_E}^2 + 0.2(\chi_{N_{I<21}}^2 + \chi_{N_{I<18}}^2 + \chi_{f_{18/21}}^2)/3$ involves the three χ^2 values for the OGLE-IV star count data, in addition to $\chi_{t_E}^2$.

from this method somewhat depends on what Galactic model is used to calculate the $t_E/\sqrt{M_L} = \sqrt{\kappa\pi_{\text{rel}}}/\mu_{\text{rel}}$ distribution. Sumi et al. (2011) measured $\alpha_{\text{bd}} = 0.50^{+0.36}_{-0.60}$ by comparing a parametric Galactic model based on Han & Gould (1995) with the t_E distribution of 474 events observed by the MOA-II survey. Mróz et al. (2017) analyzed the t_E distribution of 2617 events from the OGLE-IV survey, where $\alpha_{\text{bd}} \sim 0.8$ and $\alpha_{\text{ms}} \sim 1.3$ were measured by comparing with a similar model based on Han & Gould (1995, 2003). Further, Wegg et al. (2017) measured $\alpha_{\text{bd}} = -0.7 \pm 0.9|_{\text{stat.}} \pm 0.8|_{\text{sys.}}$ and $\alpha_{\text{ms}} = 1.31 \pm 0.10|_{\text{stat.}} \pm 0.10|_{\text{sys.}}$ using a non-parametric dynamical Galactic model developed by Portail et al. (2017) for a comparison with the 3718 t_E measurements from the OGLE-III survey (Wyrzykowski et al. 2015). By contrast, the break mass, M_{br} , and the high mass slope, α_{hm} , are fixed in these previous studies, where $M_{\text{br}} = 0.5$ or $0.7 M_{\odot}$ and $\alpha_{\text{hm}} = 2.3$ or 2.0 are typically assumed, and no measurements on the two parameters using microlensing are reported in the literature.

Our method is a kind of a hybrid of the above two methods because we used $\tilde{\chi}_{\text{IMF}}^2 + \chi_{\text{pena}}^2$ to determine the IMF model, where $\tilde{\chi}_{\text{IMF}}^2$ is defined by $\chi_{t_E}^2 + 0.2(\chi_{N_{I<21}}^2 + \chi_{N_{I<18}}^2 + \chi_{f_{18/21}}^2)/3$, which is a combination of constraints from both the total 8000 t_E measurements and the star count data in two different brightness ranges in 1456 lines of sight (Mróz et al. 2017, 2019). This hybrid method enables us to concurrently measure the three IMF slopes of $(\alpha_{\text{hm}}, \alpha_{\text{ms}}, \alpha_{\text{bd}}) = (2.32^{+0.14}_{-0.10}, 1.16^{+0.08}_{-0.15}, 0.22^{+0.20}_{-0.55})$ over the entire mass range defined in Eq. (4), in addition to a break mass $M_{\text{br}} = 0.90^{+0.05}_{-0.14} M_{\odot}$.

To understand how each constraint contributes to the determination of the IMF parameters, we plot the $\chi_{t_E}^2$ and $\tilde{\chi}_{\text{IMF}}^2$ maps in Fig. 11. This is from the same grid search calculation described in Section 4.4. Fig. 11 (a) shows that the t_E distribution cannot solely determine upper limits on M_{br} and α_{hm} while it sets both upper and lower limits on α_{ms} and α_{bd} . An upper limit on the break mass M_{br} is set when the star count data is added to the restriction, which is shown in Fig. 11 (b),

Table 6. Mass-to-light ratio in K -band for indicated models.

Model	Υ_K	M_{br}	α_{hm}	α_{ms}	α_{bd}
	$[M_{\odot}/L_{K_{\odot}}]$	$[M_{\odot}]$			
This work	$0.72^{+0.05}_{-0.02}$	$0.90^{+0.05}_{-0.14}$	$2.32^{+0.14}_{-0.10}$	$1.16^{+0.08}_{-0.15}$	$0.22^{+0.20}_{-0.55}$
Kroupa (2001)	1.04	0.50	2.30	1.30	0.30
Zoccali et al. (2000) ^a	0.75	1.00	2.35	1.33	0.30

^aModified version of the third one in Table 3 of Zoccali et al. (2000), where we apply $\alpha_{\text{bd}} = 0.30$ because their measurement is insensitive to $M < 0.15 M_{\odot}$.

although that on α_{hm} is not yet set with $\tilde{\chi}_{\text{IMF}}^2$. Because there is a negative correlation between α_{hm} and M_{VVV} , an upper limit on α_{hm} is set for the first time by including χ_{pena}^2 , as shown in Fig. 10. This is because a larger α_{hm} value prefers a lighter bulge mass than the prior of $(1.32 \pm 0.08) \times 10^{10} M_{\odot}$ (Portail et al. 2017). As indicated in the $M_{\text{VVV}}/M_{\text{VVV,pri}}$ inset in the bottom right in Fig. 11 (b), the used data itself prefers $M_{\text{VVV}} \sim 0.75 M_{\text{VVV,pri}}$, a $\sim 4.1 \sigma$ smaller value than the prior, which results in a large χ^2 penalty value of $5 \times 4.1^2 \sim 84$.

The measured IMF slopes $(\alpha_{\text{hm}}, \alpha_{\text{ms}}, \alpha_{\text{bd}}) = (2.32^{+0.14}_{-0.10}, 1.16^{+0.08}_{-0.15}, 0.22^{+0.20}_{-0.55})$ seem similar to the local values $(\alpha_{\text{hm}}, \alpha_{\text{ms}}, \alpha_{\text{bd}}) = (2.3, 1.3, 0.3)$ by Kroupa (2001). However, the measured break mass $M_{\text{br}} = 0.90^{+0.05}_{-0.14} M_{\odot}$ is different from $0.5 M_{\odot}$ by Kroupa (2001). In fact, we find $\Delta\chi_{t_E}^2 = 496$, $\Delta\tilde{\chi}_{\text{IMF}}^2 = 810$, and $\Delta(\tilde{\chi}_{\text{IMF}}^2 + \chi_{\text{pena}}^2) = 852$ at the grid of $(M_{\text{br}}, \alpha_{\text{hm}}, \alpha_{\text{ms}}, \alpha_{\text{bd}}) = (0.5 M_{\odot}, 2.3, 1.3, 0.3)$, which indicates that the local IMF model by Kroupa (2001) is significantly disfavored by all three of the t_E data, star count data, and prior on M_{VVV} . Our IMF is similar to Zoccali et al. (2000), a single power-law of $M^{-1.33 \pm 0.07}$ in $0.15 M_{\odot} < M < 1.00 M_{\odot}$, rather than Kroupa (2001). This is expected because the Zoccali et al. (2000) measurement is for bulge stars. This similarity becomes clearer when we compare the two using the mass-to-light ratio values in the following section.

5.3. Mass-to-light Ratio and Dark Matter Fraction

Portail et al. (2015) constructed five versions of dynamical models, which are called the M80, M82.5, M85, M87.5 and M90 models, using the made-to-measure method (Syer & Tremaine 1996). These models have different degree of maximality ranging from 80 to 90%, where degree of maximality is defined as the proportion of the disk contribution to the total velocity curve, at the radius where the disk velocity curve is maximal. Each model reproduces the observed distributions toward the Galactic bulge, including the VVV photometric survey data (Saito et al. 2012), BRAVA RV data (Rich et al. 2007; Kunder et al. 2012), and OGLE-II proper motion data (Rattenbury et al. 2007a). Although the five models have consistent dynamical mass $(1.84 \pm 0.07) \times 10^{10} M_{\odot}$ inside the VVV bulge box ($\pm 2.2 \times \pm 1.4 \times \pm 1.2$ kpc), the dark matter fractions are different. This leads to different mass-to-light ratio values for the five models, which allows us to consider the dark matter fraction inferred by our model through it.

Table 6 lists the stellar mass-to-light ratio in K -band, Υ_K , calculated for the three IMF models from this work, Kroupa (2001), and Zoccali et al. (2000). The calculations are done with the initial-final mass relationships for the remnants described in Section 2.1 and the PARSEC isochrone models for age = 10 Gyr to compare with values by Portail et al. (2015). To check our calculation, we

calculate the Υ_K values for the [Kroupa \(2001\)](#) and [Zoccali et al. \(2000\)](#) IMFs. The calculation yields $\Upsilon_K = 1.04 M_\odot/L_{K_\odot}$ and $0.75 M_\odot/L_{K_\odot}$, respectively, which are consistent with the values calculated by [Portail et al. \(2015\)](#) for the two IMF models (see their Figure 15). The Υ_K value calculated for our IMF is $\Upsilon_K = 0.72^{+0.05}_{-0.02} M_\odot/L_{K_\odot}$, and this confirms the similarity with the [Zoccali et al. \(2000\)](#) IMF described in Section 5.2. The requirement for a mass-to-light ratio lower than the [Kroupa \(2001\)](#) IMF value comes mainly from a high ratio of the number of stars with $I < 18$ to the number of stars with $I < 21$ in the OGLE-IV data. The residuals in the bottom two panels of Fig. 5 show that our model, which has a 30% lower Υ_K value than the [Kroupa \(2001\)](#) model, still slightly underestimates the number of stars with $I < 18$ and slightly overestimates the number of stars with $I < 21$, on average.

Among the five dynamical models in [Portail et al. \(2015\)](#), the M80 model has the smallest Υ_K value, $0.83 \pm 0.08 M_\odot/L_{K_\odot}$, and the largest dark matter mass inside the VVV bulge box, $M_{\mathcal{DM}} = 0.33 \times 10^{10} M_\odot$ ³. Because our Υ_K value is even smaller than the M80 model's value, we linearly fit the relation between $M_{\mathcal{DM}}$ and Υ_K values among the five models in [Portail et al. \(2015\)](#) and extrapolate it to derive $M_{\mathcal{DM}} = 0.45^{+0.02}_{-0.06} \times 10^{10} M_\odot$ at $\Upsilon_K = 0.72^{+0.05}_{-0.02} M_\odot/L_{K_\odot}$ for our model. Note that the error of $M_{\mathcal{DM}}$ does not include the uncertainties of the relation, which is expected to be dominant, but it is sufficient to assess the reliability of the following independent estimate by a different approach.

Another approach to estimate $M_{\mathcal{DM}}$ is using M_{VVV} , the model integrated mass within the VVV bulge box. By simply subtracting the sum of $M_{\text{VVV}} = 1.14^{+0.10}_{-0.11} \times 10^{10} M_\odot$ and the central nuclear stellar disk mass of $0.2 \times 10^{10} M_\odot$ suggested by [Portail et al. \(2017\)](#) from the well-constrained dynamical mass $(1.85 \pm 0.05) \times 10^{10}$ ([Portail et al. 2017](#)), we have $M_{\mathcal{DM}} = 0.51^{+0.12}_{-0.11} \times 10^{10} M_\odot$, which can be larger than $M_{\mathcal{DM}} = (0.32 \pm 0.05) \times 10^{10} M_\odot$ by [Portail et al. \(2017\)](#). A drawback of this approach is an implicit assumption that no additional stellar mass other than the central nuclear stellar disk is missed inside the VVV bulge box in our density model that is fitted to data in $|b| \gtrsim 2^\circ$. However, because the $M_{\mathcal{DM}}$ estimation with this approach is consistent with $M_{\mathcal{DM}} = 0.45^{+0.02}_{-0.06} \times 10^{10} M_\odot$ estimated by the independent approach using Υ_K above, the implicit assumption seems reasonable. Thus, we consider $M_{\mathcal{DM}} = 0.51^{+0.12}_{-0.11} \times 10^{10} M_\odot$ as our fiducial value. This corresponds to a dark matter fraction in the VVV bulge box of $28 \pm 7\%$, which could be larger than a previous estimate of $17 \pm 2\%$ by [Portail et al. \(2017\)](#).

6. APPLICATION TO MICROLENSING ANALYSIS

In microlensing studies, a Galactic model is most commonly used as a prior probability distribution to calculate the posterior probability distributions of the lens mass and distance for individual events ([Alcock et al. 1995](#); [Beaulieu et al. 2006](#); [Koshimoto et al. 2014](#); [Bennett et al. 2014](#)). This is done when no or only one quantity that provides a mass–distance relation is measured, and such a Bayesian analysis usually yields a loosely constrained posterior distribution. Because of their large uncertainties, results of the Bayesian estimates for individual events are not very sensitive to the choice of Galactic models ([Yang et al. 2020](#)), and thus we do not apply our Galactic model to such an analysis in this paper.

Using a refined Galactic model is important when it is applied to a statistical study with many events because small differences for individual events are combined and become significant. In Section

³ The nuclear stellar disk mass based on [Portail et al. \(2017\)](#), $0.20 \times 10^{10} M_\odot$, is subtracted from the fiducial dark matter mass of the M80 model, $0.53 \times 10^{10} M_\odot$, because the nuclear stellar disk mass was not considered in the dark matter mass estimation of [Portail et al. \(2015\)](#).

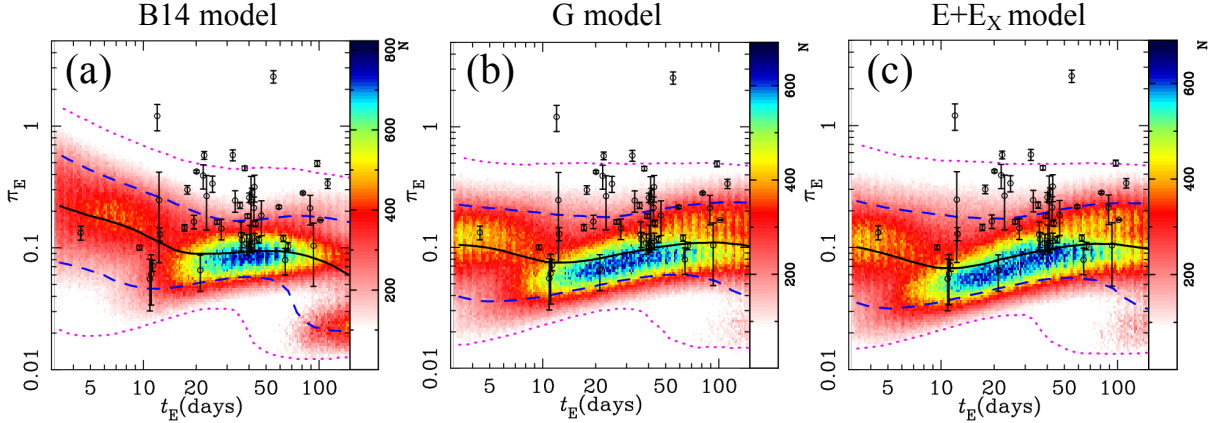


Figure 12. Reproductions of Figure 1 of Koshimoto & Bennett (2020) using the Galactic models developed here, where the probability of microlens parallax, π_E , as a function of fixed t_E , $\Gamma_{\text{Gal}}(\pi_E|t_E)$, is plotted using (a) the B14 model from Koshimoto & Bennett (2020), (b) the G model, and (c) the E+E_X model. Some updates, such as inclusion of neutron stars and black holes, are applied compared to the original one in Koshimoto & Bennett (2020). The black dots are measured values for 50 events in the raw sample of Zhu et al. (2017). The solid black, dashed blue, and dotted magenta lines indicate the median, 1σ , and 2σ for $\Gamma_{\text{Gal}}(\pi_E|t_E)$, respectively.

6.1 below, we repeat part of the analysis by Koshimoto & Bennett (2020) using the new Galactic models and compare the result with the one using the Bennett et al. (2014) model, which is a Galactic model frequently used for microlensing studies.

Another useful way to use a Galactic model is to distinguish between degenerate solutions, which indicate different lens system physical quantities for the analysis of an individual event. We apply our Galactic model to calculate the prior probability distribution for OGLE-2011-BLG-0950 (Choi et al. 2012; Suzuki et al. 2016) in Section 6.2, in which degenerate models indicate different lens-source relative proper motion μ_{rel} values with each other and very different mass-ratios. This is the only ambiguous event suffering from a degeneracy between planetary and binary solutions out of the 29 events in the Suzuki et al. (2016) combined sample, and we show that the stellar binary solution is preferred by our Galactic model.

6.1. Statistical Study Using a Galactic Model

Koshimoto & Bennett (2020) compared 50 microlens parallax, π_E , measurements from the 2015 *Spitzer* campaign (Zhu et al. 2017) to three different Galactic models (Sumi et al. 2011; Bennett et al. 2014; Zhu et al. 2017), commonly used in microlensing analyses. They found that ≥ 37 events have π_E values higher than the medians predicted by the Galactic models, and concluded that the difference is mainly attributed to systematic errors in the *Spitzer* microlens parallax measurements. They considered that part of the inconsistency might originate from some simplistic features in the Galactic models, such as constant velocity dispersion regardless of Galactic distance, which is one of the main motivations for this work. Because our Galactic model includes the dependency of the velocity dispersion on the Galactic location, as well as further updates to match recent observations, we test their claim using the updated models.

Following Koshimoto & Bennett (2020), we calculate $\Gamma_{\text{Gal}}(\pi_E|t_E)$, the probability distribution of π_E as a function of a given t_E value, which can be directly compared with observed π_E values without

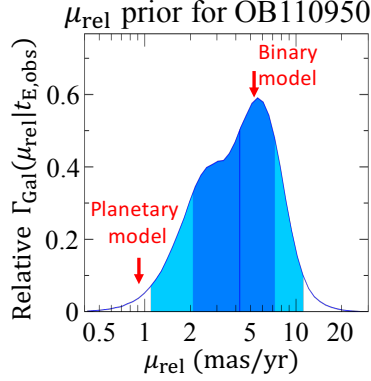


Figure 13. Prior probability distribution of the lens-source relative proper motion μ_{rel} for OGLE-2011-BLG-0950, calculated using the best-fit G+G_X model. The indicated two μ_{rel} values are calculated using the parameters in Table 3 of Suzuki et al. (2016).

a detection efficiency correction. Color maps in Fig. 12 show the distributions toward a typical sky direction of the 50 *Spitzer* events of $(l, b) = (1.0^\circ, -2.2^\circ)$, where a total of 10^5 artificial events contribute to each bin of t_E with width 0.05 dex in $\log t_E$. Fig. 12 (a) shows the result with the B14 model from Koshimoto & Bennett (2020) for comparison, while the (b) and (c) panels show the results with the best-fit G and E+E_X models, respectively. We selected the G and E+E_X models here to show the largest variation caused by one’s choice from the E, G, E+E_X, and G+G_X models, because these two models have the largest χ^2_{fit} difference from each other ($\Delta\chi^2_{\text{fit}} \sim 15000$) among the four models. In the calculation, we also included the neutron star and black hole populations, which were ignored in Koshimoto & Bennett (2020) as negligible possibilities. The distinct population in the bottom right for each color map primarily consists of black hole lenses, which confirms the same feature predicted by the Lam et al. (2020) simulation. In contrast to our previous expectation, this population changes the distribution in $t_E \gtrsim 60$ days, seen as undulations of the median, 1 σ , and 2 σ lines in the figure.

There is a clear difference in the distributions between the B14 model and our two new models; compared with the G and E+E_X models, the B14 model tends to have higher π_E values with short t_E values, while it tends to have lower π_E values with long t_E values. By contrast, there is no major difference between the G and E+E_X models. We calculated the same distributions with the E and G+G_X models, and found that they were almost identical to the E+E_X model’s distribution.

Black dots in each panel are the reported π_E values in the raw-sample of Zhu et al. (2017), in which the Galactic prior is not applied unlike Figure 1 of Koshimoto & Bennett (2020). This results in 43, 43, and 44 events whose π_E values above the median of $\Gamma_{\text{Gal}}(\pi_E|t_E)$ with the B14, G, and E+E_X models, respectively. Even though there is a clear visual difference in the distributions between the old and new models, statistical quantities inferred from this analysis happen to be very similar to the old models, which implies no change to the Koshimoto & Bennett (2020) conclusions. Nevertheless, Fig. 12 shows that it could be very different depending on the observed distributions, indicating that the choice of the models is important for a statistical analysis using a Galactic model.

6.2. Prior Calculation to Distinguish Degenerate Models

Suzuki et al. (2016) has analyzed the largest statistical sample of 29 planetary events till now and found a peak in the mass-ratio function for the first time. Out of the 29 planetary events, there is one

ambiguous event, OGLE-2011-BLG-0950, which has degenerate planetary and stellar binary mass-ratio models with $\Delta\chi^2 \sim 20$ (Choi et al. 2012; Suzuki et al. 2016). The preferred planetary model has mass-ratio $q \sim 6 \times 10^{-4}$ while the binary model has $q \sim 0.5$ (Suzuki et al. 2016). Although our Galactic model cannot assess the relative prior probability for these two mass-ratio values because we do not know the relative frequency of systems with mass ratios with $q \sim 6 \times 10^{-4}$ compared to systems with $q \sim 0.5$, these two models have very different lens-source proper motion μ_{rel} values, which can be assessed using our model.

Fig. 13 shows the calculated μ_{rel} prior, $\Gamma_{\text{Gal}}(\mu_{\text{rel}}|t_{\text{E,obs}})$, using the best-fit G+G_X model, where $t_{\text{E,obs}}$ is the observed t_{E} value for this event and we applied $t_{\text{E,obs}} = 68 \pm 3$ days (Suzuki et al. 2016). This figure shows that our Galactic model significantly prefers the μ_{rel} value for the stellar binary model over that for the planetary model. The preference of the stellar binary model is also suggested by a high angular resolution follow-up imaging by Keck (Terry et al., in preparation).

7. SUMMARY AND CONCLUSION

In this study, we developed parametric Galactic models using constraints from the spatial distributions of the median velocity and velocity dispersion from the Gaia DR2 (Gaia Collaboration et al. 2018), OGLE-III RC star count data (Nataf et al. 2013), VIRAC proper motion data (Smith et al. 2018; Clarke et al. 2019), BRAVA radial velocity data (Rich et al. 2007), and OGLE-IV star count and microlensing event data (Mróz et al. 2017, 2019). Our modeling indicated the following (we note that the error estimates could be influenced by our non-standard fitting method of an iterative step-by-step procedure.):

1. Local velocity dispersions for the thin and thick disks of $(\sigma_{R,\odot}^{\text{thin}}, \sigma_{z,\odot}^{\text{thin}}, \sigma_{R,\odot}^{\text{thick}}, \sigma_{z,\odot}^{\text{thick}}) = (35.2\text{--}44.0, 22.2\text{--}25.4, 68\text{--}75, 47.8\text{--}61.4)$ km/s, slopes of age-velocity dispersion relation for the thin disk of $(\beta_R, \beta_z) = (0.22\text{--}0.34, 0.77\text{--}0.82)$, and scale lengths for the velocity dispersion distributions of $(R_{\sigma_R}^{\text{thin}}, R_{\sigma_z}^{\text{thin}}, R_{\sigma_R}^{\text{thick}}, R_{\sigma_z}^{\text{thick}}) = (9.5\text{--}21.4, 5.9\text{--}10.4, 47\text{--}180, 6.9\text{--}52.0)$ kpc by a grid search with the modified Shu DF model (Sharma et al. 2014) over the Gaia data in $3340 \text{ pc} < R < 8440 \text{ pc}$. The value ranges correspond to variations due to our choice for the scale height model (linear or flat) and for the fitting range ($|z| < 3400 \text{ pc}$ or $|z| < 900 \text{ pc}$).
2. Although a linear scale height disk model is preferred with the Gaia data, a flat scale height model is preferred with $\Delta\chi_{\text{fit}}^2 > 1000$ with the other datasets for bulge stars when combined with the bulge model, which might indicate a best choice somewhere in the middle.
3. A bar pattern speed of $\Omega_p = 45.9_{-5.4}^{+4.0}$ km/s/kpc, which could be slightly larger than but consistent with recent measurements of 39.0 ± 3.5 km/s/kpc (Portail et al. 2017) and 41 ± 3 km/s/kpc (Sanders et al. 2019b).
4. Stellar mass inside the VVV bulge box, defined as the central region inside $(x', y', z') = (\pm 2.2, \pm 1.4, \pm 1.2)$ kpc (Wegg & Gerhard 2013), of $M_{\text{VVV}} = 1.14_{-0.11}^{+0.10} \times 10^{10} M_\odot$. This results in the dark matter mass inside the box of $M_{\mathcal{DM}} = 0.51_{-0.11}^{+0.12} \times 10^{10} M_\odot$ when we assume the dynamical mass of $(1.85 \pm 0.05) \times 10^{10}$ and the central nuclear stellar disk of $0.2 \times 10^{10} M_\odot$ suggested by Portail et al. (2017), which could be larger than a previous estimate of $M_{\mathcal{DM}} = (0.32 \pm 0.05) \times 10^{10} M_\odot$ (Portail et al. 2017).

5. An IMF with a break mass at $M_{\text{br}} = 0.90_{-0.14}^{+0.05} M_{\odot}$ and slopes for different mass ranges of $(\alpha_{\text{hm}}, \alpha_{\text{ms}}, \alpha_{\text{bd}}) = (2.32_{-0.10}^{+0.14}, 1.16_{-0.15}^{+0.08}, 0.22_{-0.55}^{+0.20})$, which is different from the Kroupa (2001) local IMF but similar to the bulge IMF measured by Zoccali et al. (2000).
6. The IMF indicates stellar mass-to-light ratio in K -band, $\Upsilon_K = 0.72_{-0.02}^{+0.05} M_{\odot}/L_{K_{\odot}}$. A comparison with the Υ_K values of a series of five dynamical models by Portail et al. (2015) yields $M_{\mathcal{DM}} = 0.45_{-0.06}^{+0.02} \times 10^{10} M_{\odot}$, which is consistent with the above value implied by M_{VVV} .

We used our new Galactic models to test the result of Koshimoto & Bennett (2020) in which the existence of systematic errors in *Spitzer* microlens parallax measurements is claimed based on older, simpler Galactic models. We saw a significant difference in the predicted microlens parallax distributions between our model and a model used in the Koshimoto & Bennett (2020) analysis, but this had no effect on the conclusions of Koshimoto & Bennett (2020) that the *Spitzer* microlensing parallax measurements were contaminated by systematic errors.

We also applied the new model to calculate a prior probability distribution of the lens-source relative proper motion μ_{rel} for OGLE-2011-BLG-0950, the only ambiguous event in the Suzuki et al. (2016) planet sample. Our calculation shows that the μ_{rel} value for the stellar binary solution is significantly preferred over that for the planetary solution.

Although the influence of model choice for individual event analysis is expected to be small, it becomes significant for statistical studies using multiple events (Yang et al. 2020). With many recent microlensing event discoveries, a refined Galactic model like the one in this work is beneficial to study populations of various objects ranging from planets to black holes. Our model is purely parametric, which makes it easy to implement and reproduce. The demand is expected to increase in the era of the *Nancy Grace Roman Space Telescope*, previously known as *WFIRST*, which is expected to find 54,000 microlensing events during the primary 5 years survey toward the Galactic center (Gaudi et al. 2019). Because our current models lack constraints from data in $|b| < 2^{\circ}$, where the *Roman* fields are likely to be located, a further update should be expected in the future. In such future updates, survey data toward the Galactic center expected to be collected by coming missions like Japan Astrometry Satellite Mission for INfrared Exploration (JASMINE; Gouda 2012)⁴ or PRime-focus INfrared Microlensing Experiment (PRIME⁵) will be very useful.

We are grateful to Przemek Mróz, Nathan Golovich, and David Katz who provided us with valuable data from their leading studies, which significantly helped us do this work. We would like to thank Shogo Nishiyama for his helpful suggestion for our model. NK was supported by JSPS KAKENHI Grant Number JP18J00897 and the JSPS overseas research fellowship. JB acknowledges the support by JSPS KAKENHI Grant Numbers 18K03711, 18H01248, 19H01933, 21H00054 and 21K03633.

⁴ <http://jasmine.nao.ac.jp/index-en.html>

⁵ <http://www-ir.ess.sci.osaka-u.ac.jp/prime/index.html>

Table 7. $\tilde{\chi}_{\text{sum}}^2$, $\chi_{N_{\text{eve}}}^2$, and $\chi_{t_E}^2$ values for each model with and without G20 option.

Model	w/o G20			w/ G20		
	$\tilde{\chi}_{\text{sum}}^2$ ^a	$\chi_{N_{\text{eve}}}^2$	$\chi_{t_E}^2$	$\tilde{\chi}_{\text{sum}}^2$	$\chi_{N_{\text{eve}}}^2$	$\chi_{t_E}^2$
E	80173	21887	78	81411	22018	115
G	91319	22022	89	92261	22283	133
E+E _X	76261	21857	67	77583	22058	113
G+G _X	76500	21852	68	77797	22041	109

$$^a \tilde{\chi}_{\text{sum}}^2 \equiv \tilde{\chi}_{\rho_B}^2 + 2\chi_{v_B}^2 + 5\chi_{\text{pena}}^2.$$

NOTE—G20 option is disfavored in any model with any χ^2 value.

DPB and NK were supported by NASA through grant NASA-80NSSC18K0274 and award number 80GSFC17M0002.

APPENDIX

A. COMPARING TO ANOTHER SET OF THE EINSTEIN RADIUS CROSSING TIME DATA

Measurements of t_E for a microlensing event can be occasionally erroneous due to systematic errors in light curve data. [Golovich et al. \(2020\)](#) recently reanalyzed all the 5788 events of [Mróz et al. \(2019\)](#) using their newly developed model to simultaneously handle microlens parallax due to Earth’s motion, systematic instrumental effects, and unlensed stellar variability with a Gaussian Process model. Consequently, they found fewer long t_E events and more short t_E events compared to the [Mróz et al. \(2019\)](#) t_E distribution. To consider this possible systematic effect in the t_E distribution, we attempt another option, hereafter called the G20 option, using the t_E distribution from [Golovich et al. \(2020\)](#) instead of the original [Mróz et al.’s](#) distribution.

[Golovich et al. \(2020\)](#) conducted their modeling on the 5788 events in the low-cadence fields ([Mróz et al. 2019](#)), but not on the 2212 events in the high-cadence fields ([Mróz et al. 2017](#)). To approximately apply the systematic effect correction by [Golovich et al. \(2020\)](#) to the 2212 events, we derived the following factor

$$g(t_E) = \frac{N_{\text{G20}}^{\text{obs}}(t_E)}{N_{\text{O}_{\text{low}}}^{\text{obs}}(t_E)} \quad (\text{A1})$$

by comparing the two t_E distributions of the 5788 events in the low-cadence fields by [Mróz et al. \(2019\)](#) and [Golovich et al. \(2020\)](#) ([Golovich, private communication](#)). We multiply $g(t_E)$ by the t_E distribution of the 2212 events in the high-cadence fields, where the resultant number is rounded to the nearest whole number and use as $N_{\text{O}_{\text{hi}}}^{\text{obs}}(t_E)$ in the G20 option. The t_E data with and without the G20 option are plotted in [Fig. 8](#).

With the G20 option, we should also consider modifying the number of detected events as a function of t_E for each i th subfield, $N_{\text{eve},i}^{\text{obs}}(t_{E,j})$. Whereas the numbers by [Golovich et al. \(2020\)](#) are used for $i \in \text{O}_{\text{low}}$, we apply $g(t_E)$ for $i \in \text{O}_{\text{hi}}$. Multiplying $g(t_E)$ by $N_{\text{eve},i}^{\text{obs}}(t_{E,j})$ is not feasible because $N_{\text{eve},i}^{\text{obs}}(t_{E,j})$

is mostly 0, and its typical non-zero value is 1 or 2, which is largely affected by the round-off process needed to calculate the Poisson probability in Eq. (39). Therefore, the compared model value of $N_{\text{eve},i}^{\text{mod}}(t_{\text{E},j})$ is instead divided by $g(t_{\text{E},j})$, and thereafter, $\chi_{N_{\text{eve}}}^2$ is calculated. Applying $g(t_{\text{E}})$ to the events in the high-cadence fields is a crude attempt for the Golovich et al. (2020) correction because the factor should depend on both the t_{E} value, as well as characteristics of individual events or fields, such as extinction, event brightness, impact factor, and light curve coverage. For analyzing the impact qualitatively, this is sufficient, though.

We compare the best-fit $\tilde{\chi}_{\text{sum}}^2$, $\chi_{N_{\text{eve}}}^2$, and $\chi_{t_{\text{E}}}^2$ values for each model, with and without the G20 option in Table 7. We find that all the three χ^2 values increase when the Golovich et al. (2020) correction based on a Gaussian Process model is applied to the t_{E} data regardless of the model choice. As discussed above, the G20 application to the t_{E} distribution in the high-cadence fields is a crude approximation. However, as shown in Fig. 8, the breakdown of $\Delta\chi_{t_{\text{E}}}^2$ is 7 from $\chi_{t_{\text{E},\text{Ohi}}}^2$ and 34 from $\chi_{t_{\text{E},\text{Olow}}}^2$; therefore, the worse $\chi_{t_{\text{E}}}^2$ with the G20 option is attributed to the t_{E} distribution in the low-cadence fields, to which the G20 correction is accurately applied, rather than the t_{E} distribution in the high-cadence fields. Although Fig. 8 is for the G+G_X model, this is same for the other models. Thus, we conclude that with our model framework, the original Mróz et al.’s t_{E} distributions are favored to the Golovich et al.’s one and use models without the G20 option as the fiducial best-fit models in this study.

REFERENCES

- Akeson, R. L., Chen, X., Ciardi, D., et al. 2013, *PASP*, 125, 989. doi:10.1086/672273
- Alcock, C., Allsman, R. A., Alves, D., et al. 1995, *ApJL*, 454, L125
- An, J. H., Albrow, M. D., Beaulieu, J.-P., et al. 2002, *ApJ*, 572, 521
- Batista, V., Beaulieu, J.-P., Bennett, D. P., et al. 2015, *ApJ*, 808, 170
- Beaulieu, J.-P., Bennett, D. P., Fouqué, P., et al. 2006, *Nature*, 439, 437
- Bennett, D. P., Batista, V., Bond, I. A., et al. 2014, *ApJ*, 785, 155 (B14)
- Bennett, D. P., Becker, A. C., Quinn, J. L., et al. 2002, *ApJ*, 579, 639. doi:10.1086/342225
- Bennett, D. P., Bhattacharya, A., Anderson, J., et al. 2015, *ApJ*, 808, 169
- Bhattacharya, A., Beaulieu, J.-P., Bennett, D. P., et al. 2018, *AJ*, 156, 289
- Binney, J. 2012, *MNRAS*, 426, 1328. doi:10.1111/j.1365-2966.2012.21692.x
- Binney, J. & Piffl, T. 2015, *MNRAS*, 454, 3653. doi:10.1093/mnras/stv2225
- Binney, J. & Tremaine, S. 2008, *Galactic Dynamics: Second Edition*, by James Binney and Scott Tremaine. ISBN 978-0-691-13026-2 (HB). Published by Princeton University Press, Princeton, NJ USA, 2008.
- Bland-Hawthorn, J. & Gerhard, O. 2016, *ARA&A*, 54, 529. doi:10.1146/annurev-astro-081915-023441
- Bovy, J. 2017, *MNRAS*, 470, 1360
- Bressan, A., Marigo, P., Girardi, L., et al. 2012, *MNRAS*, 427, 127
- Calamida, A., Sahu, K. C., Anderson, J., et al. 2014, *ApJ*, 790, 164. doi:10.1088/0004-637X/790/2/164
- Calamida, A., Sahu, K. C., Casertano, S., et al. 2015, *ApJ*, 810, 8. doi:10.1088/0004-637X/810/1/8
- Cao, L., Mao, S., Nataf, D., et al. 2013, *MNRAS*, 434, 595. doi:10.1093/mnras/stt1045
- Chen, Y., Girardi, L., Bressan, A., et al. 2014, *MNRAS*, 444, 2525
- Choi, J.-Y., Shin, I.-G., Han, C., et al. 2012, *ApJ*, 756, 48. doi:10.1088/0004-637X/756/1/48
- Chung, S.-J., Han, C., Park, B.-G., et al. 2005, *ApJ*, 630, 535. doi:10.1086/432048

- Clarke, J. P., Wegg, C., Gerhard, O., et al. 2019, *MNRAS*, 489, 3519. doi:10.1093/mnras/stz2382
- Duchêne, G. & Kraus, A. 2013, *ARA&A*, 51, 269. doi:10.1146/annurev-astro-081710-102602
- Dwek, E., Arendt, R. G., Hauser, M. G., et al. 1995, *ApJ*, 445, 716
- Einasto, J. 1979, *The Large-Scale Characteristics of the Galaxy*, 84, 451
- Gaia Collaboration, Katz, D., Antoja, T., et al. 2018, *A&A*, 616, A11
- Gardner, E., Debattista, V. P., Robin, A. C., et al. 2014, *MNRAS*, 438, 3275. doi:10.1093/mnras/stt2430
- Gaudi, B. S., Akeson, R., Anderson, J., et al. 2019, *BAAS*, 51, 211
- Golovich, N., Dawson, W. A., Bartolić, F., et al. 2020, arXiv:2009.07927
- Gouda, N. 2012, *Galactic Archaeology: Near-Field Cosmology and the Formation of the Milky Way*, 458, 417
- Gravity Collaboration, Abuter, R., Amorim, A., et al. 2019, *A&A*, 625, L10. doi:10.1051/0004-6361/201935656
- Han, C., & Gould, A. 1995, *ApJ*, 447, 53
- Han, C. & Gould, A. 2003, *ApJ*, 592, 172. doi:10.1086/375706
- Hawkins, K., Leistedt, B., Bovy, J., et al. 2017, *MNRAS*, 471, 722. doi:10.1093/mnras/stx1655
- Howard, C. D., Rich, R. M., Reitzel, D. B., et al. 2008, *ApJ*, 688, 1060. doi:10.1086/592106
- Jung, Y. K., Udalski, A., Gould, A., et al. 2018, *AJ*, 155, 219
- Kalirai, J. S., Hansen, B. M. S., Kelson, D. D., et al. 2008, *ApJ*, 676, 594. doi:10.1086/527028
- Koshimoto, N. & Bennett, D. P. 2020, *AJ*, 160, 177. doi:10.3847/1538-3881/abaf4e
- Koshimoto, N., Bennett, D. P., & Suzuki, D. 2020, *AJ*, 159, 268. doi:10.3847/1538-3881/ab8adf
- Koshimoto, N. & Ranc, C. 2021, Zenodo.4784949. doi: 10.5281/zenodo.4784949
- Koshimoto, N., Udalski, A., Sumi, T., et al. 2014, *ApJ*, 788, 128
- Kozłowski, S., Woźniak, P. R., Mao, S., et al. 2006, *MNRAS*, 370, 435. doi:10.1111/j.1365-2966.2006.10487.x
- Kroupa, P. 2001, *MNRAS*, 322, 231
- Kuijken, K. & Rich, R. M. 2002, *AJ*, 124, 2054. doi:10.1086/342540
- Kunder, A., Koch, A., Rich, R. M., et al. 2012, *AJ*, 143, 57. doi:10.1088/0004-6256/143/3/57
- Lam, C. Y., Lu, J. R., Hosek, M. W., et al. 2020, *ApJ*, 889, 31. doi:10.3847/1538-4357/ab5fd3
- Launhardt, R., Zylka, R., & Mezger, P. G. 2002, *A&A*, 384, 112. doi:10.1051/0004-6361:20020017
- Mao, S., & Paczynski, B. 1991, *ApJL*, 374, L37
- McKee, C. F., Parravano, A., & Hollenbach, D. J. 2015, *ApJ*, 814, 13
- McWilliam, A. & Zoccali, M. 2010, *ApJ*, 724, 1491. doi:10.1088/0004-637X/724/2/1491
- Metropolis, N., Rosenbluth, A. W., Rosenbluth, M. N., Teller, A. H., & Teller, E. 1953, *JChPh*, 21, 1087
- Minniti, D., Lucas, P. W., Emerson, J. P., et al. 2010, *NewA*, 15, 433
- Mróz, P., Udalski, A., Skowron, J., et al. 2017, *Nature*, 548, 183
- Mróz, P., Udalski, A., Skowron, J., et al. 2019, *ApJS*, 244, 29. doi:10.3847/1538-4365/ab426b
- Nataf, D. M., Gould, A., Fouqué, P., et al. 2013, *ApJ*, 769, 88. doi:10.1088/0004-637X/769/2/88
- Nataf, D. M., Udalski, A., Gould, A., et al. 2010, *ApJL*, 721, L28. doi:10.1088/2041-8205/721/1/L28
- Nishiyama, S., Yasui, K., Nagata, T., et al. 2013, *ApJL*, 769, L28. doi:10.1088/2041-8205/769/2/L28
- Nordström, B., Mayor, M., Andersen, J., et al. 2004, *A&A*, 418, 989. doi:10.1051/0004-6361:20035959
- Penny, M. T., Gaudi, B. S., Kerins, E., et al. 2019, *ApJS*, 241, 3. doi:10.3847/1538-4365/aafb69
- Penny, M. T., Henderson, C. B., & Clanton, C. 2016, *ApJ*, 830, 150
- Piffl, T., Binney, J., McMillan, P. J., et al. 2014, *MNRAS*, 445, 3133. doi:10.1093/mnras/stu1948
- Poindexter, S., Afonso, C., Bennett, D. P., et al. 2005, *ApJ*, 633, 914. doi:10.1086/468182
- Portail, M., Wegg, C., Gerhard, O., et al. 2015, *MNRAS*, 448, 713. doi:10.1093/mnras/stv058
- Portail, M., Gerhard, O., Wegg, C., & Ness, M. 2017, *MNRAS*, 465, 1621
- Raithel, C. A., Sukhbold, T., & Özel, F. 2018, *ApJ*, 856, 35. doi:10.3847/1538-4357/aab09b
- Rattenbury, N. J., Mao, S., Debattista, V. P., et al. 2007a, *MNRAS*, 378, 1165. doi:10.1111/j.1365-2966.2007.11851.x
- Rattenbury, N. J., Mao, S., Sumi, T., et al. 2007b, *MNRAS*, 378, 1064. doi:10.1111/j.1365-2966.2007.11843.x

- Rich, R. M., Reitzel, D. B., Howard, C. D., et al. 2007, *ApJL*, 658, L29. doi:10.1086/513509
- Robin, A. C., Bienaymé, O., Fernández-Trincado, J. G., et al. 2017, *A&A*, 605, A1. doi:10.1051/0004-6361/201630217
- Robin, A. C., Marshall, D. J., Schultheis, M., et al. 2012, *A&A*, 538, A106. doi:10.1051/0004-6361/201116512
- Robin, A. C., Reylé, C., Derrière, S., & Picaud, S. 2003, *A&A*, 409, 523
- Robin, A. C., Reylé, C., Fliri, J., et al. 2014, *A&A*, 569, A13. doi:10.1051/0004-6361/201423415
- Saito, R. K., Hempel, M., Minniti, D., et al. 2012, *A&A*, 537, A107. doi:10.1051/0004-6361/201118407
- Sanders, J. L. & Binney, J. 2015, *MNRAS*, 449, 3479. doi:10.1093/mnras/stv578
- Sanders, J. L., Smith, L., Evans, N. W., et al. 2019a, *MNRAS*, 487, 5188. doi:10.1093/mnras/stz1630
- Sanders, J. L., Smith, L., & Evans, N. W. 2019b, *MNRAS*, 488, 4552. doi:10.1093/mnras/stz1827
- Schönrich, R. & Binney, J. 2012, *MNRAS*, 419, 1546. doi:10.1111/j.1365-2966.2011.19816.x
- Sharma, S. & Bland-Hawthorn, J. 2013, *ApJ*, 773, 183. doi:10.1088/0004-637X/773/2/183
- Sharma, S., Bland-Hawthorn, J., Binney, J., et al. 2014, *ApJ*, 793, 51
- Shu, F. H. 1969, *ApJ*, 158, 505. doi:10.1086/150214
- Smith, L. C., Lucas, P. W., Kurtev, R., et al. 2018, *MNRAS*, 474, 1826. doi:10.1093/mnras/stx2789
- Specht, D., Kerins, E., Awiphan, S., et al. 2020, *MNRAS*, 498, 2196. doi:10.1093/mnras/staa2375
- Sumi, T., Kamiya, K., Bennett, D. P., et al. 2011 *ApJ*, 473, 349 (S11)
- Suzuki, D., Bennett, D. P., Ida, S., et al. 2018, *ApJL*, 869, L34. doi:10.3847/2041-8213/aaf577
- Suzuki, D., Bennett, D. P., Sumi, T., et al. 2016, *ApJ*, 833, 145
- Syer, D. & Tremaine, S. 1996, *MNRAS*, 282, 223. doi:10.1093/mnras/282.1.223
- Tang, J., Bressan, A., Rosenfield, P., et al. 2014, *MNRAS*, 445, 4287
- Terry, S. K., Barry, R. K., Bennett, D. P., et al. 2020, *ApJ*, 889, 126. doi:10.3847/1538-4357/ab629b
- Wegg, C. & Gerhard, O. 2013, *MNRAS*, 435, 1874. doi:10.1093/mnras/stt1376
- Wegg, C., Gerhard, O., & Portail, M. 2015, *MNRAS*, 450, 4050. doi:10.1093/mnras/stv745
- Wegg, C., Gerhard, O., & Portail, M. 2016, *MNRAS*, 463, 557. doi:10.1093/mnras/stw1954
- Wegg, C., Gerhard, O., & Portail, M. 2017, *ApJL*, 843, L5
- Wyrzykowski, L., Rynkiewicz, A. E., Skowron, J., et al. 2015, *ApJS*, 216, 12
- Wyrzykowski, L., Kostrzewa-Rutkowska, Z., Skowron, J., et al. 2016, *MNRAS*, 458, 3012. doi:10.1093/mnras/stw426
- Wyrzykowski, L. & Mandel, I. 2020, *A&A*, 636, A20. doi:10.1051/0004-6361/201935842
- Yang, H., Mao, S., Zang, W., et al. 2020, arXiv:2010.16146
- Yoo, J., DePoy, D. L., Gal-Yam, A., et al. 2004, *ApJ*, 603, 139
- Yu, J. & Liu, C. 2018, *MNRAS*, 475, 1093. doi:10.1093/mnras/stx3204
- Zhu, W., Udalski, A., Calchi Novati, S., et al. 2017, *AJ*, 154, 210
- Zoccali, M., Cassisi, S., Frogel, J. A., et al. 2000, *ApJ*, 530, 418. doi:10.1086/308359